In-vivo Human Superior Colliculus Functional Connectivity and Anatomy Segmentation

Dissertation

zur Erlangung des Grades eines

Doktors der Naturwissenschaften

der Mathematisch-Naturwissenschaftlichen Fakultät
und
der Medizinischen Fakultät
der Eberhard-Karls-Universität Tübingen

vorgelegt

von

Amin Dadashi

Zahedan, Iran

2020

Tag der mündlichen Prüfung: July 7, 2021

Dekan der Math.- Nat. Fakultät: Prof. Dr. Thilo Stehle

Dekan der Medizinischen Fakultät: Prof. Dr. Bernd Pichler

1. Berichterstatter: PD Dr. Marc Himmelbach

2. Berichterstatter: Prof. Dr. Markus Siegel

Prüfungskommission: PD Dr. Marc Himmelbach

                                       Prof. Dr. Markus Siegel

                                       Prof. Dr. Ludger Johannes Schöls

                                       Prof. Dr. Uwe Klose

.

Erklärung / Declaration:

Ich erkläre, dass ich die zur Promotion eingereichte Arbeit mit dem Titel:

"In-vivo Human Superior Colliculus Functional Connectivity and Anatomy Segmentation"

selbständig verfasst, nur die angegebenen Quellen und Hilfsmittel benutzt und wörtlich oder inhaltlich übernommene Stellen als solche gekennzeichnet habe. Ich versichere an Eides statt, dass diese Angaben wahr sind und dass ich nichts verschwiegen habe. Mir ist bekannt, dass die falsche Abgabe einer Versicherung an Eides statt mit Freiheitsstrafe bis zu drei Jahren oder mit Geldstrafe bestraft wird.

hereby declare that I have produced the work entitled "In-vivo Human Superior Colliculus Functional Connectivity and Anatomy Segmentation", submitted for the award of a doctorate, on my own (without external help), have used only the sources and aids indicated and have marked passages included from other works, whether verbatim or in content, as such. I swear upon oath that these statements are true and that I have not concealed anything. I am aware that making a false declaration under oath is punishable by a term of imprisonment of up to three years or by a fine.

Tübingen, den ....

          Datum / Date   Unterschrift /Signature

ABSTRACT

The superior colliculus (SC) is a paired and layered structure located on the dorsal surface of the midbrain playing an important role in auditory, visual, motor control, and multisensory integration. The small size of the nuclei, the composition of the midbrain, and the proximity of the SC to the brain vascular and ventricular formations are major hindrances in the way of studying human SC in-vivo. However, recent advances in magnetic resonance imaging (MRI) in terms of resolution, acquisition time, and signal-to-noise ratio (SNR) which are the products of the improved sequences and stronger magnets e.g. Ultra-High-Field (UHF) MRI has enabled the possibility of studying brain areas such as SC as a region of interest (ROI).

In the first phase of this project, we estimated the global functional connectivity network (FCN) of the SC. To this end, we used 3T functional MRI (fMRI) data acquired by the Human Connectome Project (HCP) consortium. The data was preprocessed by the HCP pipeline and was corrected for motion artifacts and was registered to a standard space template. Driven by the limitation imposed by the SNR and the resolution, we studied all the SC layers of each hemisphere combined. Our results were following major animal studies while introducing unnoticed connections to frontal attentional and motor control areas. Importantly and in general, we mapped the entire functional network of the alive human brain SC, in-vivo; provide the chance for a direct comparison with previously detected structural connections of the SC in mammalians' brains.

In the second phase of the project, we examined a layer-wise connectivity pattern of the human SC function in-vivo, using the 7T fMRI dataset from the HCP database. Our goal in the second phase was to identify the functional sub-networks that the SC is involved in by breaking the previously estimated network into smaller regions groups based on depth-dependent SC FCN. By spatial upsampling of the SC region and the use of k-means clustering, we discovered six sub-networks with unique characteristics. These networks comprised areas associated with vision, the oculomotor system with an emphasis on the peripheral vision, and planning goal-directed actions. Also, we identified clusters that are representing the areas of no functional connection to SC.

In the third phase of this project, we developed a solution for human midbrain

segmentation with a particular focus on SC. Creating an in-vivo map of the human midbrain nuclei in a standard space is essential to encourage further functional and structural studies of the regions within this area. To this end, we used a UHF MRI dataset of ten subjects including R2* and Quantitative Susceptibility Mapping (QSM), preprocessed, resliced, and standardized spatially. By fusing the information of two modalities and ten subjects and using manually selected image features we successfully mapped major midbrain nuclei including SC. Calculated features were fed into a deep learning network to create the compressed feature representation of the data and was used in hybrid with a k-means clustering machine to improve the clustering assignment confidence simultaneously with the relevance of the deep features representation. We identified the borders of SC, pars reticulata, pars compacta, and pars lateralis of the substantia nigra, magnocellular and parvocellular red nucleus, corticospinal, corticopontine and fronto-pontine crus cerebri tracts, periaqueductal grey, and inferior colliculus (IC).

Our results reveal the widespread pattern of the human SC neural correlates in the resting state and the relative transformation of the function with respect to the SC depth orthogonal to the tectal plate. Data-driven segmentation of the SC connectivity map splits it up into sub-networks, each comprising areas mainly known for their involvement in peripheral vision, oculomotor system, goal-directed hand actions, and planning. We found no evidence of the human SC being functionally connected to the focal primary visual area in the resting-state. Furthermore, using the UHF structural MRI data we could delineate the borders of the human SC together with the borders of the SN pars reticulata, pars compacta, and pars lateralis, magnocellular and parvocellular areas of the RN, corticospinal, corticopontine, and fronto-pontine crus cerebri tracts, PAG and IC. Keywords: superior colliculus, midbrain, depth-dependent, fMRI, clustering, deep learning, quantitative structural mapping.

Contents

CHAPTER 1 INTRODUCTION

1.1   The Superior Colliculus (SC)

The superior colliculus is a small bilaterally symmetric nucleus located at the top of the midbrain. In mammals, SC is structured in six alternating gray and white layers while an additional layer of fiber called stratum zonale covers the surface of the nuclei (Figure 1.1). Different anatomical characteristics of the layers are the key to describe and understand the functional organization of SC. Each layer, namely, superficial, intermediate, and deep layer consists of a gray layer at the top and follows by a deeper white layer. Moreover, these layers are different in the organization of their inputs and outputs and also in the arrangement and density of the neurons and the fiber distribution (May, 2006). The distinction between different SC layers is clear in the lateral and middle SC where the layers are thick and contain large neurons. However, the layers gradually become thinner in more medial parts of the SC and they become barely distinguishable near the surface (Tardif and Clarke, 2002). The thickness of each layer in humans is poorly studied. However, few studies reported an approximate thickness of 1mm for the superficial SC, although variable across subjects (White and Munoz, 2011).

The superficial layers mainly process visual information conveyed by afferents from the retina, visual cortex, and the frontal eye fields (FEF) (Schneider & Kastner, 2005). In monkeys, the retina sends signals directly to the neurons in the dorsal part of the superficial layers, however, the inputs from the visual cortex arrive at the areas at more depth in the superficial layers (Lund, 1972a). These patterns might be different in other mammals, including humans.

The major inputs to the intermediate layers of the SC are mainly from the superficial layers, and also from those regions of the cortex which are known to be involved in oculomotor control including the lateral intraparietal area of the parietal cortex and the frontal eye field of the frontal cortex. Substantia nigra pars reticulata also provides major

subcortical inputs for the SC. Intermediate layers have a distinguished output that crosses from one side of the brain to the other (the pre-dorsal bundle) and conveys the collicular output to the neurons in the deeper midbrain including regions of the pontine and medullary reticular formation, regions near and possibly within the abducens nucleus, subnucleus B of the medial accessory nuclei of the inferior olive, and cervical spinal cord (Wurtz & Albano, 1980). The critical point is that the pathway crosses the midline at this point so that activity in and above the SC is related primarily to saccades made in contralateral direction, whereas neuronal activity below the SC is related to saccades made in ipsilateral direction. A major ascending output of the intermediate layers is also the frontal cortex through the medial dorsal nucleus of the thalamus.

Deep layers contain multisensory and visuomotor neurons. Neural activation in these layers is associated with eye and head movements based on electrophysiology and behavioral studies in small animals and non-human primates. In general, we can expect a similar neural architecture of the macaque and the human SC, however, many functional features that are currently known from the macaque SC have never been examined in humans. Moreover, a comparison of the result of other studies on different mammalian
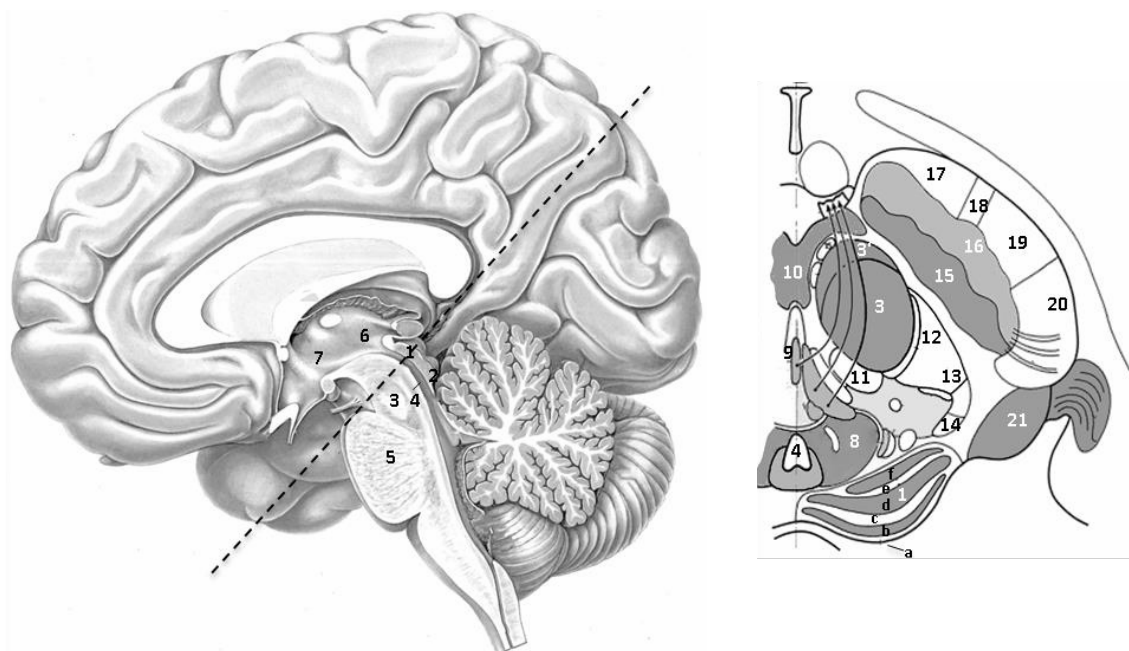
species SC proves incongruence in their anatomy, afferents, and efferents to a certain

Figure 1.1 - Midbrain Anatomy. Sagittal overview of the brainstem (left) and; on the right, transversal sections of the midbrain at the medial part of the superior colliculus (SC) level (indicated by the dotted line on top): 1) SC: a. stratum zonale (StZ), b. stratum griseum superficiale (SGS), c. stratum opticum (SO), d. stratum griseum medium (SGM), e. stratum lemnisci (SL), f. stratum griseum profundum (SGP). (adapted from (Naidich, 2009; Nieuwenhuys et al., 2007) with permission from "Springer Nature")

degree which cast doubt over the complete analogy of macaque and human SC (May,

2006).

1.2 SC Functional Networks

Animal studies reveal a lot about SC functional roles however, it has not been confirmed that the human SC live up to the same purposes. Studies on SC show that its superficial and intermediate layers are involved in visual and auditory orienting as well as visuospatial discrimination and oculomotor functions (Lomber, Payne, & Cornwell, 2001). The deeper layers of the SC including the intermediate and the deep layers are known to be multimodal function units, responding to a manifold of sensory inputs triggered by visual, acoustic, and somatosensory stimulation (Groh & Sparks, 1996; Jay & Sparks, 1987). More specifically, the deep layer is part of a network that establishes goal-directed hand actions. The structural connectivity of the SC is also pretty well studied, however more in animals rather than human subjects. Since there is not much knowledge about the existing SC functional networks, its structural connectivity together with behavioral studies provides a good overview of the expected functional correlates of SC. The location and the size of SC are accountable for its unpopularity as a topic of research. With current imaging and brain signal acquisition instruments, it is very difficult if not impossible to record the SC activity, while it requires an acceptable SNR and proper resolution at brain deep locations. Tectal signals are also pretty contaminated with respiration and heart pulsation noises because of their position relative to the ventricles and the brain vascular system.

It would be even more valuable to capture the dynamic of the SC functional connectivity network against its structure. Despite the complexity of in-vivo SC layers examination, recent advances in magnetic resonance imaging have led to some improvement in midbrain image acquisition, by increased SNR as well as enhanced resolution. This gives the opportunity of gaining a detailed understanding of structures like SC. To further analyze the findings pertaining to the SC functional connectivity networks it is worth figuring out if there is any depth-dependent alteration of connectivity measures. It is also possible to explore whether these alterations follow specific patterns. This would be worthwhile as different articles noted similar brain areas to be connected to different layers of SC. Such cases raise different questions about the fundaments, reasons, and the function of such connections; are all regions connected to SC part of a larger cognitive network designed for a particular behavior, or are they components of smaller sub-networks with distinct functional roles? Does the functional contribution of each SC layer vouch for its specific known structural connections? And does the patterns found explain more about

the specific contribution of SC and its layers to observed human behaviors? Possible answers to such questions are not only valuable for the sake of science and a better understanding of the human brain, but they would also be important for clinical purposes by giving a better picture of brain processes and the reasons for their failure helping with neural disorders prognosis and diagnosis as well as suggesting effective treatments.

1.3 Human SC segmentation

Accurate conclusions about the functional role of brain regions or their axonal connections can be made only if their boundaries are defined precisely. As the outcome of the seed-based studies is reflecting the average voxels behavior, the amount of imprecision in regions definition that an analysis tolerates varies by the size of the region and the total number of voxels that it includes; as an instance, 10 faulty assignment of voxels might be negligible for an area of size 2000 voxels while it is considerable for an area of size 100 voxels. This is the main reason that turns the image resolution into an important factor in mapping relatively tiny brain areas such as SC. In a regular structural MR imaging with isotropic voxels of size 1mm, each SC, approximately, includes 150 voxels. In the case of ultra-high-field MRI (UHF MRI), it is possible to decrease the voxel volumes by 8 to 300 folds which leads to a range of 1200 to 45000 voxels that build each SC. Consequently, by keeping a good balance between the resolution and signal to noise ratio (SNR), UHF MRI makes it possible to map tiny areas like SC with unparallel details and higher precision. UHF helps with precision in two ways; first, the enhanced properties of the image make it easier to correctly classify the voxels into ROI and non-ROI and second, they reduce the confusion at the borders. The border voxels, inevitably, include lumps of both ROI and non-ROI, and smaller voxels can help with improving separation in these areas. On the other hand, depending on the imaging sequence we may capture different properties of the brain areas. That would result in different contrasts that emphasize different features of the tissues. Therefore, to capture more brain structures it is important to consider acquiring images with different adjusted sequences or modalities. A combination of multiple high-resolution MRI modalities is a way to map those brain structures that were formerly difficult to discern, because of their size, location, or tissue type. Our effort here is to map out midbrain nuclei, and SC in particular with the help of UHF MRI and advanced statistics and machine learning methods to encourage future studies of brainstem structures that have remained neglected because of the lack of standardized definition of their location in the human brain.

1.4 Scope and Main Goals

In this thesis, we estimate the functional connectivity network of the human SC and the depth-dependent variation of the functional connectivity that gives rise to the functional sub-networks that the human SC is part of. Besides, we employ advance deep learning methods to map the SC structure and a few more midbrain nuclei. We can divide the goals of this project threefold:

1. Estimating the global brain functional connectivity network (FCN) of the human SC, using a 3T fMRI dataset of the human connectome project (HCP), evaluating the laterality of the SC neural correlates and the depth-dependent analysis of SC FCN at 3T (CHAPTER 2);

2. Evaluating the SC depth-dependent FCN at 7T, using clustering methods to identify the existing patterns in the global brain connections to different layers of SC and define SC functional sub-networks, accordingly. (CHAPTER 3);

3. Segmenting the human midbrain, using UHF structural MRI modalities at 9.4T, and delineating the human SC by utilizing a deep clustering method (CHAPTER 4).

CHAPTER 2 GLOBAL BRAIN FUNCTIONAL CONNECTIVITY OF THE HUMAN SC AT 3T

2.1 Introduction

The laminated structure of the superior colliculus (SC) has been known for decades. Numerous studies on non-human subjects have illustrated the role of SC in attention and goal-directed motor function by the means of controlling eye movements and posture. The pieces of evidence of functions depth association that have been deducted from primates' studies reveal the necessity of layer-level focus in SC probes. Superficial and intermediate layers of SC are involved in visual and auditory orienting as well as visuospatial discrimination and oculomotor functions (Lomber et al., 2001). The deep layer, in the meantime, is part of a network that establishes goal-directed hand actions. It is not possible to attribute a function to a specific layer alone since each of them is a recipient of a diversity of similar sensory inputs. Accordingly, depth-dependent specialization is acceptable only to a limited extent. Finding out about the layer-specific cortical and subcortical connections of SC is a way to better understand how SC functions.

Studies in non-human primates show the superficial layer of the SC receives afferents from the striate cortex (Fries & Distel, 1983), extrastriate cortex (Fries, 1984a), retina (Perry & Cowey, 1984; Rodieck & Watanabe, 1993), and the frontal eye fields (Künzle, Akert, & Wurtz, 1976). The contralateral visual field is mapped on the superficial SC neurons with retinotopically organized receptive fields (Lund, 1972b; Sparks, 1986). There is evidence of the existing connections conveying visual information from the superficial SC to both pulvinar and lateral geniculate nucleus (Huerta, 1984; Stepniewska, QI, & Kaas, 2000), which, in turn, are well-known for their connections to the primary and the secondary visual areas. It has been shown that injection into monkeys brain MT and V3 establishes disynaptic projections from SC (Lyon, Nassi, & Callaway, 2010b).

The deeper layers of the SC including the intermediate and the deep layers are known to be multimodal function units, responding to a manifold of sensory inputs triggered by visual, acoustic, and somatosensory stimulation (Groh & Sparks, 1996; Jay & Sparks, 1987). The deep SC inputs arise from the primary and secondary sensory and the motor cortices is rather sparse and the majority of connections are associated by prefrontal and lateral intraparietal cortex (Clower, West, Lynch, & Strick, 2001; Fries, 1984a; Goldman & Nauta, 1976) involved in the goal-directed hand movements (Borra, Gerbella, Rozzi, Tonelli, & Luppino, 2012a) maintained by the deep SC role in eye-hand coordination (Lünenburger, Kleiser, Stuphorn, Miller, & Hoffmann, 2001), the frontal and supplementary eye fields (Fries, 1984a; Komatsu & Suzuki, 1985; Künzle & Akert, 1977; Künzle et al., 1976; Leichnetz, Spencer, Hardy, & Astruc, 1981; Segraves & Goldberg, 1987; Sommer & Wurtz, 2000), and parietal cortex (Fries, 1984a; Lynch, Graybiel, & Lobeck, 1985) while using thalamic relays to project back to the cortical areas (Harting, Huerta, Frankfurter, Strominger, & Royce, 1980). Auditory information is also mapped within the deep SC layers where inferior colliculus projections converge with visual representation (Huerta, 1984; Sparks, 1986). Macaque brain inferior parietal (PFG and anterior intraparietal [AIP]), ventral premotor (F5p and F5a), and ventrolateral prefrontal (rostral 46vc and intermediate 12r) areas forming a network involved in controlling purposeful hand actions all have relatively dense projections to the intermediate and deep gray layers of the ipsilateral SC (Borra et al., 2012a).

Besides all aforementioned, there are inhibitory interlaminar connections between the cells in the superficial and deep SC with similar receptive fields (Moschovakis, Karabelas, & Highstein, 1988), possibly integrating visual and auditory fields. The nigrotectal pathway has also been described (Beckstead & Frankfurter, 1982; Huerta, Van Lieshout, & Harting, 1991) as well as collicular input to the substantia nigra in a few primate species (May, 2006).

While SC has been extensively studied in non-human animal models with the application of different invasive and non-invasive approaches, the number of studies with human subjects has remained far less. Ethical codes prevent the application of invasive brain-mapping techniques. In addition, the location of the SC makes it a challenge for in-vivo neuroimaging methods to acquire high-quality information from the region of interest. Deep brain signals acquired via Event-Related Potential (ERP) or magnetic resonance imaging technics degrade tremendously compared to the signals coming from less deep

areas. Magnetic resonance imaging in particular is pretty susceptible to CSF and vascular pulsation noises and SC as a deep brain structure is located in the exact adjacency of CSF cavities and the main brain vascular port. However, fMRI approaches are among the best solutions to study the deep brain nuclei as they have been improved a lot in recent years.

Early task-based human fMRI studies suggested that activity in SC increases by the presence of an exploratory contingency and signal in the SC correlates with the frontal eye field (FEF), posterior parietal cortex, and visual association regions (Gitelman, Parrish, Friston, & Mesulam, 2002). "A generalized form of context-dependent psychophysiological interaction analysis unraveled increased illusion-dependent functional connectivity between the SC and some of the main brain areas previously involved in bodily self-consciousness: right temporoparietal junction (rTPJ), bilateral ventral premotor cortex (vPM), and bilateral postcentral gyrus" (Olive, Tempelmann, Berthoz, & Heinze, 2015). Tractography analysis of human DTI consistently identified an approximately ventrodorsally pathway oriented from SC to the parietal cortex (Rushworth, Behrens, & Johansen-Berg, 2006). Probabilistic DTI tractography revealed a streamlined path that passes dorsolaterally through the pulvinar before connecting to the lateral amygdala in both humans and rhesus monkeys (Rafal et al., 2015). Intrinsic connections within superficial layers and radial superficial-layers to deep-layers exist in human SC. These connections are claimed to play role in visual receptive field organization, as well as visuomotor and multisensory integration (Tardif, Delacuisine, Probst, & Clarke, 2005).

We estimated the cortical functional correlates of SC by using the resting-state functional magnetic resonance images. We used a high-quality dataset of 3T rs-fMRI images taken from the human connectome project (HCP) including more than 140 subjects to estimate robust SC neural correlates on the entire cortex. The objective was to estimate the SC functional connectivity with cortical areas independent from any prior knowledge.

2.2 Methods

2.2.1 Participants

We analyzed the magnetic resonance imaging data of 141 subjects (51 males, mean age 27.71 ± SD 3.53; 90 females, mean age 30.66 ± SD 2.66) from the Human Connectome Project (HCP). For a complete description of the inclusion and exclusion criteria of participants in the HCP, please see (Van Essen et al., 2012). Briefly, all participants were between 22 and 35 years old, with no previously documented history of psychiatric,

neurological, or medical disorders known to influence brain function. The selected group for our analysis included 5 left-handed participants, 124 right-handed, and 12 bilateral-handed participants according to Edinburgh Handedness Inventory scores. Subjects' datasets comprised T1-weighted structural and resting-state functional MR images. We chose subjects that had denoised and pre-processed images of all four resting-state fMRI runs available on the HCP database.

2.2.2 MR data specification

T1-weighted images have been acquired using an MPRAGE sequence with 0.7mm isotropic resolution, FOV=224x224 mm, 256 sagittal slices, TR=2400 ms, TE=2.14 ms, TI=1000 ms, FA=8°, Bandwidth (BW)=210 Hz/pixel, Echo Spacing (ES)=7.6 ms, IPAT 2 Acceleration.

Resting-state fMRI data were collected for each subject in 2 sessions, each session consisted of two runs with TE=33.1ms, TR=720ms, and opposite phase encoding directions (left-to-right and right-to-left). Multiband multi-slice-EPI (Feinberg et al., 2010) sequence with experiment specific properties has been used to acquire 1200 volumetric images in each run and multiband factor equal to 8. Please see (Glasser et al., 2013) for further specifications of HCP data acquisitions.

2.2.3 SC seed region definitions

We defined masks of the SC on the 1mm ICBM152 template image in MNI space following the same guidelines as Loureiro et al. (Loureiro et al., 2017). The superior border of the SC is defined by the imaginary line that connects the mammillary body to the superior edge of the tectal plate. The inferior border is identified by a line which is parallel to the one connecting the superior pontine notch to the inferior edge of the tectal plate and starts from the inferior edge of the SC in para-sagittal slices. Finally, we defined an anterior border by the neuroaxis adjacent to the posterior boundaries of the periaqueductal grey (Fig. 1). The volumes of the resulting left and right SC ROIs were 158 mm³ and 141 mm³, respectively.

The entire SC ROI was then segmented into 2 ROIs on each hemisphere. A dorsal SC ROI starts from the surface of the tectal plate on its border with the quadrigeminal cistern and extends 2mm in depth (0-2 mm from the posterior surface of the SC), perpendicular to the surface. The volumes of the resulting left and right dorsal SC ROIs were 79 mm³ and 71 mm³. A ventral SC ROI was constructed by subtracting the dorsal SC

ROI from the whole SC ROI, resulting in ROI volumes of 79mm³ for the left ventral and 70mm³ for the right ventral SC mask.
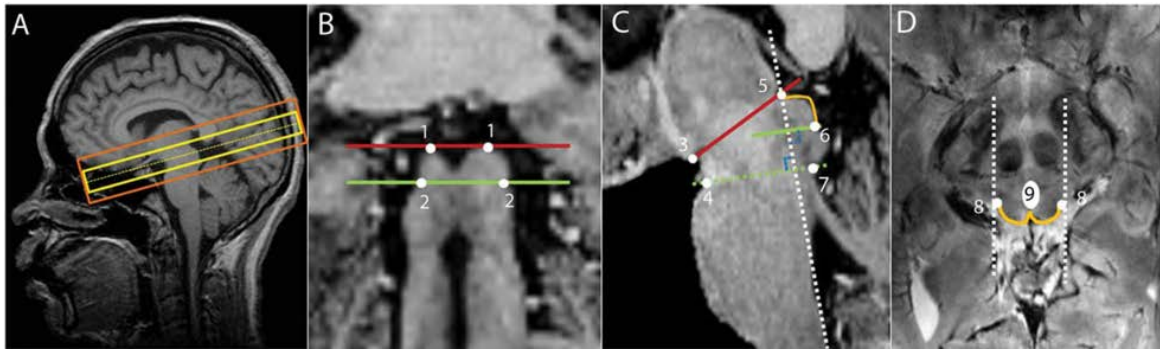

Figure 2.1 - Delineation of the superior colliculus. Reproduced from (Loureiro et al., 2017) with permission of "John Wiley and Sons"

2.2.4 MRI data preprocessing

We analysed images in a combined cortical surface and subcortical volume coordinate system (CIFTI) and used minimally preprocessed HCP datasets which included spatial artifact/distortion removal, surface generation, cross-modal registration, and alignment to standard space (please see Glasser et al., 2013 for details). In short, the structural pipeline includes 3 steps. The first produces an undistorted native structural volume space for each subject, aligns the T1w images, performs B1 bias field correction, and registers the subject's native structural volume space to MNI space. Next, volumes are segmented into predefined structures (including the subcortical parcels used in CIFTI) using FreeSurfer (Fischl et al., 2002). White matter and pial cortical surfaces have been reconstructed. The resulting surfaces are then registered to the Freesurfer's fsaverage surface atlas (Fischl, Sereno, Tootell, & Dale, 1999). The final structural pipeline, PostFreeSurfer, produces all of the NIFTI volume and GIFTI surface along with applying the surface registration (to the Conte69 surface template (Van Essen, Glasser, Dierker, Harwell, & Coalson, 2011)), down-sampling registered surfaces for connectivity analyses, creating the final brain mask, and creating myelin maps. The 91,282 vertices standard grayordinate (CIFTI) space which is used in our analyses is made up of a standard subcortical segmentation in 2 mm MNI space (from the Conte69 subjects) and the 32k Conte69 mesh of both hemispheres.

The "first functional pipeline, fMRIVolume, removes spatial distortions, realigns volumes to compensate for subject motion, registers the fMRI data to the structural, reduces the bias field, normalizes the 4D image to a global mean, and masks the data with the final brain mask". Volumes are then transferred into "CIFTI grayordinate standard space by

mapping the voxels within the cortical gray matter ribbon onto the native cortical surface, transforming them according to the surface registration onto the 32k Conte69 mesh, and mapping the set of subcortical gray matter voxels from each subcortical parcel in each individual to a standard". For more information please see Glasser et al. (2013).

Signals from the SC are potentially contaminated by respiratory and pulsation artifacts, which would be particularly detrimental for resting-state correlation analyses. Therefore, we used the FIX-denoised fMRI images which come with the HCP preprocessed dataset package. The small size of the SC and its location in the adjacency of the quadrigeminal cistern and air cavities make SC signals particularly vulnerable to the propagation of noise through spatial smoothing. Therefore, we left all subcortical structures, including SC, unsmoothed. To increase detection power for cortical areas, we used a geodesic Gaussian smoothing kernel of 3 mm to smooth just surface registered cortical areas.

2.2.5 Seed-based grayordinate-wise functional connectivity

To minimize the field inhomogeneity bias caused by the scans phase encoding direction, we used all four fMRI runs from each subject. Before performing the correlation analysis, time-series of grayordinates from each run were demeaned and normalized. Then, the normalized images of all four runs were concatenated to calculate the average of the preprocessed BOLD time-series across all voxels in each SC ROI. For every subject, the bivariate zero-order (Pearson) correlation was calculated between these seeds' average time-series and each cortical and subcortical grayordinate and converted using Fishers' transform.

To increase the sensitivity of our analyses we tested the resulting correlation values against a physiologically meaningless correlation baseline, i.e. the average of the voxel-wise CSF correlations with the SC ROIs. To this end, we used the probabilistic CSF masks of every individual and rejected any voxel with a probability lower than 1. Next, we calculated Fisher's transform of every CSF voxel's correlation with the SC ROIs average timecourses and used the average of all CFS voxels' z-values within each subject for further statistical analysis.

2.2.6 Statistical analysis

In our first analysis, we calculated two-tailed one-sample t-tests for the Fisher Z-value correlation maps. We used random permutations of the Z-value signs to estimate a

null distribution of maximum t-statistics to control for the family-wise error rate (Blair & Karniski, 1993; Nichols & Holmes, 2002). The null hypothesis rejection threshold (α) was set to 0.05 after 10,000 random permutations.

In our second analysis, we took the abovementioned baseline correlation values between SC ROIs and CSF masks into account And used a paired-sample t-test to test the connectivity values against each subject's average SC-CSF connectivity z-scores which in turn gives the grayordinates with a correlation value that differed significantly from the average CSF correlation. To compare the connectivity patterns between ROI sub-volumes (Left and right, dorsal, and ventral SC) we conducted paired-sample t-tests, using the same maximum t-statistic permutation method to control family-wise error rates.

We mapped significant results of the correlation analyses on the multi-modal parcellation of cortex provided by Glasser et al. (2016) for cortical correlations, on the cerebellum parcellation by Buckner, Krienen, Castellanos, Diaz, & Yeo, (2011); Holmes et al. (2011) for cerebellar correlations, and on the 3D Morel stereotactic atlas of the human thalamus (Krauth et al., 2010) for thalamic correlations.

2.3 Results

In our first analysis, left and right SC revealed widespread bilateral significant correlations with almost the entire medial and lateral occipital cortex, occipito-parietal areas, intraparietal sulcus, superior temporal cortex, and the majority of the lateral and medial frontal cortex (Fig. 2.2 A and 2.3 A). The subtraction of CSF baseline correlations values before statistical testing provided more confined results. While the entirety of the lateral and medial occipital cortex was still significant, suprathreshold results at the parietal, temporal, and frontal cortex were reduced to distinct, smaller clusters (Fig. 2.2 B and 2.3 B). In both analyses, findings based on the left and right SC ROI were mostly equivalent with apparently slightly higher correlation Z-values and resulting t-scores for the left SC (but see the section on laterality below for a direct comparison between correlations with the left and right SC). While significant results in visual, attentional, and oculomotor regions were largely expected, we also observed significant results along the posterior bank of the central sulcus and the ventral bank of the middle frontal gyrus. The comparison between CSF-controlled suprathreshold t-maps in (Figures 2.2 and 2.3) B with Fisher-transformed correlation maps in the respective panels C shows that higher, significant t-values corresponded with higher correlation values. In the following, we will first focus on

ipsilateral correlations of either colliculus with the cerebral cortex, basal ganglia, thalamus, and cerebellum based on our second statistical analysis, taking CSF correlation baseline into account. Then, we will look at laterality effects and conclude with the results of a comparison between dorsal and ventral SC ROI correlation maps.

2.3.1 Occipital cortex

Looking at the cortical surface connectivity map, the layout of V1 clearly stands out. The hotspot patterns also follow the layout of V6 and the dorsal visual transitional area (DVT). A less strong co-activation, yet neatly delineated, with visual areas V2, V3, V4, ventromedial visual areas 1 and 3 (vmv1 and vmv3) and pro-striate cortex (ProS) is also discernible. There is also an extensive cluster of the occipital cortex in the lateral view which mainly encompasses ROIs V3CD, V3A, V6A, V7, and lateral occipital area 3 (LO3).

2.3.2 Parietal cortex

Even more pale connectivity to the posterior cingulate visual area (PCV) is existent. It is also possible to find another weak connection to area 23c. The fact that the activation pattern completely matches the elongated geometry of the ROI makes it more considerable.

Reaching out from the occipital cortex to the posterior part of the parietal cortex, we would notice patches at the inferior parietal cortex (PGp, IP0). Looking at the inferior parietal cortex, the co-activation in medial, dorsolateral, ventral, and anterior intraparietal areas is evident. Extending to the medial surface, we can trace the connectivity to a lesser extent in the 7AM area. Inferior to the AIP and moving towards the central sulcus we can also find portions of PF complex and PF opercular (mostly right SC), area 2, and PFt (mostly left SC).

We found significant correlations along the somatosensory areas 3a and 3b, essentially reaching from a frontal superior FEF and area 4, and parietal area 3a/3b eye-related complex in ventral direction to the face and tongue representations, where significant correlations are mostly confined to 3a/3b

2.3.3 Temporal cortex

Examining the temporal cortex connectivity, one cluster reaches from lateral occipital areas into temporal areas FST and the medial superior temporal gyrus (MST) while it does not include MT. We can also recognize another cluster with slightly stronger connectivity at the border of posterior inferotemporal (PIT) and area PH. The temporo-

parieto-occipital junction areas 2 and 3 (TPOJ3 & TPOJ2) and PHT also show a faint correlation with SC. While all these areas extend from significant findings in instantly neighbored occipital areas, a delineated cluster located almost exactly in the superior temporal visual area STV stands out from a surrounding of non-significant, lower correlations.

2.3.4 Frontal cortex

At the lateral premotor cortex, we found the expected clusters of significant, higher correlations at the frontal and premotor eye fields (areas FEF and PEF), while area 55b in-between showed contrasting lower correlations. In both hemispheres, we found significant correlations in the primary motor cortex area 4 posterior to FEF and extending into the posteriorly neighbored parietal somatosensory areas 3a and 3b.

Anterior and inferior to PEF, we found a ribbon of slightly higher, significant correlation peaks in inferior frontal areas IFJp, IFJa, IFSp, and IFSa, which stand out from a neighborhood of lower correlations in the ventro- and dorsolateral cortex with the only exception of smaller significant spots in dorsolateral area 46. We also found dispersed smaller spots in the medial anterior cingulate areas and supplementary and cingulate eye fields (SCEF).

Figure 2.2 - The entire left SC cortical map of: A) correlation z-score one-sample t-test with critical-t equal to 4.6, B) correlation z-score paired-sample t-test with critical-t equal to 5.2 for testing the connectivity values against the distribution of each subject's average SC-CSF connectivity z-scores, C) group average of SC connectivity z-scores.

Figure 2.3 - The entire right SC cortical map of: A) correlation z-score one-sample t-test with critical-t equal to 4.66, B) correlation z-score paired-sample t-test with critical-t equal to 5.21 for testing the connectivity values against the distribution of each subject's average SC-CSF connectivity z-scores, C) average subjects' SC connectivity z-scores

2.3.5 Thalamus and basal ganglia

The results show a strong connection between SC and almost the entire body of the thalamus with a predisposition towards its medial and posterior parts (Figs. 4 and 5). The thalamus nuclei that fall into these areas are central lateral (CL), centre median (CM), Habenular nucleus (Hb), Limitans (Li), anterior and medial pulvinar (PuA and PuM), Parvocellular part of the mediodorsal nucleus (MDpc), posterior and the lateral posterior nuclei (Po and LP).

SC also appears to have connections to relatively small parts of the basal ganglia. There we found clusters at the dorsal wall of the caudate nuclei in addition to the less significant group of voxels at the posterior tip of the putamen.
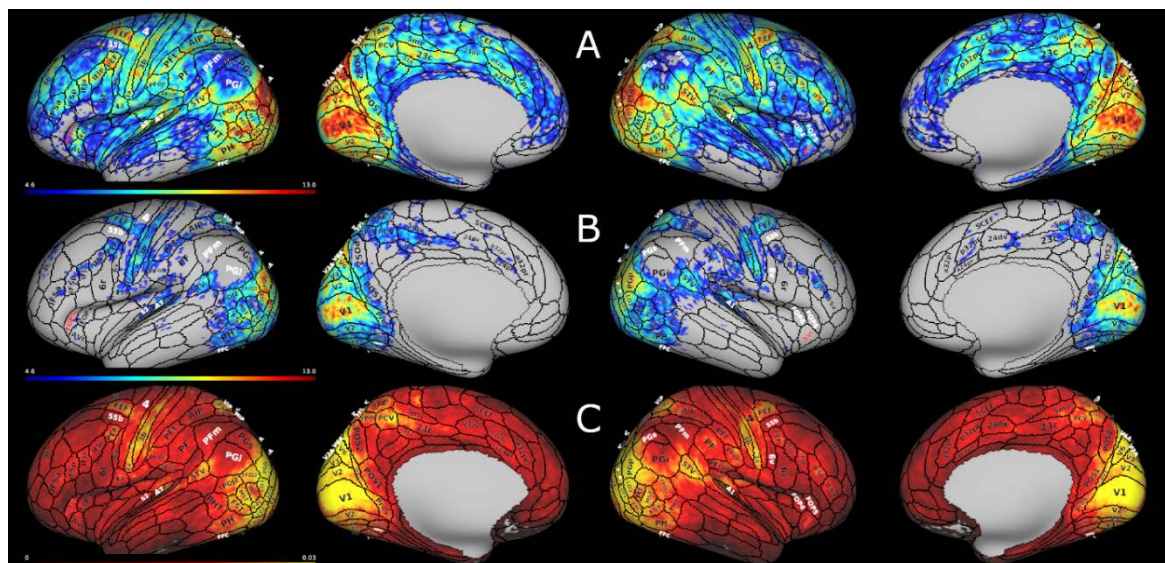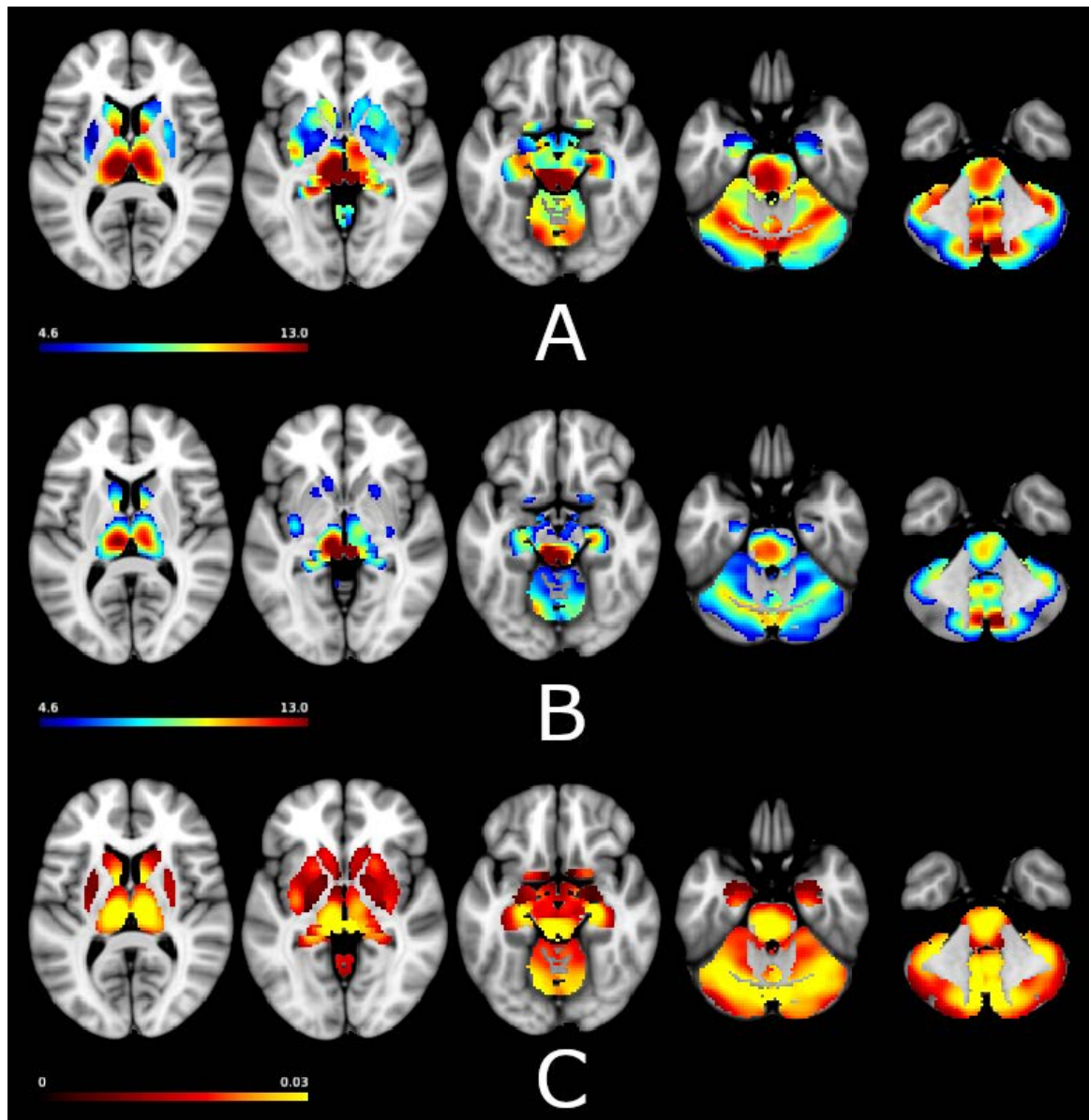
Figure 2.4 - The entire left SC sub-cortical map of: A) correlation z-score one-sample t-test with critical-t equal to 4.6, B) correlation z-score paired-sample t-test with critical-t equal to 5.2 for testing the connectivity values against the distribution of each subject's average SC-CSF connectivity z-scores, C) average subjects' SC connectivity z-scores
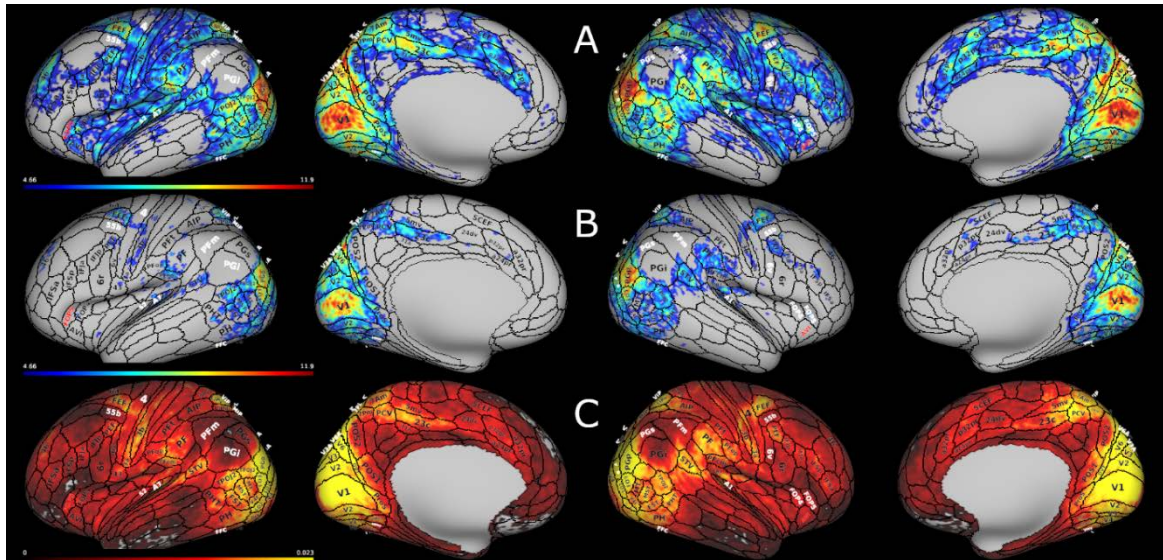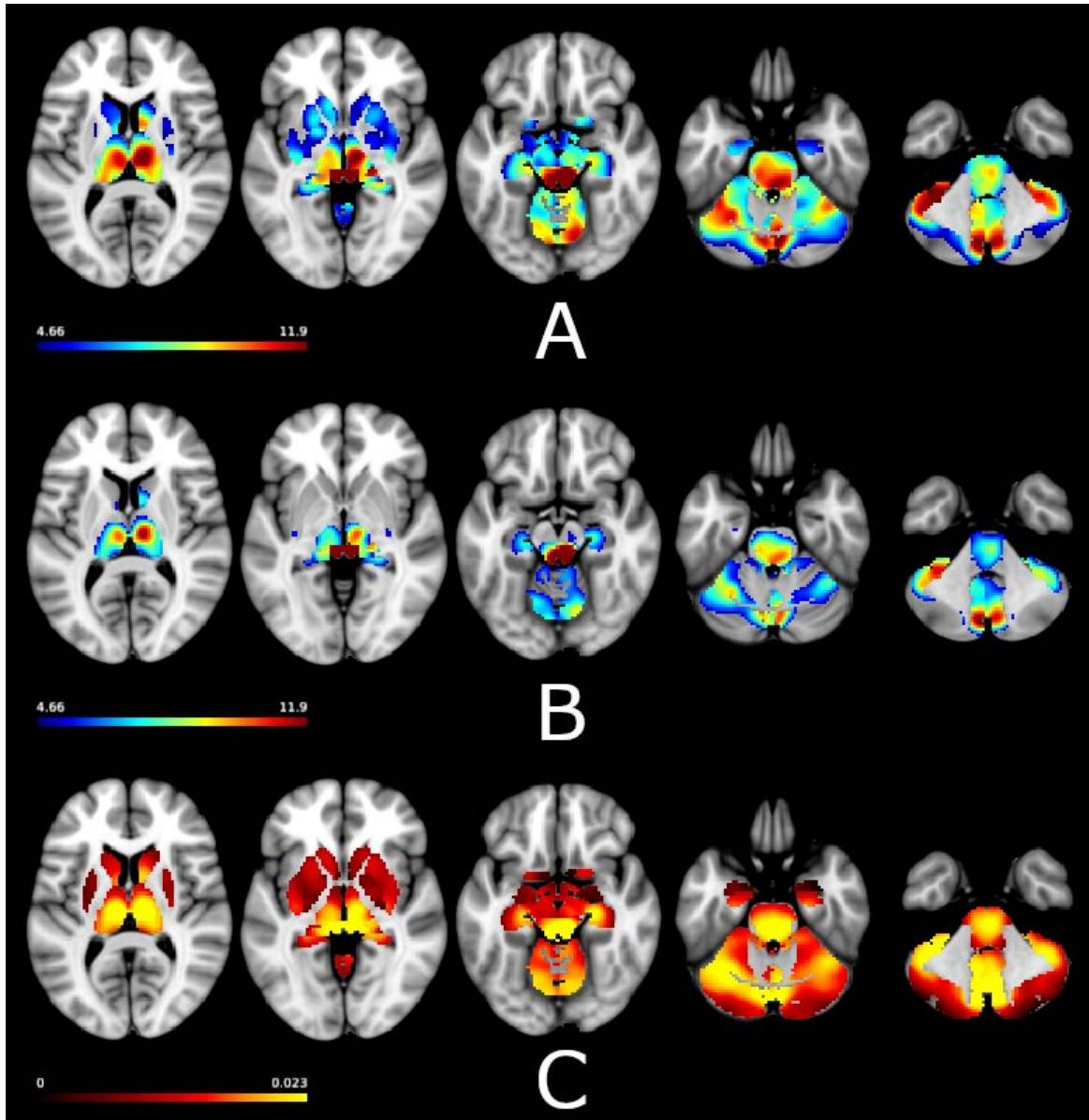
Figure 2.5 - The entire right SC sub-cortical map of: A) correlation z-score one-sample t-test with critical-t equal to 4.66, B) correlation z-score paired-sample t-test with critical-t equal to 5.21 for testing the connectivity values against the distribution of each subject's average SC-CSF connectivity z-scores, C) average subjects' SC connectivity z-scores

2.3.6 Cerebellum

Consistent with the nature of our analysis, we used the cerebellum parcellation by (Holmes et al., 2011). to assess cerebellar SC correlates. This atlas was estimated based on the cerebral functional connectivity of the cerebellum. The connectivity pattern at the cerebellum is pretty symmetrical with an ipsilateral predisposition in terms of strength and spatial distribution extent of the significant clusters. SC shows strong connectivity to a large patch of voxels including parts of areas 5, 6, and 12 located in VIIB lobule with an approximate center at (8, -74, -44) MNI coordinates. We detected another cluster in the lowermost rostral region of the cerebellum in the sagittal plane comprises portions of areas 6 and 7 laid at VIIIB and also VIIIA to a smaller extent, roughly centered at (14, -46, -48).

The next group of voxels, spanning from the left to right side of the cerebellum, covers the entire lobule VI which makes the superior part of area 7. The remaining voxels with significant correlation are encompassing parts of areas 16 (lumps of lobules Crus II, VIIB, and IX) and small pieces of areas 4 and 11 that correspond accordingly to lobules V and VIIIB.

2.3.7 Laterality

The results of the individual left and right SCs showed abundant identical connections between the cortex and the respective SC. Any difference between left and right SC connectivity could only be found with uncorrected statistics (Fig. 6). These results showed a predominance of the left SC connectivity strength over the right SC in areas inferior frontal gyrus, a large extension of the Broadmann area 8 and superior and inferior parietal gyrus (PGi and PGs), supramarginal gyrus (PFm), superior temporal sulcus (STSdp and STSvp), posterior temporal cortex (TE1p), and area 9m. Left SC does not keep overruling right SC on the right hemisphere except for the minute scatters on PGi and primary sensory-motor cortex.
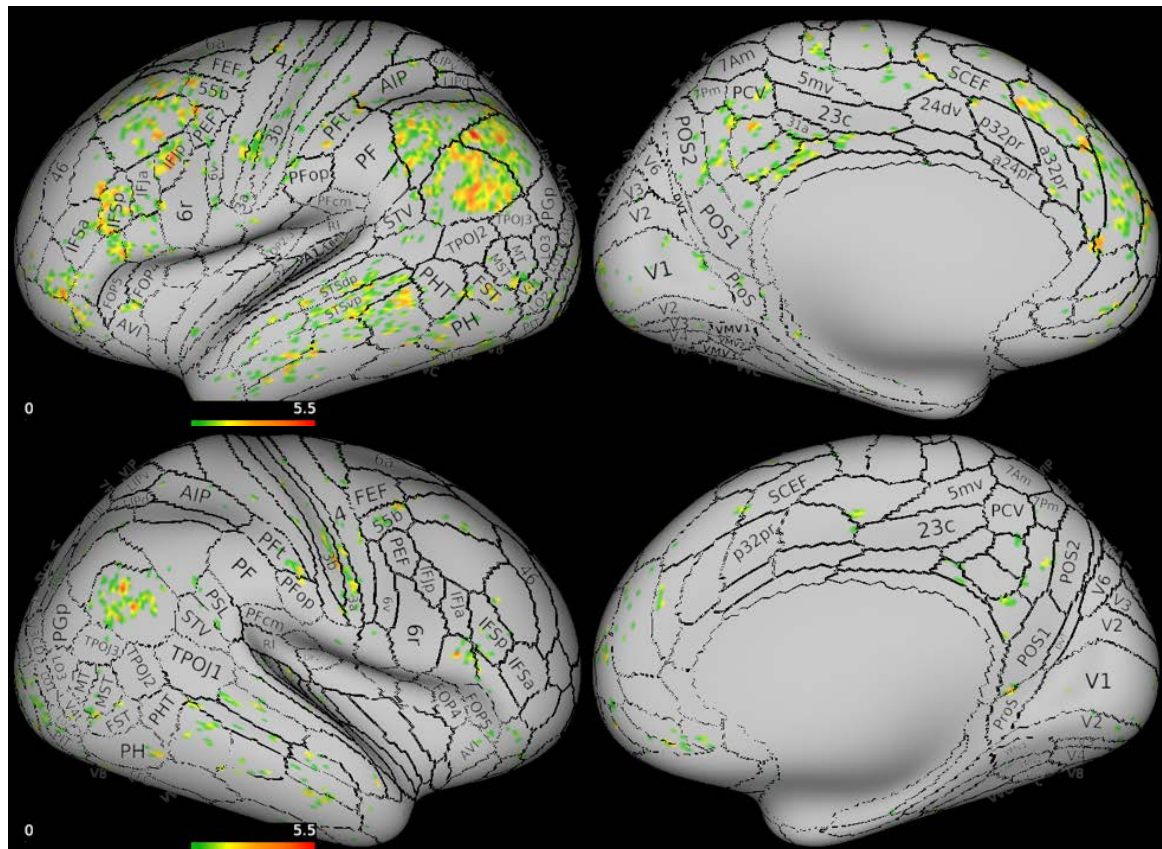
Figure 2.6 - Connectivity dominance (left SC > right SC) uncorrected statistics A) left hemisphere, B) right hemisphere.

Looking at the connectivity of the right SC, the general co-activation pattern is very similar to the one from the left SC connectivity map while the correlations are less significant and of lower values in most areas (Figure 2.5).

2.3.8 Depth-dependent connectivity

Exploring the connectivity of the dorsal and ventral zones on each hemisphere showed that the DZ correlation layout is more widespread where no exclusive connectivity exists for the VZ. To further investigate the observation we performed a permutation test based on maximum t-statistics (Figures 2.7 and 2.8) and it reveals the connectivity layout of the VZ is a subset of the DZ connectivity map, while no independent cortical functional correlation could be found at the ventral zone.
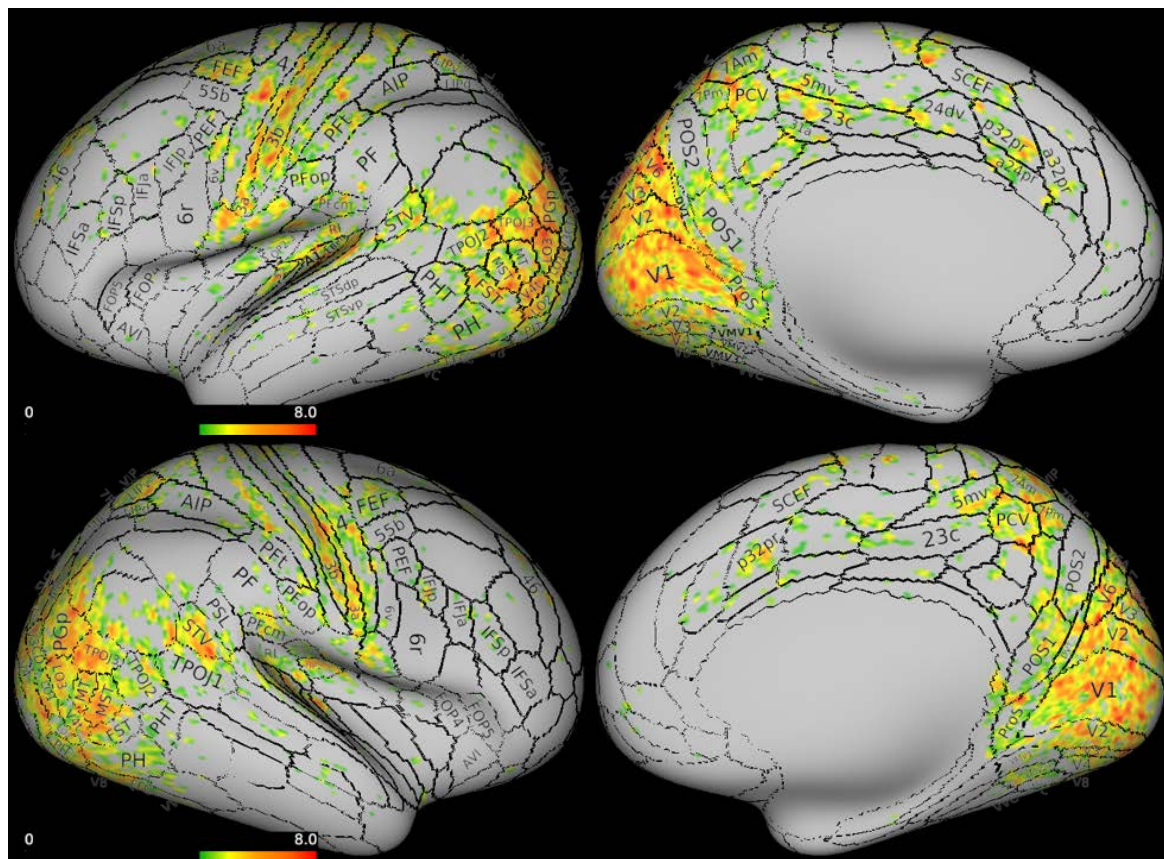
Figure 2.7 - Comparison of left DZ > left VZ after controlling for family-wise error rate, using the T_{max} permutation test. A) left hemisphere, B) right hemisphere.
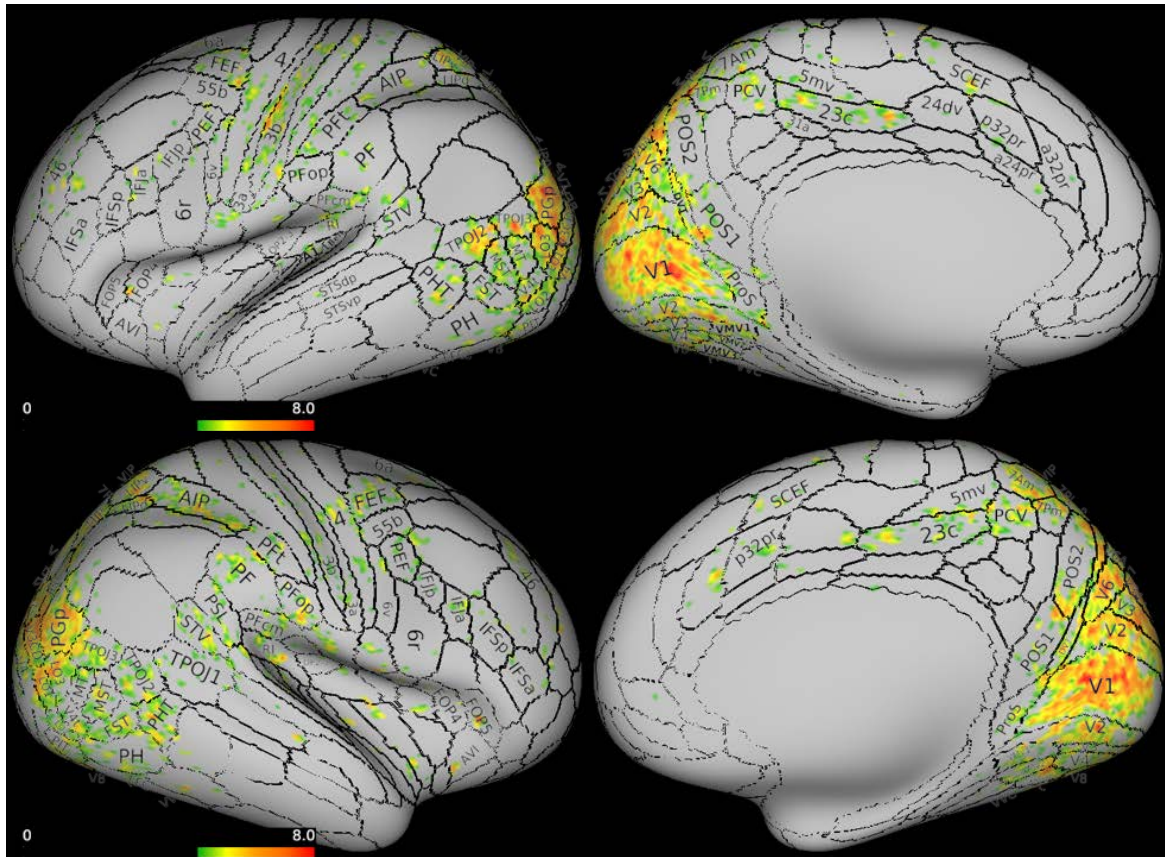
Figure 2.8 - Comparison of right DZ > right VZ after controlling for family-wise error rate, using the T_{max} permutation test. A) left hemisphere, B) right hemisphere.

2.4 Discussion

We successfully demonstrated a coherent network of neuronal nodes formed around superior colliculus. Zero-order correlation analysis enabled us to create a picture of the SC neural correlates during the so-called brain resting state, in which fMRI measures spontaneous blood-oxygen-level-dependent (BOLD) signals. So far, the power and the precision of in-vivo imaging instruments and analysis tools were insufficient to record and extract a clear signal from a small and deep structure as SC in whole-brain volume measurements. Recent advances in MR imaging quality and image preprocessing methods developed by the human connectome project provided us with the possibility of studying SC of a living human brain.

Most we know about human SC function heretofore is based on extensive non-human species SC neural wiring or functional studies. Most prominently from the 70's, the distinctive functional behavior of the SC zones started to receive more attention (Casagrande, Harting, Hall, Diamond, & Martin, 1972; Harting, Hall, Diamond, & Martin, 1973; Lund, 1969; Mohler & Wurtz, 1976; Wurtz & Mohler, 1976). The study of the cortical projections to the SC of macaque monkeys by Fries (1984a) is a great showcase of

neural distribution of the cortical synapses ending up in SC in which it shows that the injections into the different depth of SC result in different, but consistent dispersion patterns of the labeled cells. Likewise, by conducting functional connectivity analysis of the SC average signal, we found a widely distributed, meanwhile, sound cortical coactivation pattern. A comparison between human and macaque SC connectivity reveals fundamental analogy in most cortical areas and concurrently major dissimilarity in others.

2.4.1 Cortex

We showed that the whole body of the SC is significantly correlated with clearly delineated sub-volumes of the visual cortex. Laterally, it extends from lateral occipital areas to the inferior parietal cortex and the temporo-parieto-occipital junction, while the superior temporal visual area also stands out more like an isolated patch. On the medial surface, it includes visual areas 1 to 4 beside visual area 6 and ventromedial visual areas and dorsal transitional visual area in addition to the pro-striate cortex and it ends at the parieto-occipital sulcus. It has been known that SC is densely connected to the primary visual area for decades. There is also evidence of SC projections to the dorsal visual stream, which is known for a high temporal frequency and sensitivity to motion and capability of fast response by circumventing the primary visual area (Collins, Lyon, & Kaas, 2005; Kaas & Lyon, 2007; Lyon et al., 2010b; Wang & Burkhalter, 2013). Our study result pictures SC beside the principal elements of the dorsal stream on the occipital cortex together with the posterior parietal cortex. Major correlated areas on the parietal cortex are interparietal complex and medial area 7 which together are involved in attention, locating object position in space, reaching, and grasping the located object. All aforementioned evidence supports the assumption that human SC, as well as in many non-human species, serves the role in fast visual responses (Boehnke & Munoz, 2008; Courjon, Olivier, & Pélisson, 2004; Dean, Redgrave, & Westby, 1989; Morris, Öhman, & Dolan, 1999) and visually guided behavior (Sprague, 1966; Werner, 1993).

Furthermore, our investigations show functional connections between SC and frontal eye fields (FEF), premotor eye fields (PEF), and supplementary eye fields (SCEF). The same network has been detected in different studies, showing a multitude of projections from mentioned cortical eye fields to SC in non-human primates; together, playing role in the control of visual attention and generation and control of eye movements (Huerta & Kaas, 1990; Luppino, Rozzi, Calzavara, & Matelli, 2003; Parthasarathy, Schall, & Graybiel, 1992; Small et al., 2003).

An interesting and unexpected piece of the puzzle is the significant correlations between SC and primary hand motor and inferior frontal areas. Goal-directed hand movement has been widely studied. The major cortical areas contributing during reaching and grasping trials in primates are known to be inferior parietal, dorsal and ventral premotor, ventrolateral prefrontal, and primary motor cortex (Borra et al., 2012a; Castiello & Begliomini, 2008). Borra and colleagues found projections from anterior intraparietal (AIP), ventral premotor (PMv), and ventrolateral prefrontal areas to the intermediate and deep layers of ipsilateral macaque monkeys SC. They suggested that the information provided for SC through these areas is used to facilitate the control over orienting behavior toward targets of the visually informed object-oriented hand actions. Beforehand, Fries and colleagues studied cortical projections to the SC (Fries, 1984a). They observed projections from the primary motor (area 4) and premotor (area 6) hand areas as well as the prefrontal cortex (area 9) to the intermediate and deep layers of the SC. They could also detect projections from FEF and posterior parietal cortex. Looking back at our functional connectivity maps, SC connection to the primary hand motor area is evident, while connections to the premotor cortex, in particular, the corresponding area 6 of macaque's brain are present, but with relatively noticeable less strength. We are also able to find a very clear patch stretched along the inferior frontal junction and inferior frontal sulcus, covering four functionally distinct areas. As we still do not know much about the human brain homolog of the ventrolateral prefrontal area of the macaque's brain, the interpretation of our findings pertinent to the SC functional correlates in inferior frontal areas would remain debatable. These later observed differences between our study results and non-human brain findings could be simply explained by the incongruity of different species brains, while the dissimilarity might not only be caused by the heterogeneity of the structural organization, but also discordant functional properties. We should also keep in mind that what we have investigated here is the systematical functional accordance of the signals which does not necessarily match the underlying structural configuration.

2.4.2 Thalamus

We found an extensive connection between SC and many thalamus nuclei, which are mostly located in the caudal and lateral parts of the thalamus. There were significant correlations with non-specific nuclei of the intralaminar thalamus which has widespread connections to the cortex. The connectivity map shows SC being strongly connected with posterior intralaminar nuclei (CM and PF) which are known to receive inputs from the

premotor and motor cortex (Akert & Hartmann-von, 1980; Chiba, Kayahara, & Nakano, 2001; Künzle & Akert, 1977). CM also projects to most of the sensorimotor area of the striatum in dorsolateral caudate and putamen (Sadikot, Parent, & Francois, 1992). SC has been also connected with part of the anterior intralaminar thalamus including CL where the motor cortex and parietal cortex provide inputs to the area (Akert & Hartmann-von, 1980; Künzle & Akert, 1977). It has been proposed that the anterior intralaminar nuclei are part of the oculomotor thalamus and play a role in arousal and visual awareness (Purpura & Schiff, 1997). As an instance, anterior intralaminar neurons have shown motor-related or both visual and motor-related responses (Wyder, Massoglia, & Stanford, 2003).

Our findings also show a strong connection between SC and parvocellular mediodorsal nuclei. MD influences multiple cognitive abilities via its interactions with areas of the frontal lobe, such as dorsolateral PFC and anterior cingulate cortex (Dermon & Barbas, 1994; Ouhaz, Fleming, & Mitchell, 2018; D. Xiao, Zikopoulos, & Barbas, 2009). It has been shown that there is a direct connection between parvocellular MD and the DLPFC (Klein et al., 2010). The human counterpart of monkey DLPFC is thought to be found right above the inferior frontal gyrus (Rajkowska & Goldman-Rakic, 1995), which could be the match for our significant finding, as SC correlated voxels stretching from posterior inferior frontal junction to the anterior inferior frontal sulcus. We are still not able to confirm whether the connection between SC and the inferior frontal stripe is direct or it is being facilitated or regulated by thalamic substructures like MDpc (Pergola et al., 2018).

(Figures 2.2 and 2.3) also show connections to the anterior and medial pulvinar. Pulvinar is best known for its role in regulation and synchrony of the signals reaching the visual cortex and also its involvement during saccadic eye movements, but interestingly, another action has also been reported which is signaled by cells of the pulvinar nuclei and that is reaching by arm to a target. Cells that are active during such activity are found in essentially all of the pulvinar nuclei, although they have been reported to be more concentrated in oral (ventral) and upper part of the lateral nuclei (Acuña, Gonzalez, & Dominguez, 1983; Hardy & Lynch, 1992). And binocular eye-movement-signaling is transmitted to the SC from parietal cortical area LIP (Gnadt & Beyer, 1998), perhaps via fibers that also synapse within the lateral or medial pulvinar (Rockland, 1998). Alongside, we detected significant correlations to the Po and LP nuclei which appear to be important in various visual functions such as visually guided behaviors and reflex responses to threatening/fear-related stimuli (Goossens, Schruers, Peeters, Griez, & Sunaert, 2007;

Grieve, Acuña, & Cudeiro, 2000; Morris et al., 1999; Wei et al., 2015; Wurtz, McAlonan, Cavanaugh, & Berman, 2011). We were not able to find enough evidence that explains the circumstances upon which Hb and Li nuclei are connected to SC.

2.4.3 Cerebellum

Utilizing the functional cerebellum parcellation, made it possible to find the cortical correlates of the cerebellum areas having a significant correlation with SC. By looking at the cortical correlates of the mentioned cerebellar regions altogether, its resemblance with the SC cortical connectivity map is immediately discernible. Out of thirteen cerebellar lobules, SC appeared to be fully or partially connected to seven, which were located in the posterior lobe, excluding lobule V. Out of all correlated cerebellum ROIs, only ROI 16 showed a cortical connectivity pattern inconsistent with the SC cortical connectivity map. Parcellation area 16 which covers part of lobules CrII, VIIB, and IX is functionally connected to inferior and superior PG (angular gyrus), 7m (precuneus), posterior part of area 31 (posterior cingulate cortex), posterior and anterior parts of area 24 (ventral anterior cingulate) and rostral and dorsal parts of area 10 (dorsomedial prefrontal cortex), which are parts of default mode network (Long et al., 2008), The rest of the co-activated cerebellar areas show the same cortical connectivity pattern as SC.

2.4.4 Correlation analysis

The results presented here might raise an important question. How could very minute coefficients values of correlation be statistically significant? And where these were significant in a large group analysis, would these values and differences have any meaningful and ecologically valid interpretation. The value of the 98% percentile of the Fisher-transformed correlation values did not exceed 0.03 in our study, which from the mathematical point of view would be interpreted as uncorrelated. On the other hand, by applying the popularly accepted p-value thresholds one can notice that every tiny effect would become significant because of its consistency across the large group. Panels A in (Figure 2.5) shows what an uncontrolled big data analysis would result in by exerting conventional statistical analysis. We can better understand this phenomenon by looking at other examples of big data analyses. The advantage of a large population, high-dimensional data is that it provides enough power to disclose subtle underlying effects in the data which could not be detected in smaller samples. At the same time, high-dimensional data introduces some unique statistical challenges including noise accumulation, spurious

correlation, and incidental endogeneity which need to get addressed (Fan, Han, & Liu, 2014). All these together would leave us with many significant outcomes, which might simply result from the aforementioned effects.

From another perspective, it is not possible to deal with large samples using the conventional rules of statistical inference. Statistical inference is based on the notion of the null hypothesis, and by picking a particular number representing the "no effect" state for testing high-dimensional data result, the estimates become so precise that every minute effect would have significant distance from the "no effect" state (Lin, Lucas Jr, & Shmueli, 2013). Hence, choosing the p-value in the common range of 0.01-0.05 is simply not discriminative. This is the reason why some studies have chosen very small p-values (Lin et al., 2013) which, first, is computationally very expensive to calculate and second, is not helpful, since there is no gold standard to choose a particular threshold for p-value when it comes with so many floating points.

Another issue is that the calculated correlation coefficient distribution characteristics vary by dataset; depending on the level of residual noise, as well as the brain region under study. In a former study on 24 HCP subjects by Vu et al. (2017) they showed that the correlation values for a cortical seed at posterior parietal cortex would lie within the range of 0.5 and below where with the same analysis for the sub-cortical seed at putamen, correlation values hardly reached beyond 0.1. It is imaginable that the maximum correlation value would fall even more for a deep tiny region such as SC located in the adjacency of different noise sources contributing to the respective correlation seed signal.

To be able to tackle the high-dimensional data analysis issues we corrected our statistical test by choosing a very conservative method to select a varying null-hypothesis for every subject instead of zero, which was equal to the average of the correlation values between the chosen SC ROI and every voxel in the subject-specific CSF mask. Since this latter correlation should have no physiological meaning, we chose it as the state of "no effect" and filtered out the values which did not have a significant distance from that value.

2.5 Conclusions

Studying human mesencephalic nuclei and structures has been an implausible job with a variety of obstacles that need to be overcome. With the help of state-of-art fMRI sequences, improved preprocessing algorithms, and improved statistics, we provide a map of human superior colliculus global circuitry.

The SC connectivity map widely agrees with the findings from animal studies. However, significant correlations were also found in the prefrontal, posterior temporal, premotor, and primary motor cortex, i.e. in locations with little evidence of connections to the SC from animal models. These findings confirm recent observations that functions of the SC reach far beyond vision and oculomotor control. The parallel connectivity between SC and inferior/middle frontal area, posterior superior temporal visual area, and neck and shoulder tail of the primary motor cortex demonstrates the involvement of the SC in a multiplicity of cortical networks and functions. These include responses to moving objects, target selection, and postural control.

Being able to study such a deep structure with the use of non-invasive methods is a promising achievement. Besides, the resting-state functional network of the human SC can usher future SC-related researches with additional evidence for better experiment designs, which might eventually lead to a better understanding of the role of SC and the consequences of its dysfunction. We believe that higher quality data, together with a large enough sample size and proper analysis methods would provide a chance to further increase our knowledge about SC functional circuitry. Simultaneous use of other modalities is another key to reach a better understanding of the SC role in maintaining vital human brain functions.

CHAPTER 3   DEPTH DEPENDENT FUNCTIONAL NETWORKS OF THE HUMAN SC

3.1 Introduction

It has been known for decades that the superior colliculus (SC) anatomical structure is laminar. Six layers of the grey matter and the white matter one after the other, positioned in parallel with the tectal plate are forming the structure of the SC (May, 2006). Meanwhile, SC is known to be one of the early locations in the brain involved in multimodal integration of the sensory inputs. Multimodal integration is important to all living species, as it helps to perceive a coherent representation of surroundings and come up with a timely and appropriate behavior or reaction. It has been shown that SC collects visual, auditory, and tactile inputs and sends motor efferent, essentially, posture-related motor commands and enforcing specific eye movements, simultaneously. Many studies show that the functional compartments of SC are not randomly distributed over the structure, and each resides in a particular anatomical location. The mentioned fact suggests the plausibility of the SC functional properties inherent correlation with its laminar structure.

A comprehensive study on macaque monkey by injections restricted primarily to the superficial layers of the SC has found labeled cells in the visual cortex and both in the frontal eye field and the adjacent part of the premotor cortex (Fries, 1984b). The same study reported that the injection to the intermediate and deeper layers of the SC projects to the posterior parietal cortex, inferotemporal cortex, auditory cortex, the somatosensory representation SII, upper insular cortex, motor cortex, premotor cortex, and prefrontal cortex.

The intermediate layers of SC show sensory and saccade-related responses. The motor map in the intermediate layers corresponds to the visual sensory map on the superficial layers (Sparks, 1981). A dense fiber projection from the inferior bank of the intraparietal sulcus to the intermediate and deep layers of the superior colliculus was

observed. In contrast, only faint labeling was seen in the superior colliculus following injections into area PGc on the convexity (Lynch et al., 1985). Deep SC layers are centers for multimodal integration. There are numerous pieces of evidence of the presence of a map of auditory space in the deep layers of the SC (Gaese & Johnen, 2000; Jay & Sparks, 1987). Intermediate and deep layers are also being mentioned as part of the lateral grasping network, having connections to the dorsolateral prefrontal cortex (DLPFC), ventral premotor area, and the anterior intraparietal lobule (AIP) (Borra, Gerbella, Rozzi, Tonelli, & Luppino, 2012b).

The superficial layers of the SC are receiving retinal information (Sparks, 1981). They provide disynaptic input to dorsal areas MT and V3, not V2 or ventral area V4 (Lyon, Nassi, & Callaway, 2010a). The retinotectal projection is distributed primarily to the superficial layers (Lund, Land, & Boles, 1980; Pollack & Hickey, 1979), it has been observed that an indirect pathway via the cortex also sends visual sensory information to this layer (Marrocco, 1978). Observations in monkey studies indicate that primary and secondary visual areas are all providing retinotopic inputs only to the superficial SC and not the layers beneath (Lui, Gregory, Blanks, & Giolli, 1995; Tigges & Tigges, 1981), while the distribution of this connections must be pretty uniform over the area, according to an older study (Wilson & Toyne, 1970). However, in macaque, the area 19 projection extends into the intermediate layers (Lui et al., 1995).

One of the most well-characterized connections of the superficial SC is to the dorsal lateral geniculate nucleus (Wilson, Hendrickson, Sherk, & Tigges, 1995). The lower sublamina of the superficial SC also provides a major projection to the pulvinar/lateral posterior (Pul/LP) complex of the thalamus (Benevento & Standage, 1983; Huerta & Harting, 1983).

Some studies suggest that there is a close bind between SC and the components of the oculomotor system including frontal eye field (FEF), premotor eye field (PEF), precuneus, and lateral intraparietal area (LIP) (Büttner & Büttner-Ennever, 1988; Lynch & Tian, 2006; Müri, 2006). The SC is well-connected with the cortical eye fields to collaboratively control the gaze movement. Corresponding areas in the monkey brain include FEF, the supplemental eye field (SEF), and the parietal eye field which includes area 7A and lateral intraparietal cortex (LIP) (see Leichnetz et al., 1981; Leichnetz and Gonzalo-Ruiz, 1996; Moschovakis et al., 2004; for a broader interpretation), its human brain homolog presumably are areas 7A, LIPv, and VIP (Müri, 2006; Müri, Iba-Zizen,

Derosier, Cabanis, & Pierrot-Deseilligny, 1996; Van Essen et al., 2001). These connections are terminating in the intermediate SC with some reporting a scattered projection to the superficial layers (Huerta, Krubitzer, & Kaas, 1986; Komatsu & Suzuki, 1985; Leichnetz et al., 1981).

It has been noted that different areas of the FEF project to different layers of SC are based on saccade amplitudes. The area responsible for large saccades is only connected to the intermediate and deep layers and the connections from FEF areas responsible for small saccades terminate at the intermediate layers (Komatsu & Suzuki, 1985; Stanton, Goldberg, & Bruce, 1988). Observations about the SEF are more inconsistent, termination of its connections to the SC was observed both in the intermediate layers (Huerta & Kaas, 1990) and superficial layers for contralateral SC and intermediate layers for the ipsilateral SC (Shook, Schlag-Rey, & Schlag, 1990). Studies also show that the parietal eye field projections converge on the deeper sublamina of the intermediate SC, where the saccade-related neurons are located (Lynch et al., 1985).

SC relation to the eye fields is rather reciprocal. It means that it provides them with information through thalamic nuclei as well as receiving input signals (Harting et al., 1980; Yamasaki, Krauthamer, & Rhoades, 1986). Central lateral nucleus (CL) and the parvocellular medial dorsal nucleus (MDpc) are among the most important thalamic regions which facilitate the connection between SC and the cortical eye fields (Beckstead, 1979; Huerta & Kaas, 1990; Huerta et al., 1986).

According to previous studies, SC is involved in stimulus-driven and also goal-driven attention and embedded in corresponding cortical networks (Bell, Fecteau, & Munoz, 2004; Fecteau, Bell, & Munoz, 2004; Rafal, Posner, Friedman, Inhoff, & Bernstein, 1988; Sapir, Soroker, Berger, & Henik, 1999). The dorsal attention network enables the goal-driven attention and links it to appropriate motor responses and the ventral attention network maintains the stimulus-driven attention (Corbetta, Patel, & Shulman, 2008). A dorsal attention network includes the parietal cortex, particularly intraparietal sulcus (IPS) and superior parietal lobule (SPL), and the dorsal frontal cortex along the precentral sulcus, near or at the frontal eye field (FEF). And the core regions of the ventral network are the temporoparietal junction (TPJ), the posterior sector of the superior temporal sulcus (STS) and gyrus (STG), the ventral part of the supramarginal gyrus (SMG), and the ventral frontal cortex (VFC), including parts of middle frontal gyrus (MFG), inferior frontal gyrus (IFG), frontal operculum, and anterior insula (Corbetta et al., 2008).

Precuneus visual area which is known to be involved in visually guided reaching (Caminiti et al., 1999; Ferraina et al., 1997) is also showing a strong connection to the SC (Leichnetz, 2001; Yeterian & Pandya, 1993).

Despite all the knowledge about the SC being accumulated over the years, what is lacking today is a comprehensive map of the variety of functional connections of this structure in the human brain. Obtaining this knowledge can be very complicated considering all the obstacles on the way of studying human SC which is mainly caused by its anatomical properties. We, for the first time, have carried out a full study over the human SC functional correlates. Unlike preceding studies and instead of focusing on a single connection or limited, hypothesis-driven networks of connections, we identified the pattern of all likely sub-networks that the human SC takes part in, including the entire cortical and subcortical areas. Based on the characteristics of the SC connectivity depth profile (SCDP) we assigned each brain image voxel to a cluster in which it has the most in common with the other cluster members. Therefore, we divided the brain volume into individual clusters (SC-depth-specific functional sub-networks) that each reflect a certain type of SCDP behavior. This gives a clearer picture of how SC, as a multimodal integration unit, organizes its wide variety of interactions with the other brain functional areas. Learning about the SC functional correlates helps with making more reliable assumptions about its cognitive role and contribution to neural deficits and guides future experimental researches.

3.2 Methods

3.2.1 Participants

Resting-state data from 171 subjects (104 females, age = 30.41±2.68; 67 males age = 27.75±3.35) were chosen from the publicly available Human Connectome Project (HCP) dataset (Van Essen et al., 2012). Only those subjects whose complete set of 4 denoised and pre-processed runs of resting-state fMRI were available were chosen from the full HCP dataset. Briefly, all participants were between 22 and 35 years old, with no previously documented history of psychiatric, neurological, or medical disorders known to influence brain function. The selected group included 7 left-handed participants, 145 right-handed, and 18 bilateral-handed participants according to Edinburgh Handedness Inventory scores. Subjects' dataset comprised T1-weighted structural images and resting-state functional MR data.

3.2.2 MR data specification

Resting-state fMRI data were collected for each subject in four runs with TE=22.2ms, TR=1000ms, and opposite phase encoding directions (two anterior-posterior and two posterior-anterior). Gradient-echo EPI sequence with a multiband factor of 5 iPAT equal to 2, partial Fourier sampling ratio of 7/8, and echo spacing of 0.64 ms was used to acquire 900 volumetric images in each run with an approximate total sum of 15 minutes.

3.2.3 MRI data preprocessing

Functional images were processed using the HCP minimal preprocessing pipeline (Glasser et al., 2013), similar to the description of section 2.2.4, including head motion correction, intensity normalization, bias field correction, and transformation to an isotropic 1.6-mm MNI atlas space. To map the volumetric data onto a 59k surface, the volume data was first mapped to the native freesurfer mesh of the subject with approximately 140k vertices, which was the surface that contained the original folding details. Afterward, the mesh was down-sampled to the more sensible resolution of 59k.

3.2.4 Seed-based grayordinate-wise functional connectivity

To evaluate the functional connectivity between SC seeds and cortical and subcortical grayordinates, acquired brain signals were first demeaned and normalized separately for each run. Then, the 4D images of all 4 runs were concatenated along the time dimension. Then, we calculated the zero-order correlation coefficient (Pearson correlation) between each SC ROI concatenated signal and every brain grayordinates to determine each ROI functional connectivity map.

To control the false-positive rate and avoid significant findings originated from spurious noise correlations, a baseline of meaningful correlation values had to be defined. The CSF mask that had been previously estimated by the SPM12 segmentation module, was thresholded to accept only those voxels with a probability percent of 1. Then, we calculated correlations between SC ROIs and the average signal under the thresholded CSF mask.

Every calculated correlation value was then transformed into the z-space by using Fisher's transform function, to map the data onto the normal distribution function.

3.2.5 Statistical analysis

We calculated two-tailed one-sample t-tests for the Z-score maps. We used random permutations of the Z-score signs to estimate a null distribution of maximum t-statistics to control for the family-wise error rate (Blair & Karniski, 1993; Nichols & Holmes, 2002). The null hypothesis rejection threshold (α) was set to 0.05 after 10,000 random permutations.

We repeated the same procedure to find correlation values in which their difference from the average CSF correlation was significant. To compare the connectivity patterns between ROI subvolumes we conducted paired-sample t-tests, using the maximum t-statistic permutation method to control family-wise error rates.

3.2.6 SC connectivity depth profile

Since each anatomical layer of SC is known to have particular functional characteristics, it is expected that each layer plays a unique role in different brain functional networks. For further investigation, we created an SC correlation profile for each brain grayordinate representing its functional bond to different depths of SC. To avoid any bias caused by an ill-defined anatomical delineation of the 3 SC gray matter layers while histological information on layer boundaries are not available, we up-sampled the SC region by decreasing its voxel sizes to isotropic 0.7mm utilizing spline interpolation. Then, we divided SC into voxel-wide surfaces parallel to the tectal plate. The outcome was 12 parallel surfaces of width 0.7mm on both right and left SC. Finally, for every brain grayordinates, a depth profile of a total number of 24 correlation values was created. Share of each colliculus was 12 values ordered by the distance of the surface to the tectal plate; starting first with the correlation to the nearest layer to the tectal plate.
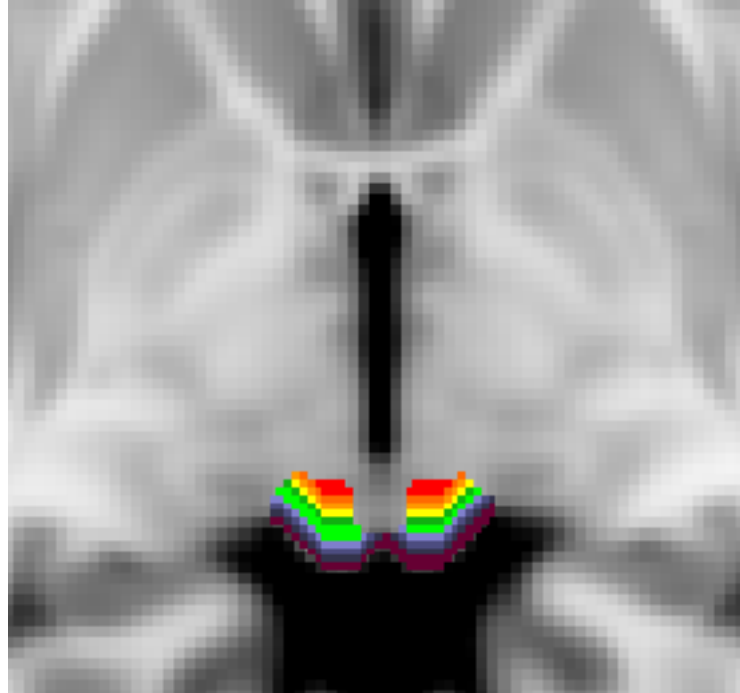
Figure 3.1 - 12 parallel SC layers of width 0.7mm on each hemisphere, used to create SC connectivity depth profile for each brain vertex

3.2.6.1 Depth effect

Using ranova function (MATLAB release R2018b), we calculated repeated measures ANOVA for each grayordinate SCDP across subjects to detect any non-constant pattern. The repeated measures ANOVA reveals grayordinates with a significant depth effect in their left or right SCDP

$$Repeated\ Measures\ ANOVA: \quad F = \frac{MS_{conditions}}{MS_{error}}$$

P-values were corrected for family-wise error with Bonferroni criteria. The result showing the grayordinates with significant depth effect is displayed in F-value mapped over a standard surface.

3.2.7 SCDP functional networks

3.2.7.1 SCDP clustering

We explored brain grayordinates to cluster the ones with similar SCDP pattern. We preferred the quantitative clustering approach over descriptive methods since the immense number of grayordinates makes it impossible to manually classify all SCDPs or detect the prevalent SCDP patterns. Thus, we implemented the k-means clustering algorithm to detect

and cluster grayordinates which were the most similar in sense of their connectivity to the different layers of their ipsilateral and contralateral SC. K-means is an unsupervised learning approach that tries to minimize the summation of euclidean distances between the data points and the cluster mean to which they belong (Hartigan & Wong, 1979). The euclidean distance is being defined in an N-dimensional feature space that is being used for the clustering purpose.

In the current study, we selected the SCDP and its gradient as discriminants providing information for the learning algorithm. To build the feature vector for each grayordinate we combined the previously calculated vectors of 24 correlation values (12 for each SC) with their gradients (11 for each SC). The average of these 46 values (feature vector) across subjects was used in a K-means machine to learn the most common SCDP patterns among the studied grayordinates. These feature vectors were also normalized to avoid any bias towards a particular feature. We decided to include the gradient values to emphasize depth-dependent changes in correlations.

We excluded cerebellum grayordinates before running the clustering over the dataset since the descriptive data showed that the histogram of the SC-cerebrum correlations has a different median and shape compared to the histograms of the SC correlation with the cortex and the midbrain. The fact that the k-means result would be affected by the correlation magnitudes due to the nature of the chosen features suggests that any magnitude bias might impose a change in the final structure of the clustering outcome.

The initial number of clusters on each hemisphere was specified based on the clustering dispersion and the clustering error probability. Clustering dispersion is the summation of the euclidean distances between each grayordinate feature vector and the mean feature vector of the cluster that the grayordinate belongs to. In case of having the discriminative features properly chosen the dispersion value would constantly decrease by increasing the number of clusters (k) until it converges to zero as k becomes equal to the number of data points. On the other hand, the clustering error probability keeps decreasing when the number of clusters decreases. As described, each measure alone suggests choosing a k value at one or the other end of the possible range of values; however, this contradictory behavior provides a rather descriptive hint to choose an optimal value for the k.

To better estimate the optimal k value, we randomly divided the dataset into five groups of 33 subjects and ran the clustering for each group, on by one. Clustering error probability measures the chance of a single grayordinate not falling into the same cluster in all five repetitions. We calculated these two measures for each k between 1 to 20 and ran the clustering for the grayordinates on the left and the right hemispheres, independetly.

After choosing the optimal number of clusters, k-means was conducted over the entire dataset average feature vectors. Since the clustering is done for each hemisphere independently and the resulting labels are not concordant, we used the Dice coefficient to find the most similar clusters on the left hemisphere to each cluster on the right side and then assigned each pair a same label.

3.2.7.2 Clustering reproducibility

To evaluate the reproducibility of the clustering results, we randomly selected 60 subjects out of 170 and reapeated that thousand times. Then we carried out clustering for every 1,000 samples with the chosen optimal number of clusters for each hemisphere. At the end of each run, the resulting clustering labels were matched to the original labeling. Eventually, we calculated the clustering reproducibility probability for each grayordinate by counting the number of times that a grayordinate fell into the original cluster.

We evaluated the contribution of the features to form the clustering outcome by conducting the same clustering procedure for the entire dataset by limiting the features once to the correlation values and then to the correlation vectors gradient. The comparison between the resulting clusters helps to understand whether the clustering uses the information from both the correlation and the gradient values to calculate the clusters or it is relying upon only one of these two vectors; Knowing that has a fundamental effect on the interpretation of the estimated sub-networks.

As the dataset under study is acquired in the resting-state, the SC functional sub-networks would share characteristics with the underlying global functional networks at the resting-state. Similarly, the outcome of data-driven analysis of any geometrically alike ROIs might be quite similar to the geometry of the well-known resting-state networks. To address the concern of the SC sub-network genuineness, we preserved the geometrical shape of the original ROIs and placed them symmetrically within the thalamic area, and performed the clustering for the newly calculated depth profiles. Any noticeable change in the clustering result for the new ROIs is a prove of the association between the ROIs'

location and the resulting clusters.

3.3 Results

3.3.1 Functional Connectivity Networks

We performed seed-based grayordinate-wise functional connectivity analyses for 3 ROIs depicting 3 anatomical zones of SC for both the right and the left hemispheres. This resulted in 6 whole-brain connectivity maps. The resulting maps represent the functional networks in which each SC anatomical layer takes part in. The voxel size of the images used in this study is 1.6mm isotropic where the approximate width of the first two layers of the SC is 1 mm each. As a result, the content of the mid-layer would be the weighted summation of the three actual anatomical layers of the SC. Thus, instead of using the term intermediate layer, we would refer to the middle ROI as the transition layer. Indeed, the signals within the first and the third layers are not purely coming from the superficial and the deep layers and each has a share of the information within the intermediate SC. Consequently, the apparent resemblance between the transition layer connectivity map and the two other layers map was very much expected. The important question here is, how much of the information within each layer is being smeared out with the adjacent layers signals. Looking at the results of the paired t-test between ipsilateral layers connectivity maps show the areas in which the functional connectivity effect is more pronounced for one layer comparing to another (Figure 3.2). Our results show that the more superficial the layer is the stronger effect it has, in a way that no layer shows a stronger effect than its higher layers in any brain region. The interpretation of this finding is not necessarily that we do not have any unique information in deeper layers. It seems by traveling to deeper layers, the functional correlations get smaller. This can happen because of the reduced SNR as the density of the cell bodies decreases by depth. Thereby it might not only be the quality of the data that results in lower correlation values to the depth of SC, but also the intrinsic characteristics of the region with less dense neuronal endings which result in less pronounced effect size.
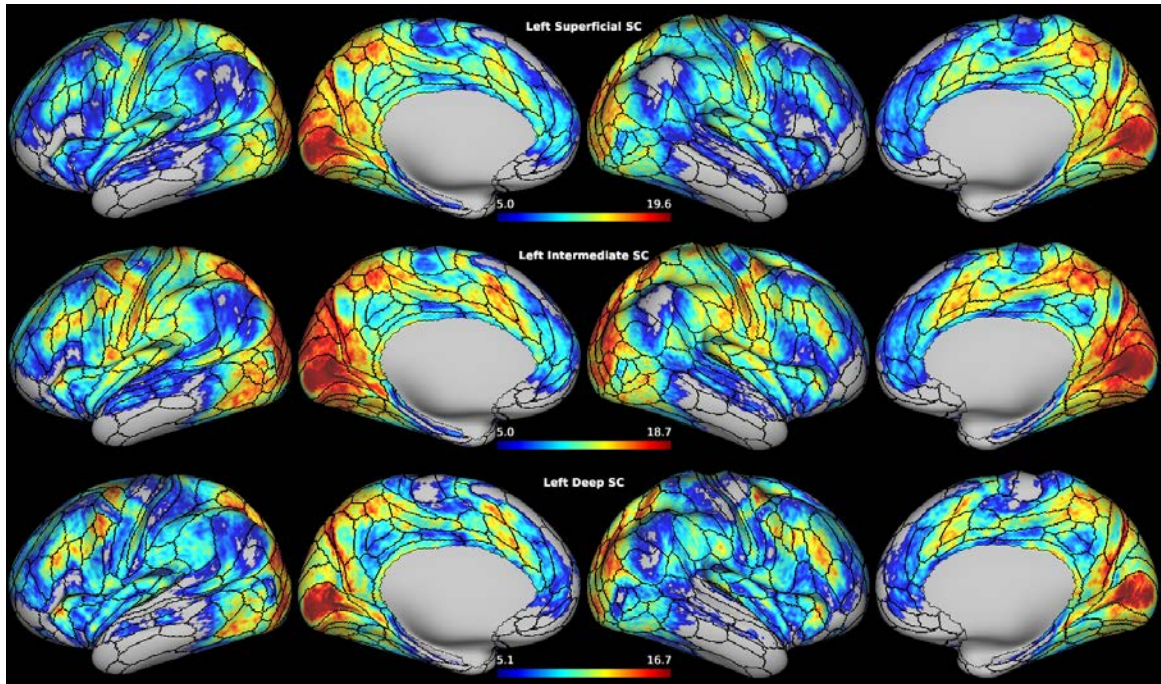
Figure 3.2 - 3 left SC layers ROI cortical correlation z-score paired-sample t-test for testing the connectivity values against the distribution of each subject's average SC-CSF connectivity z-scores.

3.3.2 Depth effect

The analogy between the functional connectivity maps of different layers raised the question of whether the FCN of SC layers is carrying unique information, and if yes, does a set of correlation values from SC layers to a single grayordinate tells us about the functional characteristics of that neural unit.

To trace the depth-dependent correlation changes for each grayordinate, we spatially up-sampled the original functional data at the SC location by decreasing the voxel size to isotropic 0.7mm using a spline interpolation. We have chosen 0.7 mm since the simultaneously acquired anatomical scans had an isotropic resolution of 0.7 mm. One essential assumption is that the transition between new SC layers is rather smooth without any unpredictable changes in the signal behavior. This must hold since every new layer is still representing one layer or the combination of the 3 anatomical layers of SC.

After calculating the functional connectivity for all 12 layers for each SC, we calculated repeated-measures ANOVAs for each grayordinate, separately for the left and the right SCDP to figure out whether a significant depth-dependent correlation effect exists at the grayordinate level. Corrected for FWE, we created an F-map for each SC that shows grayordinates with significant fluctuations in their SCDP (Fig. 3.3). We observed significant variations of vertex-wise correlations with 12 SC ROIs across occipital, parietal, temporal, and frontal cortex. Significant effects were absent in the middle and anterior

temporal lobe, the inferior and dorsal frontal cortex, and the lateral inferior parietal cortex.

The areas with a significant depth effect are pretty identical to the areas which have a significant correlation with at least one of the SC layers from the FC maps (shown in
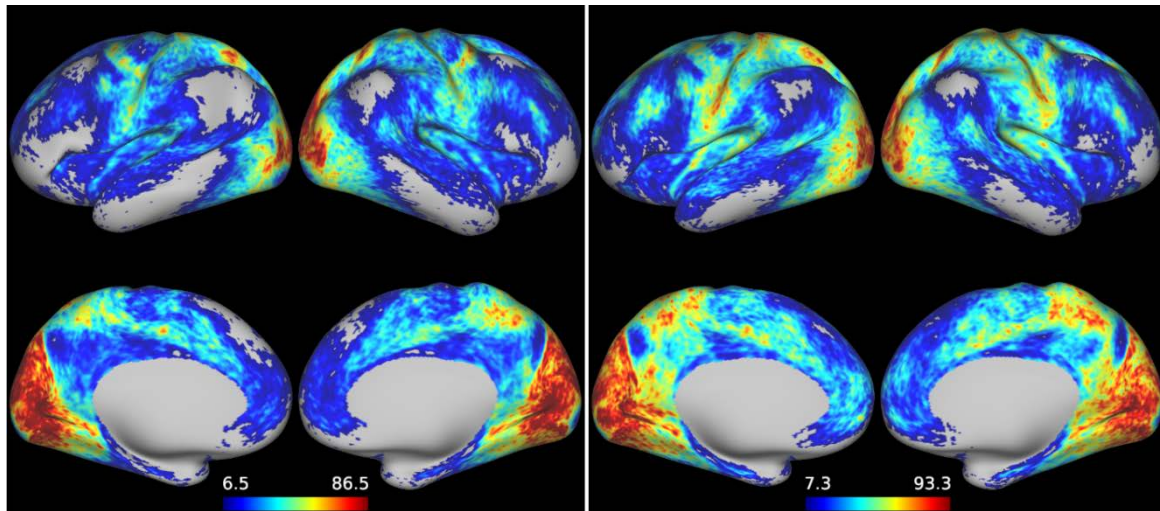

Figure 3.3 - F-maps corrected for family-wise error (α<0.05) showing significant depth-dependent correlation effects, both for the left SC (left) and the right SC (right)

Figure 3.2). For the left SC 96.3% of all grayordinates were also significant in the FC maps (see section 3.3.1 and Figure 3.2), i.e. showed a positive correlation significantly above CSF baseline correlations. This means 3.7% of all grayordinates showed a significant variation in correlation values with ROIs in different depths of the SC, but did not have a significant correlation above the CSF baseline and the FC analysis. On the other hand and on the right SC, 92% of all grayordinates were also significant in the FC maps; while, the ratio of the grayordinates with a significant correlation to at least one of the SC layers, and a significant depth effect was 0.95 for the left SC and 0.986, for the right SC.

3.3.3 SCDP Clustering

To further investigate the influence of the SCDP pattern of each grayordinate and search for cortical areas of similar SCDP patterns we used k-means clustering of grayordinate-wise SCDPs.

A general, gradual correlation reduction with increasing depth was the most prominent characteristic among the majority of the grayordinates' SCDPs. First inspections showed that variation of the rate of this general, gradual decrease of correlation coefficients provides important distinctive information. Therefore, we added SCDP gradients to each profile to create the feature vectors required to learn the properties of the clusters by k-means algorithm. To make the selection of a proper value for the number of clusters 'k' more objective, we repeated the clustering of the grayordinates for each hemisphere 20

times, changing the k value from 1 to 20 and calculating the clustering dispersion (Fig. 3.4) and the clustering error probability (Fig. 3.5). We chose k=6 as a number of clusters to be calculated on each hemisphere since it is on the mid way to the location of the elbow of the clustering dispersion plot (k=4) and the location of the lowest accumulative clustering error. The reason that we selected the same number of clusters for both hemispheres is that there is no evidence supporting the existence of any functional lateralization of either SC. By initializing our k-means algorithm we avoid inducing artificial lateralization into the final result.
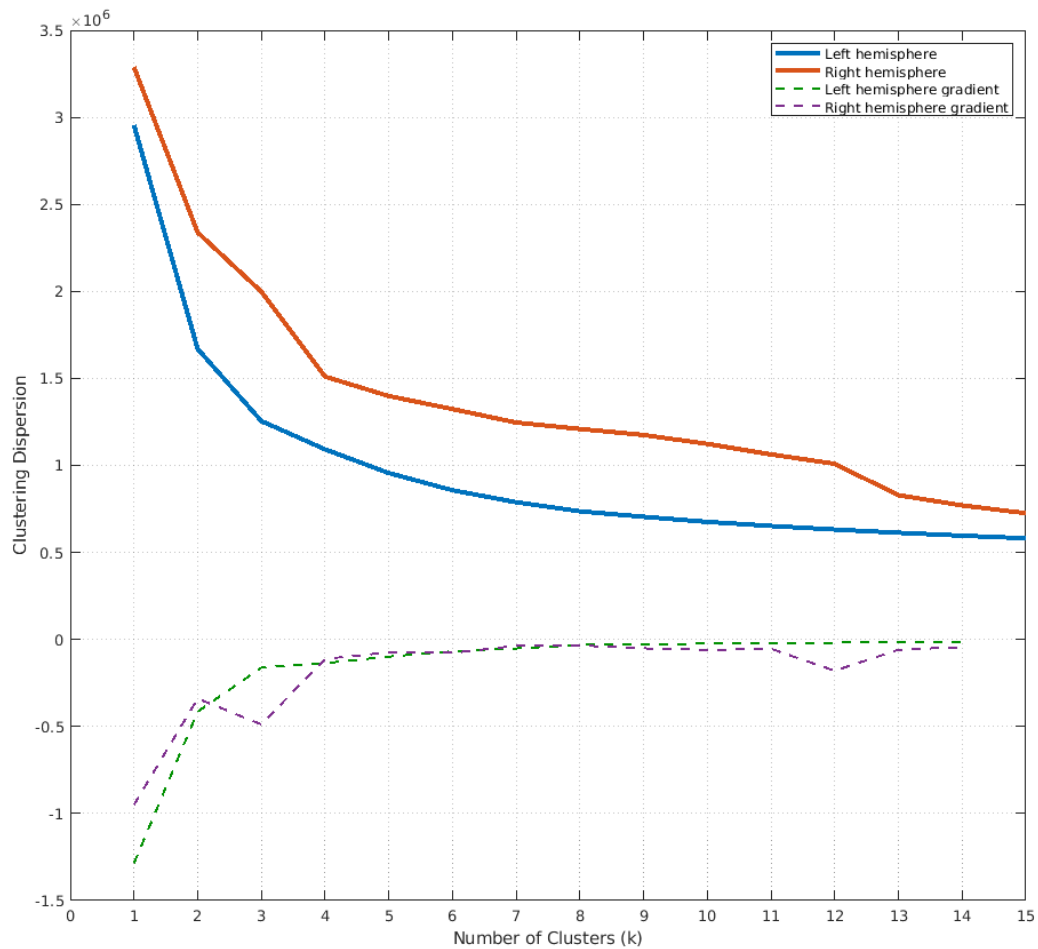

Figure 3.4 - Cluster dispersion plot shows how the mean distance from the cluster centroids decreases by increasing the value of k. for the left and the right hemispheres the elbow locations are at (k=3) and (k=4), respectively. This means that k values below those numbers are not recommended.
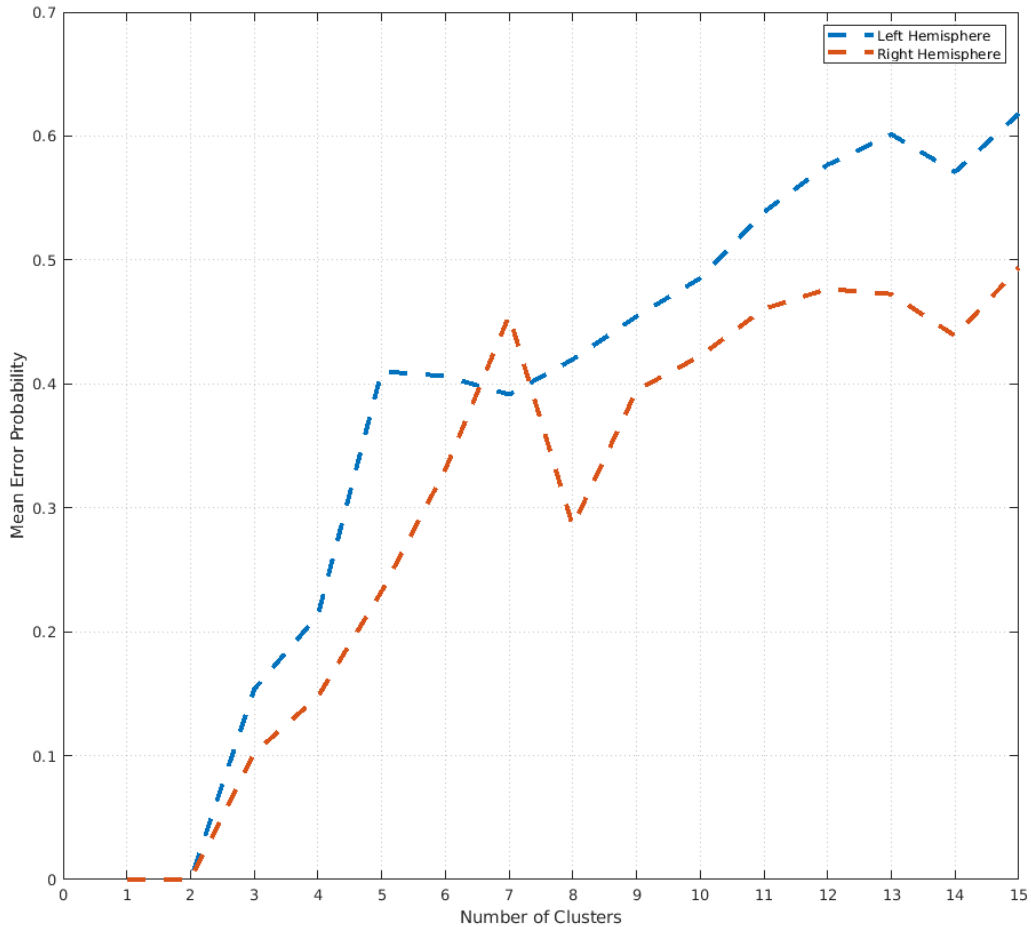
Figure 3.5 - The Mean error probability plot reveals the probability of inconsistent clustering increases by increasing the value of k. k=6 seems to be a suitable value to be far enough from the elbow values of the last figure and low enough to have proper mean error probability on both hemispheres.

By selecting the initial number of clusters, we ran k-means clustering on the entire dataset to identify the main functional networks on each hemisphere based on the updated connectivity profiles. To make the labels concordant between the two hemispheres we made use of the dice coefficient to find the pairs of contralateral clusters which share the largest number of grayordinates. In the following we describe the functional clusters identified by these procedures (Fig. 3.6), we refer to the Glasser multimodal parcellation (Glasser et al., 2016) in the labeling of cortical areas:

Cluster #1: This cluster completely overlapped with areas with no significant FC and/or depth effects in the preceding analyses. It mainly comprises areas from the lateral temporal gyrus, including the temporal polar cortex, inferior temporal gyrus, inferior temporal sulcus, and the middle temporal gyrus, excluding PHT. Furthermore, patches of the left frontal cortex belonging to areas 44 and 45 represented one of the few asymmetrical patterns from our clustering outcome. Patches of grayordinates on the right anterior

superior temporal gyrus were also appended to this cluster. Orbitofrontal cortex (OFC and pOFC), along with areas 25, s32, and 10v, representing the tip of the anterior cingulate cortex and also lateral and anterior parts of area 47 and a stripe on the dorsolateral prefrontal cortex (DLPFC) including SFL and 8BL were parts of cluster 1. In the subcortical volume, the posterior head of the caudate nucleus and lower section of the globus pallidus, as well as the entire amygdala, were the prominent nuclei included in this cluster.

Cluster#2: This cluster was composed of the lateral and medial parts of the secondary visual cortex, ventrolateral intraparietal cortex (LIPv), FEF, left PEF, the supposed trunk representation in areas 1 and 2, and the upper limb representation of areas 3a and 3b of the primary somatosensory cortex. It included parts of the posterior cingulate area together with parietal areas 5mv and 7Am, the medial section of the hippocampal area, right substantia nigra, and LGN.

Cluster#3: This is one of the largest clusters in terms of the surface area and, like cluster#1 it mainly comprised areas that had no or marginally significant FC or depth effects. It covered auditory association areas including A4, A5, TA2, and the superior temporal sulcus on both hemispheres, except for the anterior parts on the right side. This cluster also overlapped with the medial parts of the inferior parietal areas including anterior parts of PGs and PGi, PFm and posterior PF, large portions of the DLPFC (8C, 8Av, i6-8, s6-8, 9p, 9a, 8Ad, p9-46v, a9-46v, posterior 46, and anterior 9-46d), supplementary motor areas 6ma and 6mp, premotor areas 6v, 6r, 6a and 6d, frontal opercular areas FOP2 and FOP3, posterior, middle and anterior ventral Insular (PoI1, PoI2, MI and AVI), areas 10r, 10d, a10p and p10p, area 24dd, Peri-Sylvian Language area (PSL), area 55b and finally upper and lower limb areas of the primary motor cortex and the upper limb area of the primary somatosensory cortex 3a. The upper part of the Globus Pallidus, as well as Putamen, is part of the subcortical portion of this cluster. It comprises the entire area of the upper putamen and ends up in the middle section of the lower putamen.
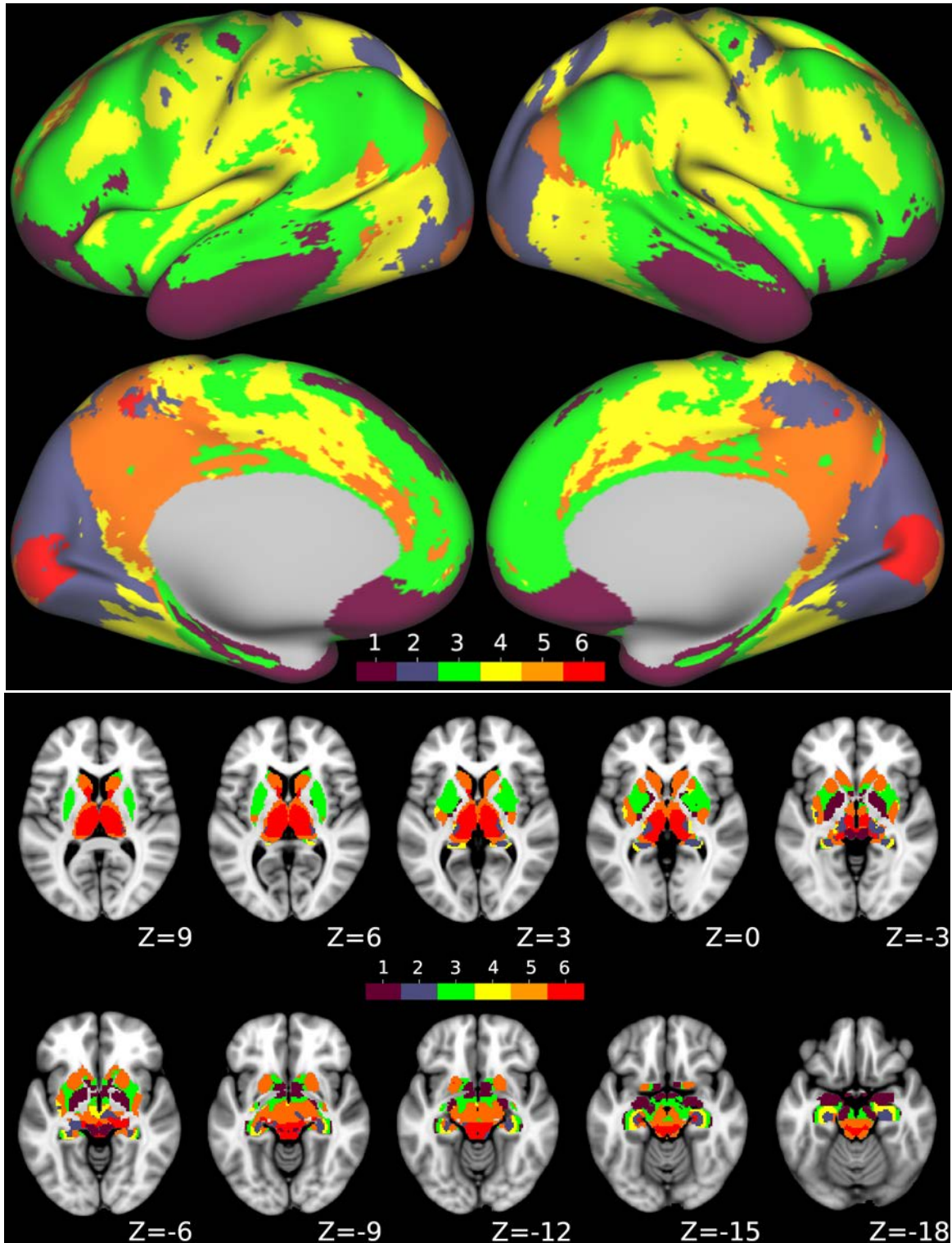
Figure 3.6 - Clustering divides the brain (Cortex on top, sub-cortex below) into 6 areas separately on the right and the left hemispheres

Cluster#4: is yet another extensive cluster that unlike cluster 3 was located in areas with significant FC and depth effect. The entire TPOJ2-3 and the superior temporal visual area (STV) were part of this cluster. The MT+ complex (MT, MST, FST, and V4t) was divided between clusters 2, posteriorly, and cluster 4 anteriorly. Ventral stream visual cortex was

another complex being divided between clusters 2 and 4 where cluster 4 included the larger portion of the Fusiform Face Complex (FFC), Ventral Visual Complex (VVC) and the Ventromedial Visual areas 2 and 3 (VMV2-3), while V8, PIT complex and VMV1 were located mostly in cluster 2. Cluster 4 also comprised areas from the medial bank of the intraparietal sulcus (MIP, LIPd, and AIP), as well as IP1 on the lateral bank of the intraparietal sulcus and partially IPS1. Areas 5L and 5m together with the cingulate motor area 24dv and area 7PC and PFt complex were further parts of cluster 4. The primary somatosensory cortex belonged almost entirely to cluster 4, excluding the presumed trunk representation and presumably neck and shoulder representations for most of area 3a, 3b, and partially for area 2. The upper limb area, however, was not part of the area 3a, and the primary motor cortex contribution to cluster 4. The lower limb and parts of the trunk representation of the primary motor cortex were also not part of this cluster. Besides, the entire posterior opercular cortex (43, FOP1, OP4, OP1, OP2-3, and PFcm) and parts of the early auditory cortex, including the A1 lateral belt (L-Belt) and the retro-Insular cortex (RI) are parts of cluster#4. We also found patches in Anterior Cingulate and Medial Prefrontal Cortex, as well as Supplementary and Cingulate Eye Field (SCEF). The premotor and frontal eye fields as well as area 6a also shared some areas with cluster 4. This cluster also covered large portions of the lateral and anterior parts of the hippocampus. The last and possibly one of the most interesting parts of this cluster was located in the middle section of the posterior and anterior parts of the inferior frontal sulcus and inferior frontal junction together with areas 8C and p9-46v, covering an area ranging from the inferior frontal gyrus to middle frontal gyrus. This cluster had no significant subcortical components.
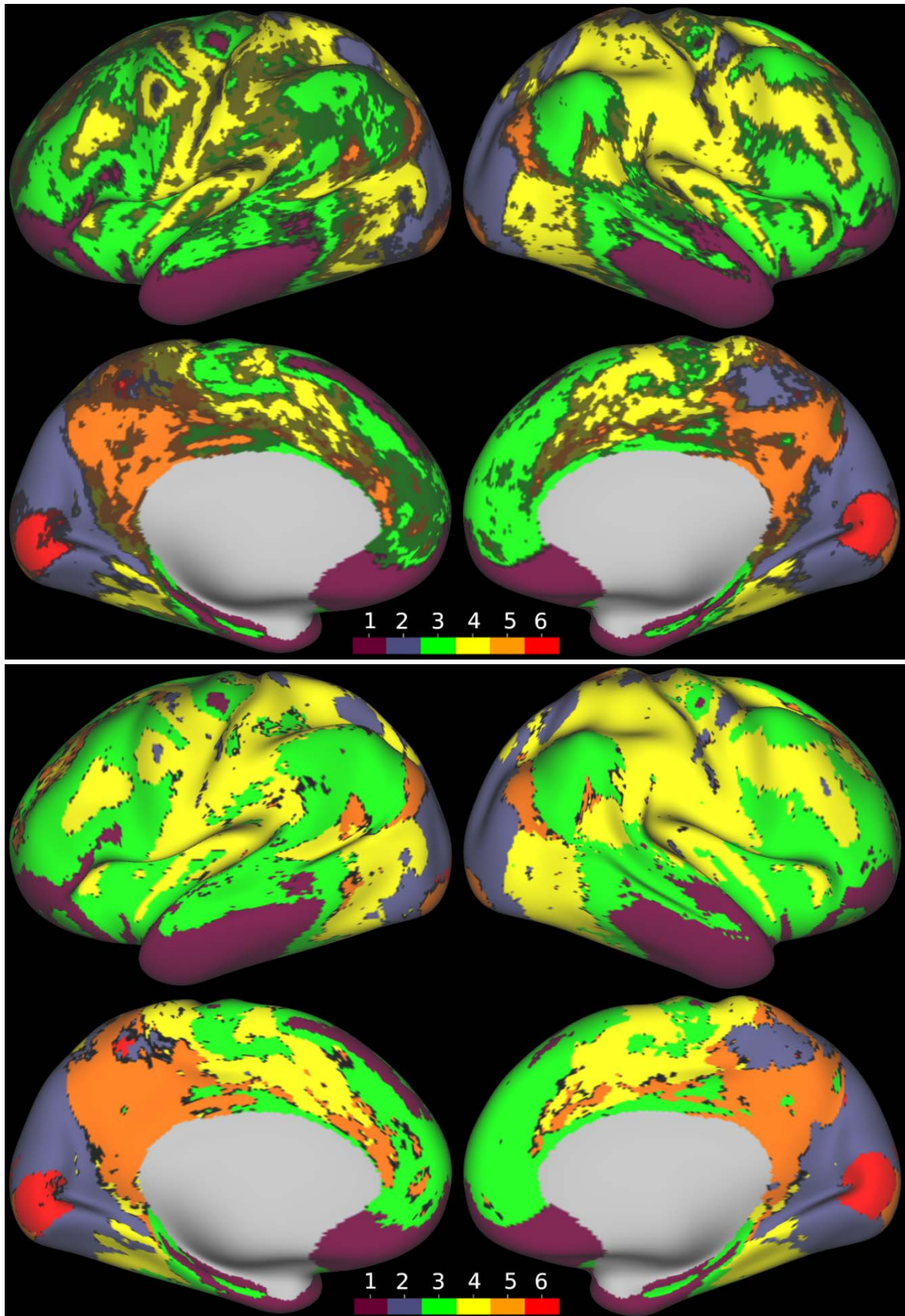
Figure 3.7 - Thresholded probability maps overlayed on top of the clustering result map. Shaded areas show locations where the chance of reproducing the clustering result was less than 85% (top) or 50% (bottom).

Cluster#5: The most noticeable area assigned to this cluster is the foveal part of the primary and the secondary visual cortex. Cluster 5 also included a major part of the posterior cingulate cortex, except for the dorsal visual transitional cortex and the prostriate cortex, and the posterior cingulate visual area. Parietal-occipital sulcus and the medial part of area 7 were included in this cluster. Scattered parcels were located in the anterior cingulate cortex, superior frontal gyrus, and the posterior part of areas PGs and PGi which together with the posterior cingulate areas are forming the default mode network. The trunk representation of area 3b was also a fragment of this cluster. There was a comparably large and complex network of subcortical volumes appended to cluster 5. This included a sizable portion of the caudate nuclei, mostly toward their head sections. Anterior and posterior part of the lower putamen, anterior thalamus, and ventral parts of the mid-brain, including left substantia nigra and the red nuclei.

Cluster#6: This last cluster was mainly made up of the primary visual cortex extending from the parafoveal visual area to the peripheral visual cortex. There were also blobs in the adjacency of the foveal part of V2 and V3 and the posterior cingulate visual areas which were more accentuated on the left hemisphere. This cluster also had major subcortical components. These included reticular formation, the inferior colliculus, and the entire thalamus except for its anterior parts and dorsal and lateral sections of the inferior thalamic areas.
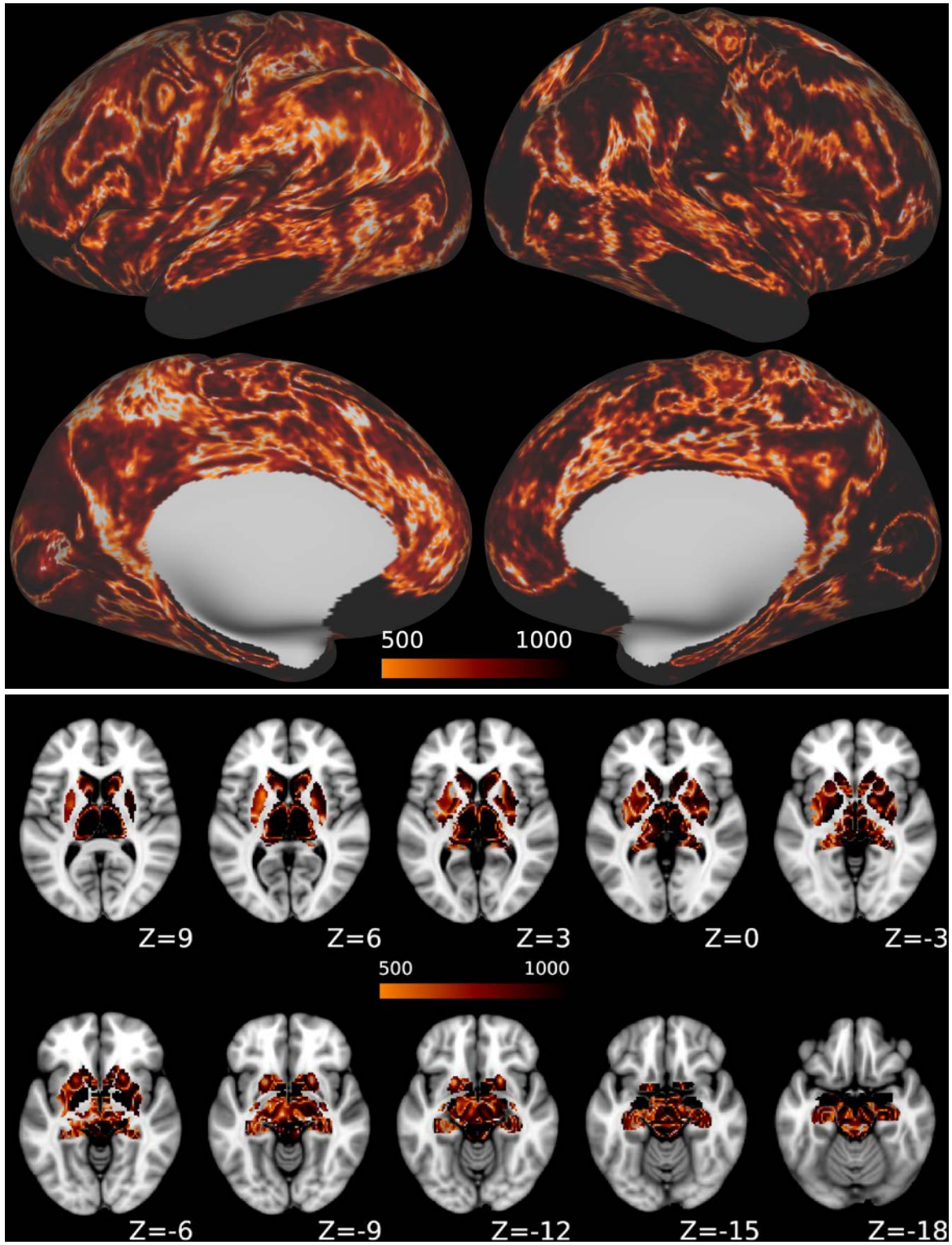
Figure 3.8 - Entropy map which shows the chance of clustering result replication for each grayordinate running the k-means clustering after random selection of subsets of 60 subjects for 1000 times and matching the resulting cluster numbers to the original full set clustering result (shown in Fig. 3.6).

3.3.4 Characteristics of identified clusters

The clustering was run over the normalized extended feature vectors of each grayordinate. K-means clustering tries to gather the most similar grayordinates regarding their SCDP. This implies that K-means maximizes the distance between the clusters' mean feature vectors or so-called centroids based on a cost function, which in this case is the euclidean distance. Therefore, looking at the centroids vector reveals how the algorithm has formed the clusters and how much different each cluster is from the others. However, the normalized vectors do not tell us about the true origin of the differences. To understand the cluster members' profiles we need to look at their non-normalized centroid vector. (Figure 3.8) shows the original clusters' centroid vectors. Due to the different value ranges of correlation coefficients and their gradients, each set of values is shown in a separate panel although both groups of values belonged to the same centroid vector. For both panels, the first twelve correlation values, respectively first eleven gradient values refer to the ipsilateral SC, the following values refer to the contralateral SC. As such, the left plots belong to the left hemisphere clusters and the plots on the right side show the centroids vector for the right hemisphere clusters. The correlation vectors are shown at the plots on the top row and the gradient vectors are on the second row.
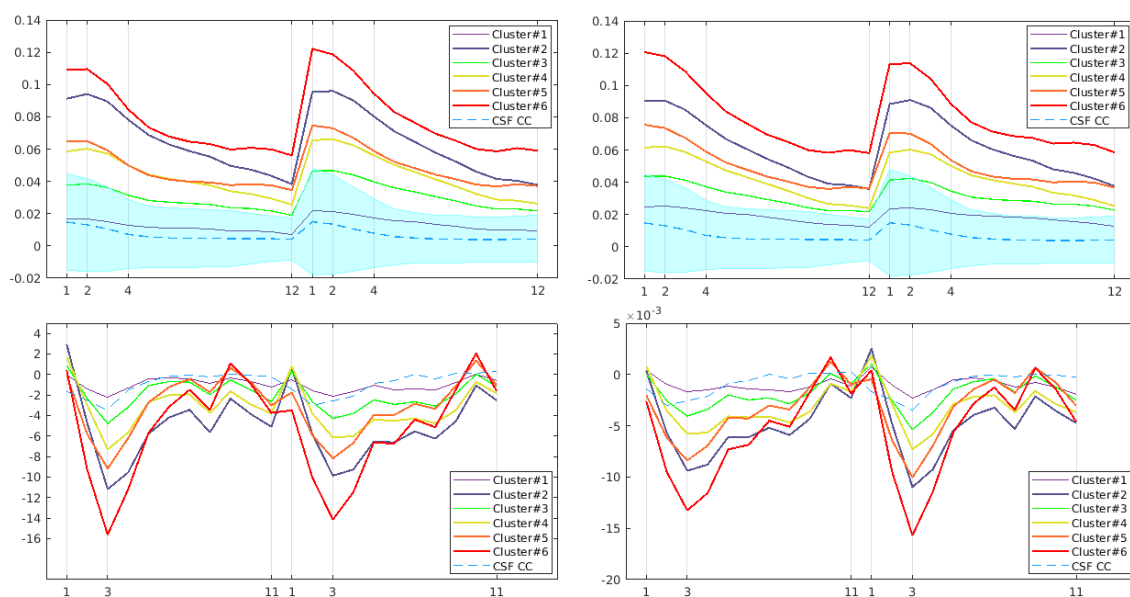
Figure 3.9 - Cluster profile plots showing the mean grayordinate (centroid) correlation depth profile (top) and the gradient of the depth profile (bottom) for the left SC (left panels) and the right SC (right panels). In each plot in the top row, the first 12 values are the centroids correlation with twelve ipsilateral SC ROIs and the second 12 values are the centroids correlation with twelve contralateral SC ROIs. The bottom plots can be interpreted in a similar way.

The SCDPs of corresponding clusters in the ipsilateral and contralateral hemispheres were pretty similar. At the first glance, SCDPs from different clusters also

resembled each other with the magnitude of the correlation values across different depths being the main difference. The highest correlation always occurred in the superficial ROIs and then it declined with increasing depth. The gradient profiles added substantial information to these correlation profiles, showing that the steepness of correlation values decreases with depth varied considerably between clusters.

Cluster 1 stood out among the other clusters because of the lowest correlation values at each depth and a rather flat correlation vector with a gradient vector close to zero. Comparing cluster 1 SCDP to the mean CSF SCDP revealed that this profile originated from the fact that this cluster had no significant correlation with any of the SC depth ROIs. Cluster 2 showed a relatively high correlation with SC and one of the most dramatic changes in gradient and the second most negative local minima, i.e. a relatively sharp decrease of correlation values with increasing depth. This cluster together with clusters 3 and 4 showed an increase from the first to the second SC depth on both ipsilateral and contralateral sides. Cluster 3, pretty similar to cluster 1, had a very low correlation to the SC with not much of an alteration across layers. This pattern once again is pretty much comparable to the CSF SCDP behavior, just barely exceeding CSF correlation values. The correlation vectors of clusters 4 and 5 were very similar in their values, while they had different gradient characteristics. Cluster 4 maintained the same negative correlation reduction rate, thus it fell continuously with the SC depth. Cluster 5 gradient, however, got close to zero from the intermediate to the deeper ROIs, i.e. the correlation values in the intermediate and deep ROIs were similar. Finally, cluster 6, which was located at the parafoveal primary visual cortex and in the thalamic nuclei, had the highest correlation values among all clusters, while exhibiting the highest reduction rate and also the fastest gradient recovery.

3.3.5 Features Contribution

The observed distinction between the clusters, looking at their correlation levels in (Figure 3.9) raised this question, whether it id possible to obtain the same clustering results after exclusion of the gradient features. The clustering outcome would then mostly reflect the general magnitude of correlations between the whole SC and other areas and structures with little if any influence of depth-dependent effects on the clustering outcome.
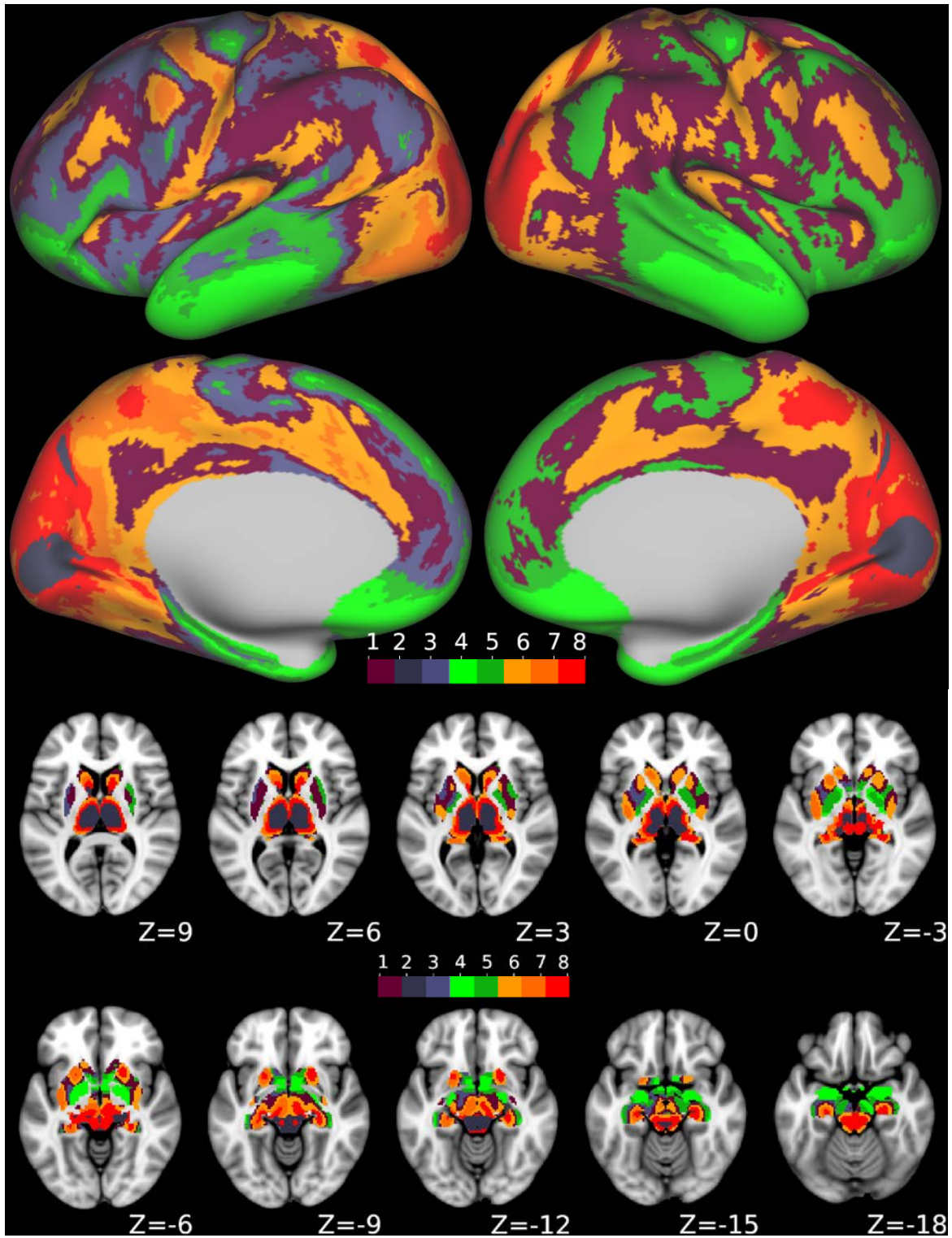
Figure 3.10 - Maps above show the clustering result when using the correlation depth-profile only (without its gradient). The same procedure suggests (k=8) on each hemisphere.

(Figures 3.10 and 3.11) show how the changes in the reduction rate play an important role in forming the clusters. While the general reduction pattern might be associated with the underlying anatomy, the gray matter density, the ratio of connections

to different sub-networks, or even an inhomogeneous signal acquisition, the differences between the clustering results with and without the gradient features confirm that it matters how this reduction rate behaves.
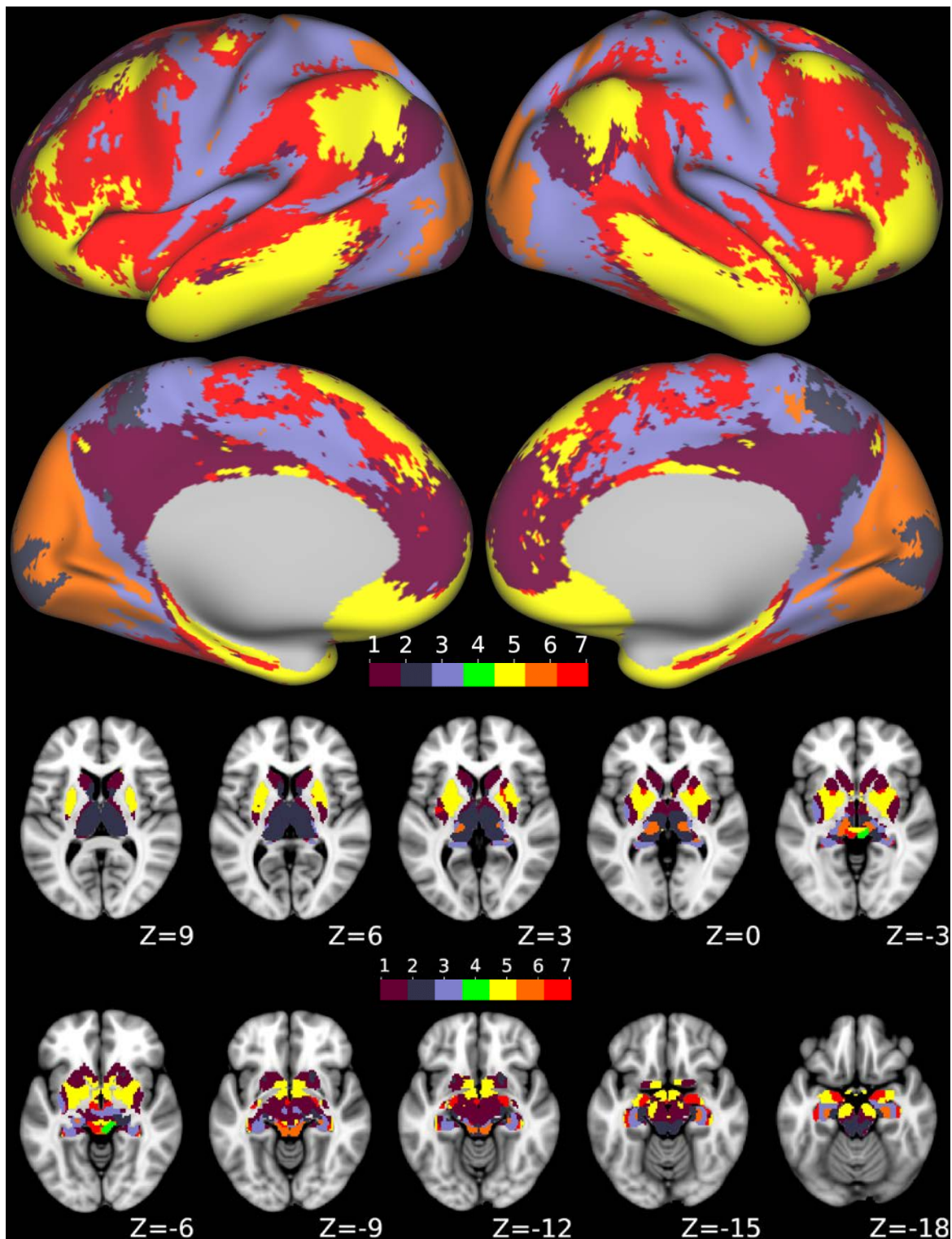

Figure 3.11 - Maps above show the clustering result when using the correlation depth-profile gradient only (without correlation depth profile). The same procedure suggests (k=7) on each hemisphere.

3.3.6 Specificity of SC depth-related clustering

Using thalamic ROIs (Figure 3.12) instead of anatomically informed SC depth ROIs resulted in a dramatic change of the previously reported clusters. (Figure 3.13) shows the shape of the thalamic clusters where all the clustering analysis parameters were kept the same as in the original run with SC depth ROIs.
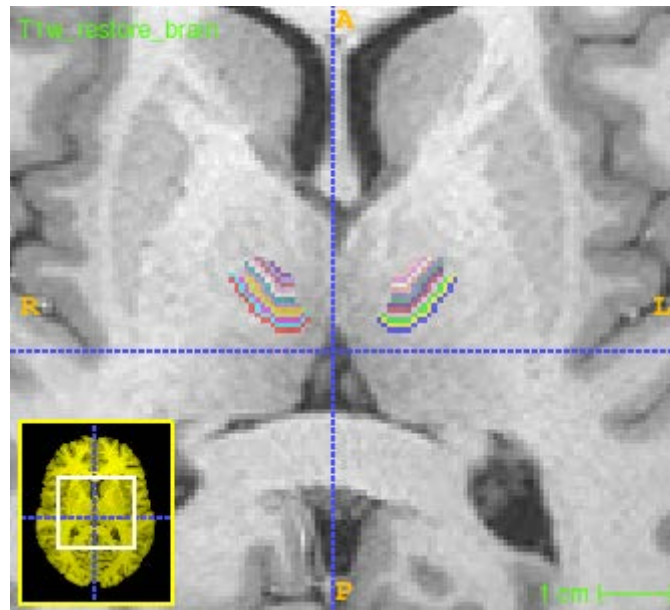
Figure 3.12 – Thalamic ROIs

The similarity between the maps for the clustering result using the thalamus and SC ROIs is striking at the first glance. the parafoveal area delineation, the ventral attention area on the medial surface, and the cluster including somatomotor areas all share similarities with clusters 6 and 4. Nevertheless, the segmentation of the primary visual area on thalamus clustering could be expected. Despite the similarities between the Null-correlation clusters of the SC sub-networks map (1 and 3) and the clusters including similar areas on the thalamus sub-networks map (red and green), we observe a large overlap of those thalamus map clusters with clusters of significant correlation in the SC map. Such inconsistencies in the organization of the anatomical areas into the sub-networks in two maps refute the possibility of replicability of the clusters.

The physiologically plausible structure of the thalamus clustering map and the analogy between the SC and thalamus clustering results do not come as surprise. The semi-random placement of the SC ROIs within the thalamus results in the superposition of signals from adjacent thalamic areas. Therefore, the resulting ROI signals are quite structured and likely to show a significant correlation with various brain functional areas.

A realistic expectation from the clustering algorithm is to reorganize the resting-state networks and functional sub-units in a way that it expresses the distinction of the functional roles of the ROIs. The unique details in the way that the clusters are organized in each case reflect the functional capacity of the ROI that the clustering result is directed by. The coverage of the peripheral vision areas and the oculomotor system in cluster 2 of the SC clustering and the salient delineation of the inferior frontal gyrus/sulcus and the STV in cluster 4 are examples of such distinctive details.

Figure 3.13 - Maps above shows the clustering results for the relocate ROIs in thalamus.
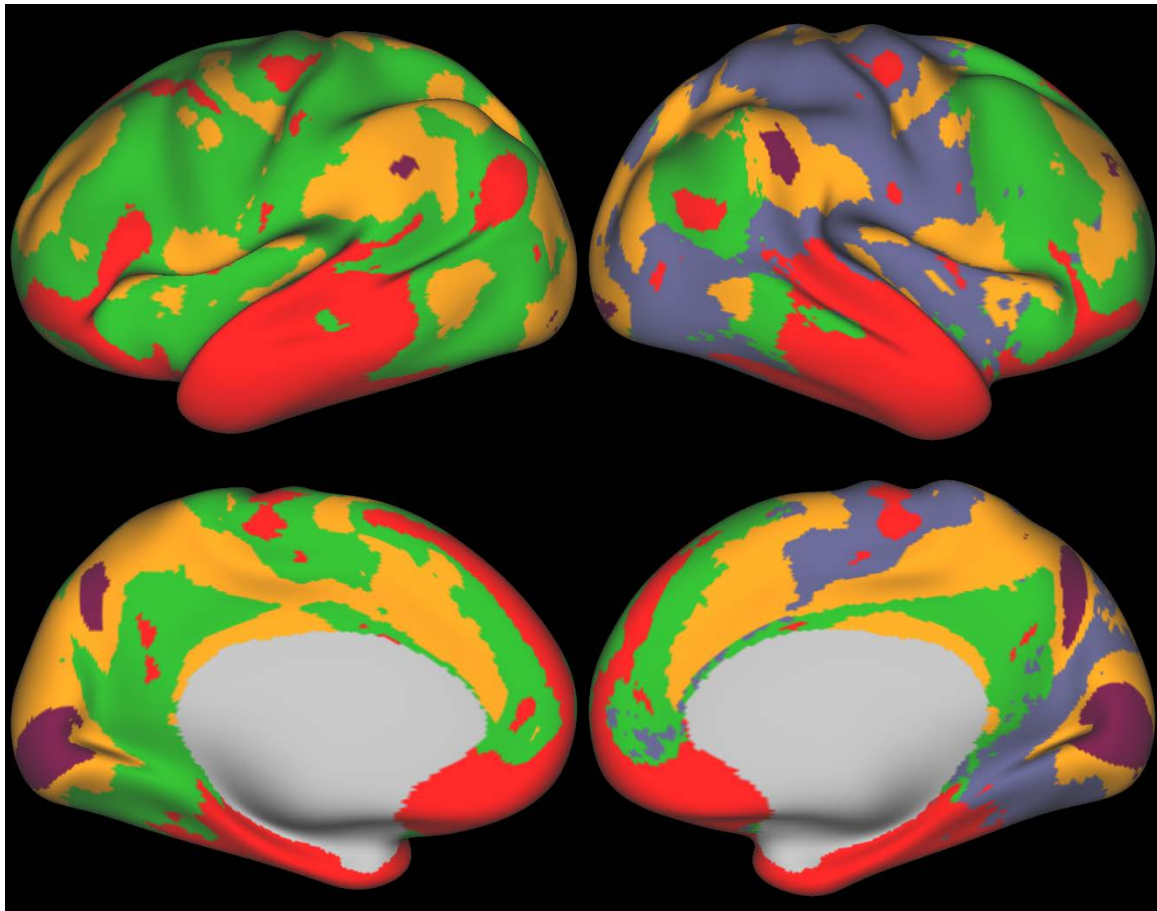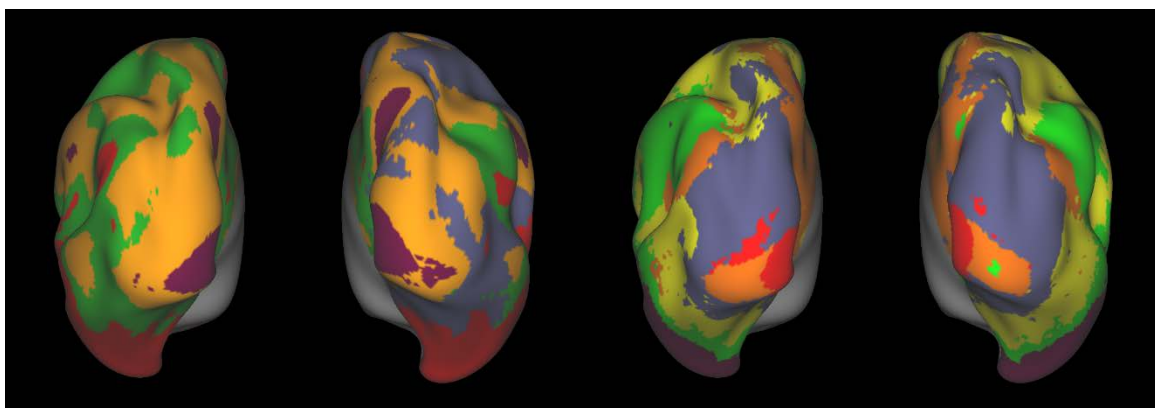

Figure 3.14 – Comparison between the clusters for the ROIs in thalamus (left) and the ROIs in SC (right) from the posterior view.

3.4 Discussion

3.4.1 Functional connectivity

The FCN from 7T data resembled very much the results that we previously obtained from the 3T data. In the previous chapter, we illustrated the complete cortical, subcortical, and cerebellar functional connectivity network of the human SC. The higher number of subjects and more importantly, higher SNR of the 7T images increased the analysis sensitivity to the degree that the slightest pattern, even those from the undesirable structured noises are being captured to some extent. We used the correlation between SC and the CSF as a baseline estimate to eliminate the effects of the unstructured noises. However, conventional statistical inference is not sufficient to discriminate between the true-positive results and false alarms because of spurious noise correlations when we are dealing with such a large dataset and a weak signal from a minuscule structure. As a consequence, any deduction from the current outcome must be partially based on scientific judgment.

Looking at the functional connectivity maps indicated that correlation values per se did not reflect the underlying functional properties of the SC layers, however, slight differences in their general FCN patterns were evident. This means although the correlation values are descending with depth, the reduction rate was not the same in all areas. In other words, the level of deep SC contribution to some functional networks was preserved while its presence in other networks faded.

3.4.2 SC functional brain networks

Cluster 1 together with cluster 3 included major areas of the inferior, medial and lateral temporal cortex, auditory association cortex/ superior temporal areas, insular cortex, inferior parietal cortex, Brodmann areas 2, and 3a upper limb as well as area 4 upper limb w.o. hand and lower limb, premotor cortex, paracentral lobule, anterior and midcingulate, medial prefrontal cortex and DLPFC, and inferior orbital and polar frontal cortex. According to (Figure 3.8), these two clusters show CSF-like behavior and they are neither associated with any significant depth effect nor any significant correlation with any layer of SC.

Cluster 2 had a very neat delineation of the areas which are known to be part of the oculomotor system. It included the entire FEF on the right and the superior FEF on the left side associated with saccades and smooth pursuit (Rosano et al., 2002) where the inferior FEF becomes activated by combined eye and head movements (Müri, 2006), ventral LIP

and the VIP were other areas included in the cluster 2 map. These two areas are located in the area called the parietal eye field (Müri, 2006; Müri et al., 1996; Van Essen et al., 2001). The parietal eye field is involved in triggering of reflexive saccades to suddenly appearing peripheral visual stimuli (Pierrot-Deseilligny, Milea, & Müri, 2004) which becomes more interesting when considering that the parieto-occipital junction labeled as V6 and V6A, lateral posterior area 7 (7PL) posterior IPS and only the peripheral V1 together with the peripheral visual areas of the secondary visual cortex (V2, V3, and V4) were the other parts of this cluster. POJ and the sections of the visual cortex perceiving the peripheral vision were identified as a part of the network responsible for peripheral reaching (Prado et al., 2005). The same locations, namely the posterior area 7 and the posterior IPS were also claimed to be a part of the peripheral reaching module (Martin, Karnath, & Himmelbach, 2015). Besides all the aforementioned, cluster 2 covers PreCuneus Visual Area PCV and area 5mv. The trunk section of the primary somatosensory cortex areas 1, 2, and 3a, as well as a fragment of the trunk area in the primary motor cortex, also belonged to this cluster. Another interesting observation was that the pro-striate cortex (ProS) was also detected as a part of the cluster 2. This area was repeatedly described as a fast responder to moving stimuli in the peripheral visual field (Mikellidou et al., 2017; Rockland, 2012; Yu, Chaplin, Davies, Verma, & Rosa, 2012), which is in line with the other cluster members functionality. It is not coming as a surprise that the magnocellular LGN is also another part of the cluster; a low latency part of LGN which distributes the essential and basic information of the preceived image (Cheng, Eysel, & Vidyasagar, 2004; Jeffries, Killian, & Pezaris, 2014). Interestingly, the clustering algorithm put the MT+ complex and the superior temporal visual area (STV) into a different cluster. We know from the literature that the MT+ and the STV are parts of the ventral-dorsal pathway processing complex visual motion related to locomotion and pursuit (Lappe, Bremmer, Pekel, Thiele, & Hoffmann, 1996; Nassi & Callaway, 2009; Siegel & Read, 1997). MT, in particular, does not respond to peripheral motion (Huk, Dougherty, & Heeger, 2002). All shreds of evidence are pointing at the fact that cluster 2 is pretty much involved in the fast perception of peripheral visual field stimuli as well as the trunk sensory input and triggering the commensurate trunk and eye movement. It is noteworthy that the dorsal visual transitional area (DVT) is also located in this cluster, but it is not much known about it since it is a newly defined area. The speculation is that it plays an important role in planned movements, spatial reasoning, and attention (Baker, Burks, Briggs, Conner, Glenn, Sali, et al., 2018).

Cluster 4 is a combination of functionally diverse areas. One patch located anterior to the occipital cortex comprises parts of the ventral-dorsal stream and the ventral stream pathways; these two complexes help with the object recognition and analyzing the location and the trajectory of moving objects (Ajina, Kennard, Rees, & Bridge, 2014; Katsuyama, Usui, & Taira, 2016; Strong, Silson, Gouws, Morland, & McKeefry, 2016). Anterior to this patch we have the TPO junction and the STV; these are cortical multimodal integration units, being involved in a variety of cognitive functions including visuospatial recognition, working memory, musical memory, and face and body recognition (Baker, Burks, Briggs, Conner, Glenn, Taylor, et al., 2018; De Benedictis et al., 2014). Another more extensive patch of cluster 4 expands from the lateral parietal lobe, anterior to the lateral secondary visual area, to the anterior cingulate cortex and medial prefrontal areas. It covers a manifold of areas in between, such as vast areas of the primary sensory-motor cortex, premotor area, insular, and orbitofrontal cortices. Area PFt being located on the posterior bank of the postcentral sulcus is important in grasping objects under visual guidance (Mars et al., 2011). This region is also activated when individuals observe the use of tools to move objects (Passingham, Chung, Goparaju, Cowey, & Vaina, 2014). The same is true for area PFop, plus this latter is also involved in motor planning and action-related functions (Mars et al., 2011). Area IPS1 on the posterior, superior bank of the intraparietal sulcus, has shown to be important in mentally visualizing the process of grasping objects as well as action associations and object function (Mruczek, von Loga, & Kastner, 2013). Likewise, area AIP is involved in shaping the hand for visually guided grasping activity, as well as object recognition (Fogassi et al., 2001; Galletti & Fattori, 2018). LIPd, located centrally on the superior bank of the intraparietal sulcus, is implicated in the control of attention and eye movements (Grefkes & Fink, 2005). Another area on the parietal cortex which is also part of cluster 4 is MIP. This region is found in the posterior portion of the superior bank of the intraparietal sulcus and is involved in the control of arm-reaching movements and grasping (Galletti & Fattori, 2018). It receives proprioceptive signals (Prevosto, Graf, & Ugolini, 2009), transforms visual information into motor action for precise movement, adjusts reaching movements, and corrects movement errors (Grefkes & Fink, 2005). MIP together with area 5L has the lowest clustering reproducibility chance among regions belonging to cluster 4, which nevertheless, is over 60% on average. Cluster 4 covers almost the entire somatosensory cortex, except for certain areas belonging to the upper limb region of area 2 and 3a. We cannot confirm to what extent the upper limb was excluded, but a comparison with motor task studies suggests it to be arm and hand areas. Meanwhile, the trunk areas of

the entire somatosensory and motor cortex are also kept out of this cluster. At the motor cortex, the lower limb is also excluded as well as almost the entire upper limb and a small section of the trunk area. Operculum areas that are known for integrating sensory responses, especially tactile information into motor actions were also parts of this extensive cluster. In addition, there is an apparent presence of the auditory cortex sections and posterior insular areas, involved in processing sensory inputs in a close relationship with the primary and the secondary motor areas (Chen et al., 2016). Areas 5L and 5m contribute to goal-oriented hand movements like reaching and pointing, specifically when the movement is not based on visual cues (Scheperjans, Palomero-Gallagher, Grefkes, Schleicher, & Zilles, 2005). Against our expectation, the premotor cortex is not part of cluster 4 or any other cluster with significant correlation, except for the eye fields and a part of area 6a of the dorsal premotor area. The precise function of area 6a is unknown. The dorsal premotor cortex, however, is involved in associating informational cues with a particular body movement. The ventral premotor area, however, is involved in more complex cortical functions such as when individuals learn actions or movements while observing others performing a task (Chouinard & Paus, 2006). Area 24dv located in the anterior inferior paracentral lobule has been implicated in complex motor planning and regulation of muscles in the upper limb and upper trunk (Vogt & Vogt, 2003). Located anterior to the dorsal-lateral 24 region, area p32pr is involved in stimulus and response selection in movement planning (Devinsky, Morrell, & Vogt, 1995). The last major patch of this cluster was a distinct stripe stretched along the inferior frontal sulcus and was slightly diffused into the MFG areas 8C and p9-46v. In the right hemisphere, this stripe starts from the premotor eye field. IFJ is known to be associated with cognitive control, goal-directed and stimulus-driven attention, and feature-based attention which is necessary for identifying an attentional target in a complex scene (Asplund, Todd, Snyder, & Marois, 2010; Brass, Derrfuss, Forstmann, & von Cramon, 2005; Sundermann & Pfleiderer, 2012; Zhang, Mlynaryk, Ahmed, Japee, & Ungerleider, 2018); as well, the MFG areas are involved in interpretation of complex visual information and attention and goal-directed higher-order cognitive processes (Nitschke, Köstering, Finkel, Weiller, & Kaller, 2017; Petrides, 2005; Reser et al., 2012).

The functional properties of the areas in cluster 4 indicated that as a network this cluster is the location of sensory inputs integration to assist with planning goal-oriented hand action. The existence of such a network in association with SC had been suggested in

animal studies (Borra, Gerbella, Rozzi, & Luppino, 2017; Borra et al., 2012b; Mikulić, 2010; Song, Rafal, & McPeek, 2011), but there was no comprehensive human study that could thoroughly address this question that whether a homolog SC network exists in the human brain. Nevertheless, (Borra et al., 2017) prediction suggests the involved areas in the human lateral grasping network, which has many areas in common with cluster 4.

Cluster 5 is mainly localized at the posterior cingulate cortex and medial superior parietal cortex. It is pretty difficult to assume a clear function for this part of the brain since it is involved in a diverse range of functions. Dorsal PCC plays a role in spatial processing and visuospatial/body orientation, while ventral PCC is suggested to be part of object processing in perceived and imagined stimuli (Vogt, Vogt, & Laureys, 2006). The precuneus portions also support a variety of cognitive tasks. The entire PCC was also repeatedly identified as part of the default mode network (DMN). Areas 7Al and 7Am are involved in space, vision shape and motion, working memory, and execution information processing. They are also involved in self-centered mental imagery and attentional processes (Scheperjans et al., 2008; Wang et al., 2015). Another noteworthy part of this cluster is the entire foveal area of the primary and the secondary visual cortex. The fact that the rest of the areas belonging to this cluster are scattered in DLPFC, orbital and polar frontal, and medial prefrontal cortex which all are also parts of the DMN raise the question of why the foveal visual cortex has been assigned to this cluster.

The major part of cluster 6 was the parafoveal area of the primary visual cortex. Other patches, more pronounced on the left hemisphere, were also visible on the lower parafoveal representation of V2 and the V3 as well as the precuneus visual area (PCV). Together with nearly the entire thalamic area, it seems this cluster is representing the pure visual functional network of the superior colliculus which has been well-described in the literature.

3.4.3 Networks SCDP characteristics

The clusters mean SCDP or so-called centroids SCDP generally followed a descending trendline. They all reached their local maxima at one of the first two layers, and the correlation values decreased by depth, afterward. What made the centroids SCDPs distinct were the averages of their correlation values across the depth and the steepness of correlation value changes from one layer to the next. A comparison of the centroids SCDP correlation values suggested that the same results might be obtained by feeding our

clustering algorithm only the correlation values and leaving the gradients out. However, conducting the same analysis on this suggestive feature set led to a different outcome, with a different spatial distribution of clusters and accordingly, different centroids. The same was true using only the gradients as a feature set. Therefore, the gradient values and the correlation values both played an important role in the main clustering result. Therefore, what we observed reflected both the strength of the grayordinates functional connection to SC and the depth-dependent behavior of those connections.

On the way of interpreting the clustering results, another major concern was the fact that the SCDPs might not reflect the true characteristics of the SC anatomy. SC is a midbrain structure, thus the value of the correlations is dependent on the average signal of the SC ROI; this value is prone to the ratio of the neuronal cell body volume to the total volume of an ROI. Less density might lead to smaller correlation values comparing to another ROI while it does not necessarily mean that the actual neural population of the first ROI is smaller. In our analysis, we passed the samples to the k-means clustering after normalizing them across subjects, so it will not be vulnerable to such anatomical misinterpretations.

According to Borra et al. (2012b) macaque inferior parietal (PFG and anterior intraparietal [AIP]), ventral premotor (F5p and F5a), and ventrolateral prefrontal (rostral 46vc and intermediate 12r) areas are parts of a network involved in controlling purposeful hand actions, which is pretty similar in function to cluster 4. We do not know the exact homolog of all these areas in humans. However, cluster 4 included areas that indicate the corresponding regions e.g. PEF in ventral premotor, IFJ, IFS, and p9-46v in the lateral frontal area as well as AIP. All of these areas were predicted as the possible human counterparts of the nodes of the macaque lateral grasping network (Borra et al., 2017). It was shown that injecting a tracer into these macaque brain areas would project onto intermediate and deep layers of SC (Borra et al., 2012b). The abovementioned can be a probable explanation of why we observed a correlation elevation in the second layer relative to the other clusters centroids SCDP. Table 3.1 shows a summary of a study by Fries (1984b). It shows the connection between layers of the SC and the Brodmann areas in which they could find labeled cells. Here X means the connection is exclusive and XX means that the connection does not necessarily exist, because the contrast was not exclusively injected to that specific layer. This table suggests that the clusters which do not have areas connected to the superficial layer must show a relatively lower correlation in

more superficial layers. This assumption holds as in our results, cluster 2 and 6 had the highest correlation values in superficial layers. On the other hand, cluster 4 had the lowest correlation value in the superficial layers among the clusters with significant correlation levels. This cluster included areas which only have connection to the deep SC, according to the table. This is in line with the fact that this cluster has the lowest correlation reduction rate in the intermediate layers among the clusters with significant correlation value.

Table 3.1 - Summary of (Fries, 1984a) results. The table demonstrates whether there is conclusive evidence for a connection between an SC layer and a Brodmann area (X), the connection is probable but not definitive (XX) or there is no connection.

	2	6	7	8	9	14	17(V1)	18(V2)	19(V3-5)	20 ITG	21 MTG	22 STG
Superficial SC		X		X			X	X	X			
Intermediate SC		XX	X	XX			XX	XX	XX			
Deep SC	XX	XX	XX	XX	XX	XX	XX	XX	XX	XX	XX	XX

The pattern of cluster 6 SCDP revealed that the parafoveal visual area of V1 had an exclusively low correlation with the intermediate layer of the SC, while the SCDP gradient becomes positive in deeper areas. However, Fries study could not predict this behavior, accurately, their report agrees with our new findings.

CHAPTER 4   STRUCTURAL MAPPING OF THE HUMAN MIDBRAIN (SC)

4.1 Introduction

The brainstem is a huge neuroanatomical hub and it connects the essential parts of the human central nervous system. It is not only a highway of processed neural information, but also home to many processing and control units that regulate vital human functions (Nicholls & Paton, 2009), including respiration and cardio-vascular functions (Cechetto & Shoemaker, 2009; Faull, Jenkinson, Clare, & Pattinson, 2015; Pattinson et al., 2009; Topolovec, Gati, Menon, Shoemaker, & Cechetto, 2004) as well as other vital nodes of all functional systems in the central nervous system, such as the visual, auditory, gustatory, vestibular, somatic, and visceral senses, and the somatomotor pathways (Beissner & Baudrexel, 2014). The brainstem also contains cholinergic, dopaminergic, noradrenergic, and serotonergic nuclei which are essential to the regulation of arousal, behavior, and cognition (Florian Beissner & Baudrexel, 2014). Despite its undeniable role in maintaining vital nervous system functions and its involvement in many known neurological disorders, the brainstem remains understudied in the human neuroimaging field. Multiple factors make it challenging to perform imaging of the human brainstem with the current in-vivo techniques: its location relative to large arteries and ventricles; the small size of its substructures; and the fact that, unlike the cerebral cortex, in the brainstem, there is no clear boundary between white-matter and grey-matter (Nicholls & Paton, 2009).

Recent technical advancements in the magnetic resonance imaging (MRI) sequence development field and the increased availability of high-field MRI scanners opened a new door into the study of the human brainstem anatomy. However, because the tissue magnetic properties of the human brainstem are still not fully known, the MRI sequences currently available are not optimally developed to capture the brainstem topology. Consequently, the acquisition of multi-modal MR imaging is essential to build a more comprehensive map of

the human brainstem anatomy and its underlying tissue architecture. In particular, there is an increasing interest in the acquisition of quantitative MR imaging sequences, which allow more precise mapping of the tissue architecture. The most widely used quantitative sequences for brain anatomy mapping are R1, R2*, diffusion imaging, and quantitative susceptibility mapping (QSM) while the sequences used to acquire each of these modalities are varying among different articles (Iglesias et al., 2015; Sclocco, Beissner, Bianciardi, Polimeni, & Napadow, 2018; Soria et al., 2011; Straub et al., 2019; Weiskopf, Mohammadi, Lutti, & Callaghan, 2015).

The midbrain, or mesencephalon, as the most rostral part of the brainstem, sits above the pons and is adjoined rostrally to the diencephalon. The principal regions of the midbrain are the tectum, the cerebral aqueduct, tegmentum, and the cerebral peduncles. The tectum is comprised of the inferior and superior colliculus (SC). The tegmentum (Latin for "covering") is the phylogenetically-old part of the brainstem and runs through the pons and medulla oblongata and located ventral to the cerebral aqueduct. In the adult brain, it contains most of the brainstem nuclei. Cerebral peduncles are placed anterior to the tegmentum and are composed of large tracts that run to and from the cerebrum. The crus cerebri usually refers to the most anterior, semilunar shaped bundle of white matter fibers in the midbrain, including the corticospinal tract centrally (3/5 intermediates) as well as the corticopontine (fronto-pontine and temporo-pontine fibers) and corticobulbar tracts. The substantia nigra is located anterior to the crus cerebri, and the mesencephalic tegmentum is posterior to that. "Cerebral peduncle" is commonly used synonymously with the crus cerebri alone, but most traditionally refers to the cylindrical shaped combination of the crus cerebri, substantia nigra, and tegmentum (Hirsch et al., 1989; Standring, 2015). The cerebral aqueduct surrounded by the periaqueductal grey (PAG) are other structures within the midbrain.

The brainstem nuclei are densely located adjacent to each other which induce several challenges at the image processing level. In particular, relatively small errors in the co-registration procedure can lead to increased variance or decreased sensitivity in structure detection (Napadow, Dhond, Kennedy, Hui, & Makris, 2006). Additionally, low sharpness at the sub-structure borders makes the co-registration step more challenging, specifically for the nuclei far from the surface and deep within the brainstem. Napadow et al. (2006) developed co-registration algorithms optimized to be used in the brainstem and its nuclei. Nonetheless, besides high-quality images and efficient registration technics, novel

quantitative approaches to deduct complex dependencies out of MR images, are still required to better understand the biological underpinnings of MR contrast and brainstem tissue architecture. Modern segmentation methods founded upon deep learning algorithms are powerful toolkits to produce homogeneous results based on the feature space they have been trained over. By building a smart feature space we can improve our learning function. In particular, for the case of structural MR image segmentation, it is possible to define various features related to the voxels intensity or its spatial position which intuitively are capable of characterizing brainstem sub-structures. Deep networks are capable of coming up with a linear or nonlinear combination of the original handcrafted features that best characterize the midbrain structures and discriminate between each of them. Consequently, this approach might enable us to distinguish between two unrelated sub-structures that share the same range of intensity or are in close vicinity of each other. One effective way of controlling the behavior of the deep network when creating the abstract representation of the original feature space is to use labeled data to inform the network of the desired final result That means the network needs ground truth labeled data to optimize the network weights and biases to learn how to assign each observation to the corresponding label, as each observation is characterized by the original hand-crafted feature space. Despite the benefits that a labeled data offers, it could also bring in disadvantages or have certain shortcomings. Labeled data needs to be prepared by a specialist using the original dataset, or needs to be adapted from the current existing atlases. Both of these methods would introduce human-induced or analytical bias in the analysis. Fully unsupervised clustering can detect any homogenous physical pattern within the data without being prone to the abovementioned biases. Inspired by many successful applications of deep learning in both supervised and unsupervised problems, many of the recent works on clustering are utilizing deep neural network ideas to improve the feature representation simultaneous with the clustering results. This pairing is commonly referred to as deep clustering (Min et al., 2018). The number of recently developed deep clustering algorithms is immense, but the entire deep clustering procedure is defined by three choices: 1) selection of the neural network architecture, 2) selection of the loss function, and 3) choosing the performance evaluation metric. However, the use of deep learning is becoming more prevalent in MRI studies, yet the application of that has remained limited in human brain segmentation, and especially in brainstem areas (Litjens et al., 2017). Among all deep clustering methods, deep embedded clustering (DEC) (Xie, Girshick, & Farhadi, 2016) is one of the first yet novel algorithms that attracted attention toward the application and implementation of deep

neural networks in unsupervised learning (Min et al., 2018).

In a previous study, it was shown that it was possible to identify unique features in quantitative MRI data acquired at 9.4T (Loureiro et al., 2018). However, it was also found that the exact boundaries of the SC are difficult to delineate. In the present work, we explored the possibility to exploit specific MRI-features within the human brainstem and use that information for tissue segmentation by the use of a deep clustering method based on a deep neural network and unsupervised learning approach. By using a novel approach that differentiated subtle features in the midbrain from multimodal high-resolution MR maps acquired at 9.4T, we investigated the plausibility of in-vivo human brainstem segmentation with a focus on the superior colliculus (SC). We optimized the algorithms in-use to fully exploit all parameters necessary to best identify the SC, however, we could still recognize some other prominent sub-structures in the midbrain. Therefore, besides the SC, we also identified the boundaries of other midbrain sub-structures such as the substantia nigra (SN), red nuclei (RN), periaqueductal grey matter (PAG), and the inferior colliculus (IC).

4.2 Methods

4.2.1 Participants

Ten subjects from the study of Loureiro et al. (2018) had quantitative MRI data with satisfactory coverage along the rostrocaudal axis (including both the superior and the inferior colliculi) age between 27 to 34 were used in the present study.

4.2.2 MR data specification

All measurements were conducted on a 9.4T whole-body MRI scanner (Siemens, Erlangen, Germany), using an in-house-built head-coil with a 16-element dual-row transmit array and a 31-element receive array (Shajan et al., 2012).

Four main sequences were acquired: 1) a whole-brain MP2RAGE (Marques et al., 2010), used to compute R1 maps (Hagberg et al., 2017); TI1/TI2=900/3500 ms; FA=4/6°; TR=6ms; volume TR=9 s; TE=2.3ms; 0.8 mm isotropic voxel size; GRAPPA=3; partial Fourier factor (PF)=6/8; and TA=9 min 40 s; 2) a zoomed 3D FLASH multi-echo sequence (ME FLASH), used to calculate the R2* maps; FA=5o; TR=41 ms; TE=6-30 ms in steps of 6 ms, 0.4 mm isotropic voxel size, GRAPPA=2; PF=6/8; and TA=13:34 min; 3) a zoomed acquisition weighted sequence (AW) (Budde et al., 2014a) with FA=8o, TR=24

ms, TE=16.5 ms, voxel size=0.132x0.132x0.6 mm³, matrix=1024x1024x16, and TA=14:45 min, which was processed to obtain susceptibility maps; 4) a zoomed 2D FLASH sequence (FLASH orient) was used for optimized slice positioning of the acquisition weighted sequence with FA=10o, TR=2:14 min, TE=6-42 ms in steps of 6ms, voxel size=0.4x0.4x1.0 mm³, and TA=14:45 min that. We optimized the TE of the AW sequence for higher contrast in the midbrain region and to increase stability phase values in this region after visual inspection of the phase evolution at different echo times, (for more details about the sequence parameters see (Loureiro et al., 2018)).

4.2.3 MRI data preprocessing

Data used in this project was originally preprocessed by Loureiro et al. (2018) and the next three sections (4.2.3.1 – 4.2.3.3) are directly taken from their work.

4.2.3.1 Relaxometry: R1 and R2* maps

MP2RAGE images were reconstructed and T1 maps were calculated offline using a custom-built script in Matlab, as described previously, and included correction for both flip angle and inversion efficiency deviations (Hagberg et al., 2017). The T1 maps were used for normalization into a standard brain space (described below), whereas the longitudinal relaxation rate was used for the depth profiles and CNR calculations and was computed as the inverse of the T1maps.

Maps of the effective transverse relaxation rate (R2*) were generated by non-linear fitting (based on a steepest-descent Loevenberg-Marquardts algorithm) of a mono-exponential signal decay to the square of the signal intensity in the multi-echo images (McGibney and Smith, 1993; Miller and Joseph, 1993).

4.2.3.2 Susceptibility Mapping (QSM)

AW GRE images were reconstructed offline as described in (Budde et al., 2014a). The phase images obtained from the 31 receiver channels were combined using a phase-sensitive coil combination algorithm.
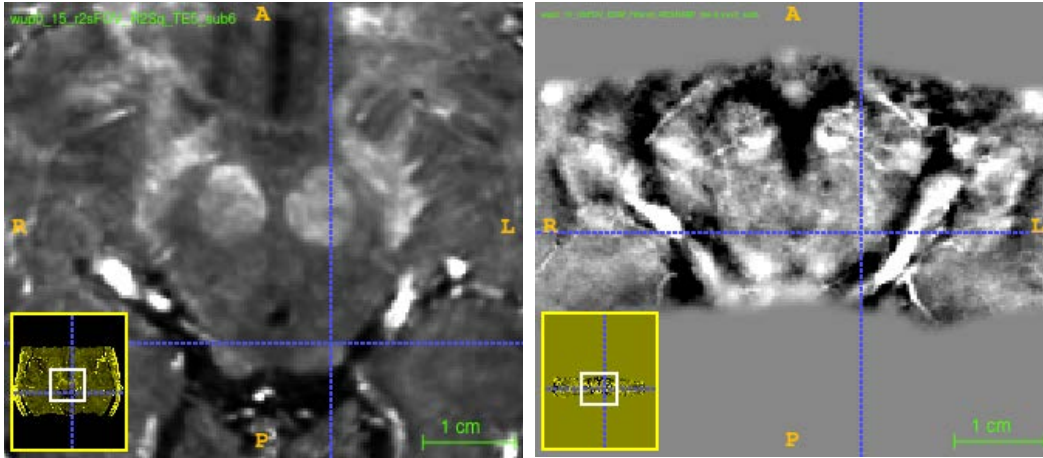
Figure 4.1 - Example axial slice of R2* map (left) and QSM (right) of the same subject at the level of inferior colliculus

To avoid background noise a brain mask was generated from the magnitude images of the AW sequence using BET from FSL and applied to the phase images. In a first step, we corrected for phase aliasing using a fast phase unwrapping method from the MEDI toolbox based on the 3D Laplacian algorithm (Li et al., 2014). The phase images were then demeaned (i.e the median phase value inside the brain mask was subtracted from each voxel). The masked phase images were then background corrected using the RESHARP algorithm (Sun and Wilman, 2014) with a Tikhonov parameter (TP) of 10-6 and a kernel size of 2 times the third dimension of the voxel size. These parameters were chosen since they yielded the best performance in terms of a low standard deviation and high CNR measures in the SC, then 23 other settings tested (increasing TP from 10-1 to 10-6 and increasing kernel sizes for each TP from 2 times the voxel size to 6 times the voxel size in the third dimension). After background removal, the QSM maps were obtained by applying the iterative least-squares approach (Li et al., 2015).

4.2.3.3 Multi-modal Co-registration and Image Resampling in Native Brain Space

The three modalities were co-registered using SPM12 for direct comparison. For all the steps the average distance between sampled points was a vector with increasingly finer points from 4 to 0.2mm (4, 2, 1, 0.5, 0.2mm) to increase precision. Due to the small field of view of the zoomed sequences, the co-registration included four main steps: 1) The 3rd echo of the ME FLASH sequence (source image) was co-registered to the magnitude of the AW sequence (reference image) and this transformation was applied to the remaining echoes of the ME FLASH sequence; 2) The T1map (source image) was co-registered to the third echo of the ME FLASH sequence (reference) and the transformation was further applied to the T1 weighted contrast obtained from the MP2RAGE sequence and to both

inversion times (Figure 9 A, B); 3) The R2* maps were upsampled to a 0.15mm isotropic grid using linear interpolation and all the images were resliced to the same grid. This step guaranteed that all the sequences have the same FOV as the ME FLASH sequence, which enabled us to improve the co-registration between the T1maps and the high resolution zoomed images; 4) automatic co-registration was applied in the new resliced images using the T1maps as the reference image and the R2s maps as the source. This transformation was applied to all the other contrasts.

To bring all the subjects into a common space, we normalized the data to MNI space using DARTEL from SPM12. A DARTEL template was created from 45 subjects acquired with the same MP2RAGE sequence at the 9.4T in Tübingen. All the upsampled co-registered images were then wrapped to MNI space with a resolution of 0.3 mm isotropic using the flow fields generated for each subject from the transformation of the segmented whole-brain T1maps to MNI space. The images of the different contrasts were then averaged across subjects in this common brain space (Figure 9 E, F). The R1 maps were relevant as they were the only whole-brain maps acquired so they were used mostly to aid in the registration process. However, due to their low resolution compared to the R2* and QSM maps the R1 maps were not included as features in the DEC approach (described below).

4.2.4 Deep unsupervised clustering

To reveal the hidden features of our data and to segment the midbrain area in an unsupervised fashion, we used DEC to learn the anatomical properties of our unlabelled data. To restrict our analysis to the target regions, we used a 3-dimensional box of size 110x110x34 mm³ (length x width x height) on the midbrain, placed symmetrically around the mid-sagittal plane which includes the SC, SN, RN, IC, PAG, and crus cerebri. We treated each voxel within this box as an observation of our learning system. The second dimension of the input matrix refers to the feature vectors of the observations that were generated from the two quantitative MR maps acquired for each subject as described below

4.2.4.1 Original feature set

A total of 16 different, subject-specific spatial features were generated from R2* and QSM for each voxel. As such a feature space consisting of 160 dimensions, made up of the 16 features from every 10 subjects was obtained. Including features for each subject was important to account for the between-subject variability of the anatomical areas.

For each of the two quantitative MRI-maps (R2* and QSM) the following 8 subject-specific features were generated: 1) The voxels intensity value; 2) the sum of the squared values of the image gradient calculated in all 3 directions; 3) the mean intensity and 4) standard deviation values of neighboring voxels, allowing us to reduce the effect of any intrinsic variability for each voxel; 5) product of the distance from the central plane and mean of the neighbors' intensity values and 6) product of the distance from the central plane and standard deviation of the neighbors' intensity values, to account for the mid-sagittal plane symmetry; 7) product of the distance from the most posterior plane and the mean of the neighbors' intensity values and 8) product of the distance from the most posterior plane and the standard deviation of the neighbors' intensity values. These eight values were calculated for each voxel in each modality (R2* and QSM) for each of the 10 subjects, which builds up to 160 features for the primary feature space.

4.2.4.2 Number of clusters

One common dilemma while using unsupervised learning approaches is choosing the correct number of clusters (k-value), a problem that we also came across in chapter 3 (please see sections 3.2.7.1 and 3.3.3). Since no ground truth labeling exists, a decision on the k value is made intuitively most of the time. To achieve a more objective choice of the number of clusters here, we measured the reproducibility of the clustering results for different values of k.

We employed a leave-one-out approach and normalized mutual information (NMI) as a reproducibility measure. In the case of every single subject, we performed two clustering analyses resulting in two midbrain segmentation maps; one deduced from the data of the individual and the other obtained from the accumulative data of the other nine subjects. Then we calculated the subject-level normalized mutual information (sNMI) between the two resulting maps and repeated as such for every 10 subjects, respectively. As a result, we calculated an average of 10 sMNI scores for each value of k which reflects the reproducibility of the clustering result for every k value ranging between 10 to 200 incrementing in steps of 5.

In the approach explained above, we used conventional k-means instead of DEC which helps to reduce the analysis duration by a factor of 10 and from an estimated 1600 hours down to 160 hours. The fact that the core clustering algorithm in DEC is the conventional k-means suggests that it provides an estimation of DEC behavior for different k-values. However, we lose the benefit of feature optimization provided by the hybrid use

of autoencoder in DEC to save time.

4.2.4.3 Clustering validation

After coming up with the proper value for k (k_{fin}) and running the final clustering analysis, it is necessary to evaluate the consistency of the resulting segmentation for k_{fin}. NMI is one popular method to determine the quality of clustering in comparison with the map of ground truth labels. Since the midbrain data at hand is not labeled, we used NMI to measure the quality of the clustering results by employing a leave one out approach. As explained in the previous section we calculated sNMI scores for each subject ending up with 10 sNMI values for the chosen main k-value. To investigate whether these values are not randomly obtained and the clustering of every single subject was indeed carrying meaningful anatomical information, we took advantage of a self-customized randomization approach. We randomly permuted the cluster labels of each voxel of the individuals' clustering result and calculated the sNMI value between the permuted segmentation and the segmentation based on the other nine subjects', un-permuted, clustering ($sNMI_{rand}$). By repeating the permutation 10,000 times and calculating 10,000 $sNMI_{rand}$ scores, we created a distribution of $sNMI_{rand}$ scores that helped to measure the information present in a single subject clustering result.

4.2.4.4 Deep Embedded Clustering

DEC trains a deep neural network (DNN) to build an optimized nonlinear translation of the original feature space, called Z and the parameters θ of the DNN that maps data points into Z. DEC initializes the parameters by a deep autoencoder and optimizes the parameters based on the high confidence predictions of the clustering results based on the embedded points $z \in Z$ (please see (Xie et al., 2016)).

Additionally, we used the early stopping method to help against overfitting. We split the dataset at the pretraining stage to 75% training and 25% validation to keep tracing the validation loss after each epoch. The pretraining stops in case the validation loss does not improve in 10 consecutive epochs. Normally, the slope of the training loss function is always negative, and the networks keep improving the discriminative function that describes the training set. However, the loss function of the validation set starts to grow after the networks begin to overfit the training set and therefore the validation loss function is a good indicator of when the pretraining has to stop (Prechelt, 1998).

The advantage of this method is that unlike standard k-means it has access to the

nonlinear combination of the features. This transformed feature space is also optimized throughout clustering by relying on the high confidence clustering results of the last iteration. Therefore, the transformation of the embedded point also improves for the ones with low assignment confidence.

DEC vs. k-means

To measure the advantage that DEC offers in comparison to k-means considering its much longer runtime, we calculated sNMI for every subject twice, using DEC and k-means. This would show whether there is a significant difference between the quality of each method.

4.3 Results

4.3.1 Optimal number of clusters

To choose the optimal number of clusters (k) we repeated the clustering for k in a range from 10 to 200 in steps of 5 using a leave-one-out method and normalized mutual information (NMI) as a reproducibility measure. We calculated the NMI of the clustering result for subject i and the group clustering result for the entire dataset without subject i. Accordingly, 10 NMI values were calculated at each k, and the average of those 10 values was used to estimate the reliability of the clustering outcome for each selected k. As for running this analysis using DEC was tremendously time-consuming we used the simple k-means algorithm instead. We can see the average NMI vs. k plot in figure 4.2. The plot reaches its local plateau at k=95 and k=150. However, it is only after k=145 that the average NMI values keep remaining over the median of 0.44. Accordingly, we chose k=150 as the basis for the clustering analysis.
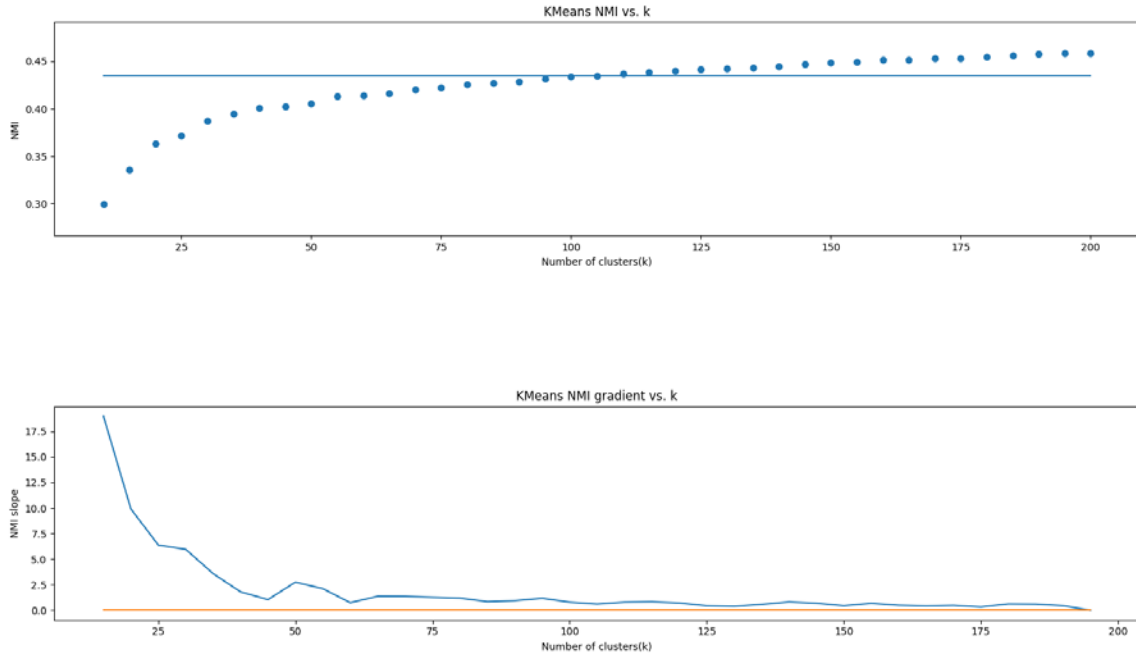
Figure 4.2 - The plot on the top shows the average NMI value after applying a leave-one-out method on each 10 subjects for values of k between 10 and 200 with increments of 5. The blue line shows the median value of 0.44. The plot on the bottom is the gradient of the one above. The orange line indicates zero.

4.3.2 DEC vs. k-means

We ran DEC with k=150 over a 3D MR image window of 110x110x34 (x,y,z) isotropic voxels of size 0.3x0.3x0.3 mm³. This window was placed on the midbrain, with its top plane covering the most superior extent of the tectum (MNI z = -2.1) and extended inferiorly, along the main axis of the brainstem for 10.2mm (z = -12.3). The box was centered on the mid-sagittal plane with a symmetrical extend of 16.5 mm to the left and right. It extended from y = -39 to y = -6 in the coronal direction and thereby included the entire tectal plate and the tegmentum. That provided the learning machine with 411,400 observations where each was explained with 160 primary features. The 160 primary features were later reduced to 120 latent features with the help of a pretrained encoder. The 120 latent features were further optimized by the clustering result after each optimization iteration until the algorithm converged by reaching a state in which less than 0.01 percent of the labels of the total number of voxels changed relative to the previous iteration. Since the centroids of the clusters were initialized randomly, the clustering was repeated 20 times in each DEC optimization iteration and the clustering result with the minimum k-means error (total sum of the euclidean distance of the observations from their clusters) was selected as the clustering outcome of that iteration.
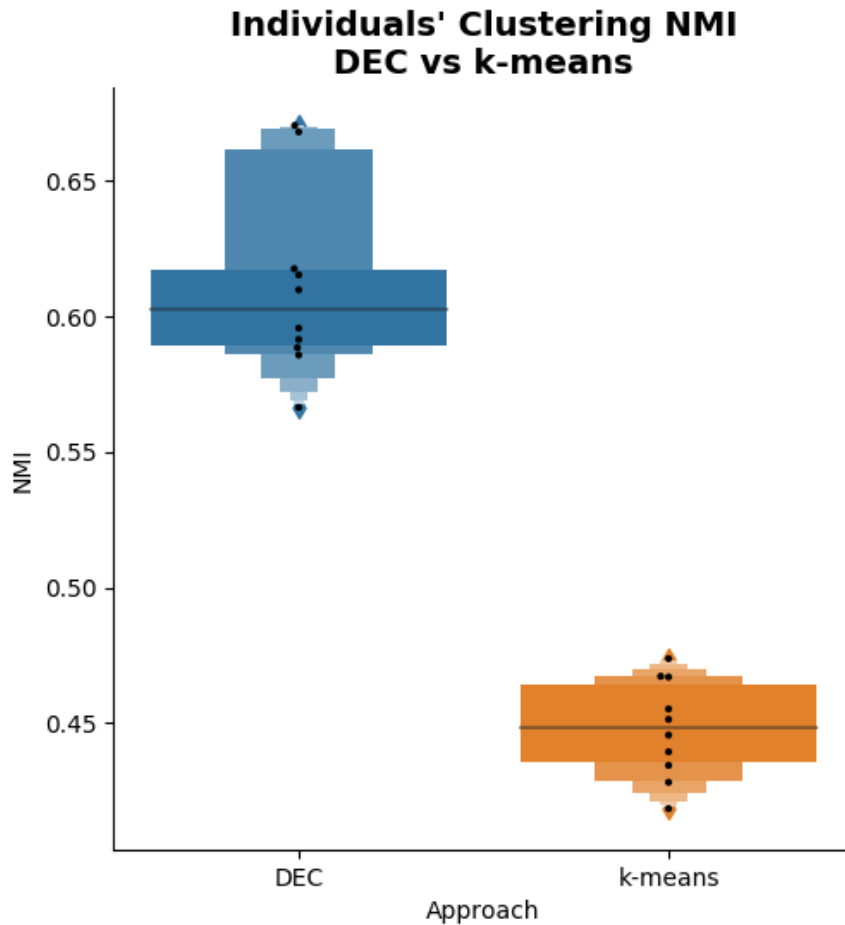
Figure 4.3 - Comparison between individuals NMI values between DEC and k-means.

To evaluate the performance of DEC we compared its results with k-means clustering outcomes for k=150. We quantified the predictability of a single subject clustering from the clustering result of the group of nine other subjects. Accordingly, we calculated 10 normalized mutual information (NMI) values for each subject for both DEC and conventional clustering methods. The distribution of these values in each approach showed that DEC is a more powerful method to build more reproducible results, as the mean NMI of DEC distribution was significantly higher than the k-means distribution mean.

4.3.3 Identified midbrain nuclei

To create an anchor point to show the advantages of choosing higher k we represent the results for k=15, where for the first time (among the selected series of k values) the borders between different anatomical structures and areas, including tectal plate and the CSF cavity becomes visible. In comparison with the outcome of $DEC_{(150)}$, $DEC_{(15)}$

contained much less detail and unveiled only the very general formations of the selected area. However, the estimated clusters appeared to be less cluttered, with neat delineations and uniform segmentations. The most salient features in these images were the clear extent of the red nuclei in red, substantial nigra also in red, the tectum, and the midbrain tegmentum in dark blue. The crus cerebri was also identifiable in pink immediately anterior to the substantia nigra. A crude estimation of the periaqueductal grey matter was detectable in light blue. However, it was combined with the quadrigeminal cistern and the cerebral
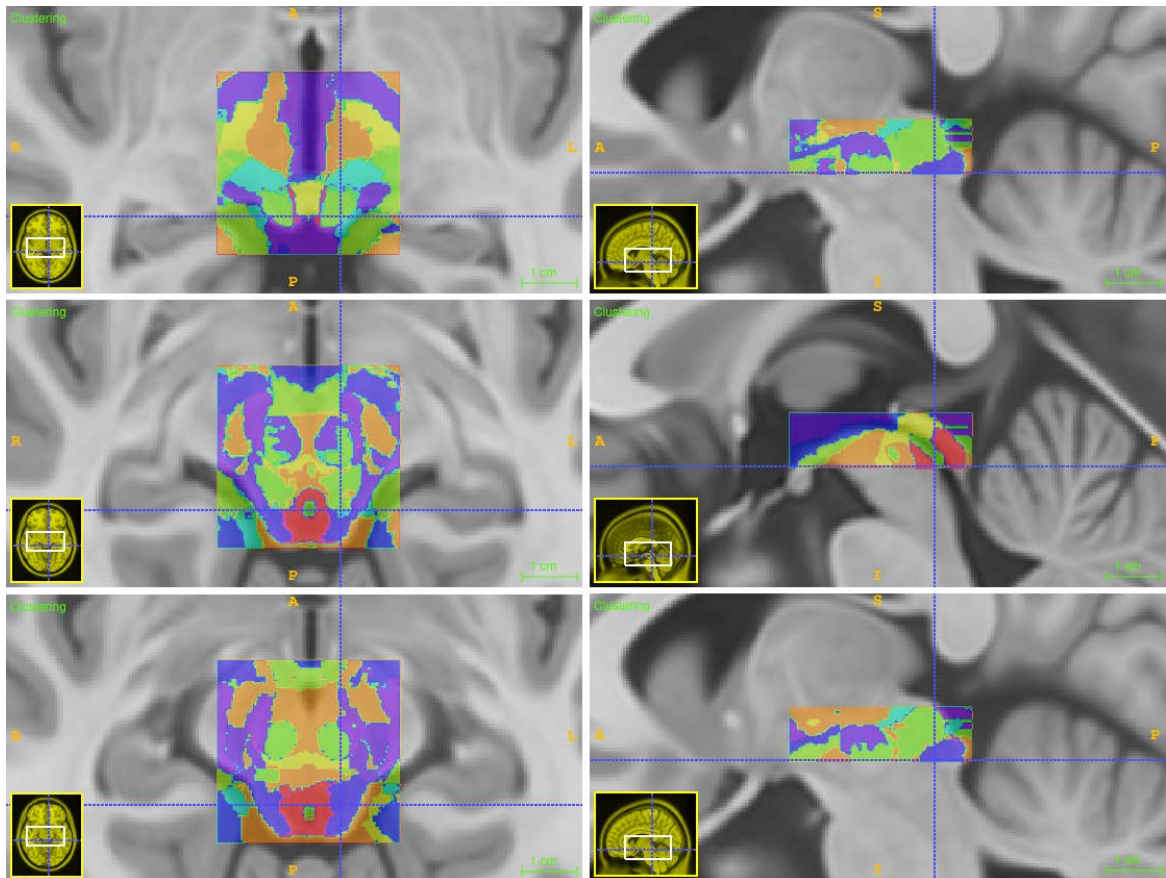
Figure 4.4 - Clustering result overlayed on top of 0.5mm MNI template in 3 axial (left) and sagittal (right) slices.

aqueduct.

Both RN and the SN appeared first at z = -4.8 and extended caudally to the most inferior slice. We were unable to confirm the caudal end of these structures due to the limited FOV of the MRI acquisitions. Crus cerebri, as well, was a quite noticeable structure, however, we could not determine the entire extent of it caudally because of the limited acquisition FOV and laterally, since the selected box did not include the outer parts of the crus.

Figure 4.5 - DEC clustering result for k=15. Each box shows an axial slice with slice 1 corresponding to z =-2.1 and 34 to z =-12.3 . Eaxh (x, y) pair corresponds to one voxel position.

Figure 4.6 - DEC clustering result for k=150. Each box shows an axial slice with slice 1 corresponding to z = -2.1 and 34 to z = -12.3. Each pair of values on the x- and y-axis corresonds to the position of a single voxel with respect to the reference anatomical position.

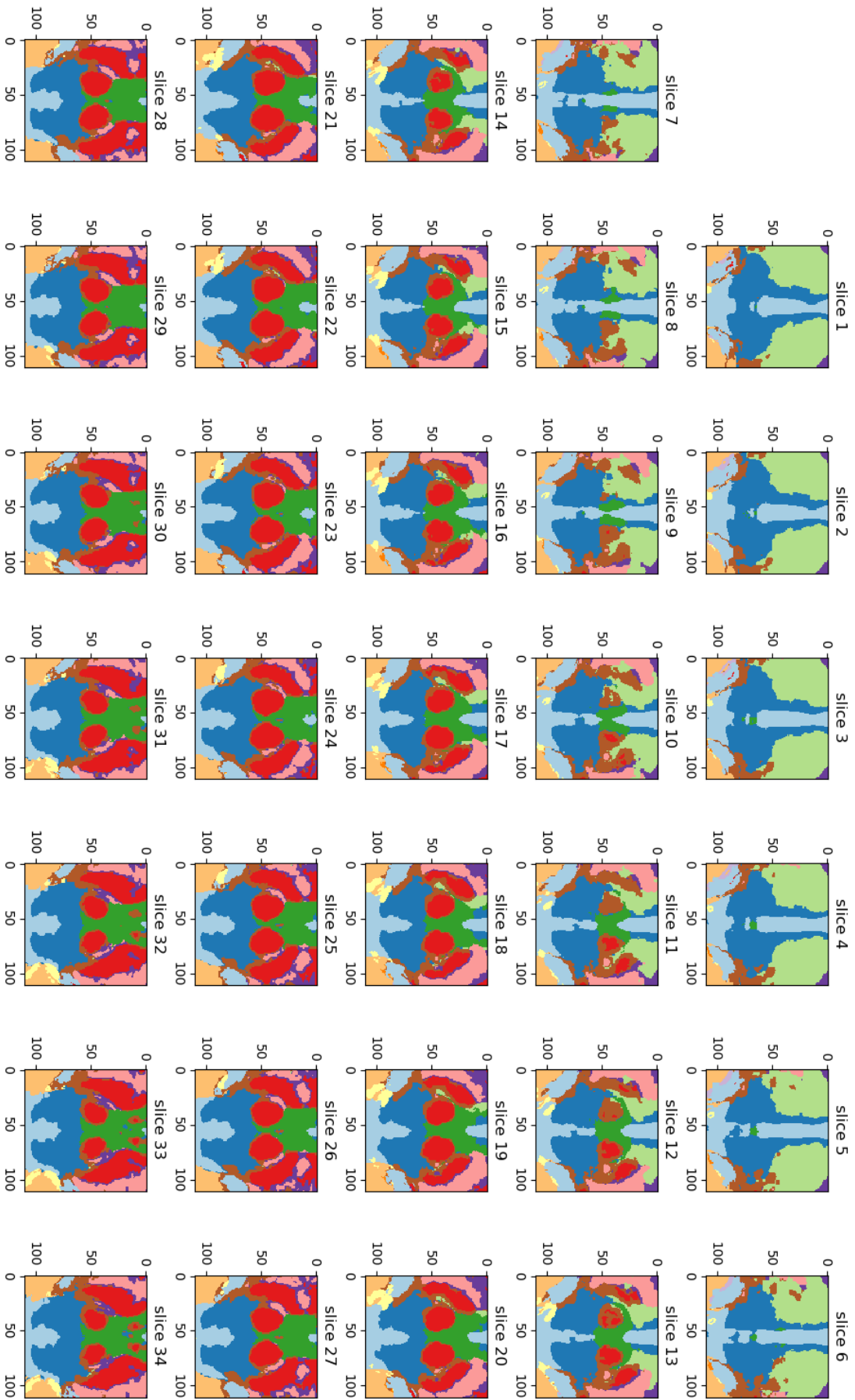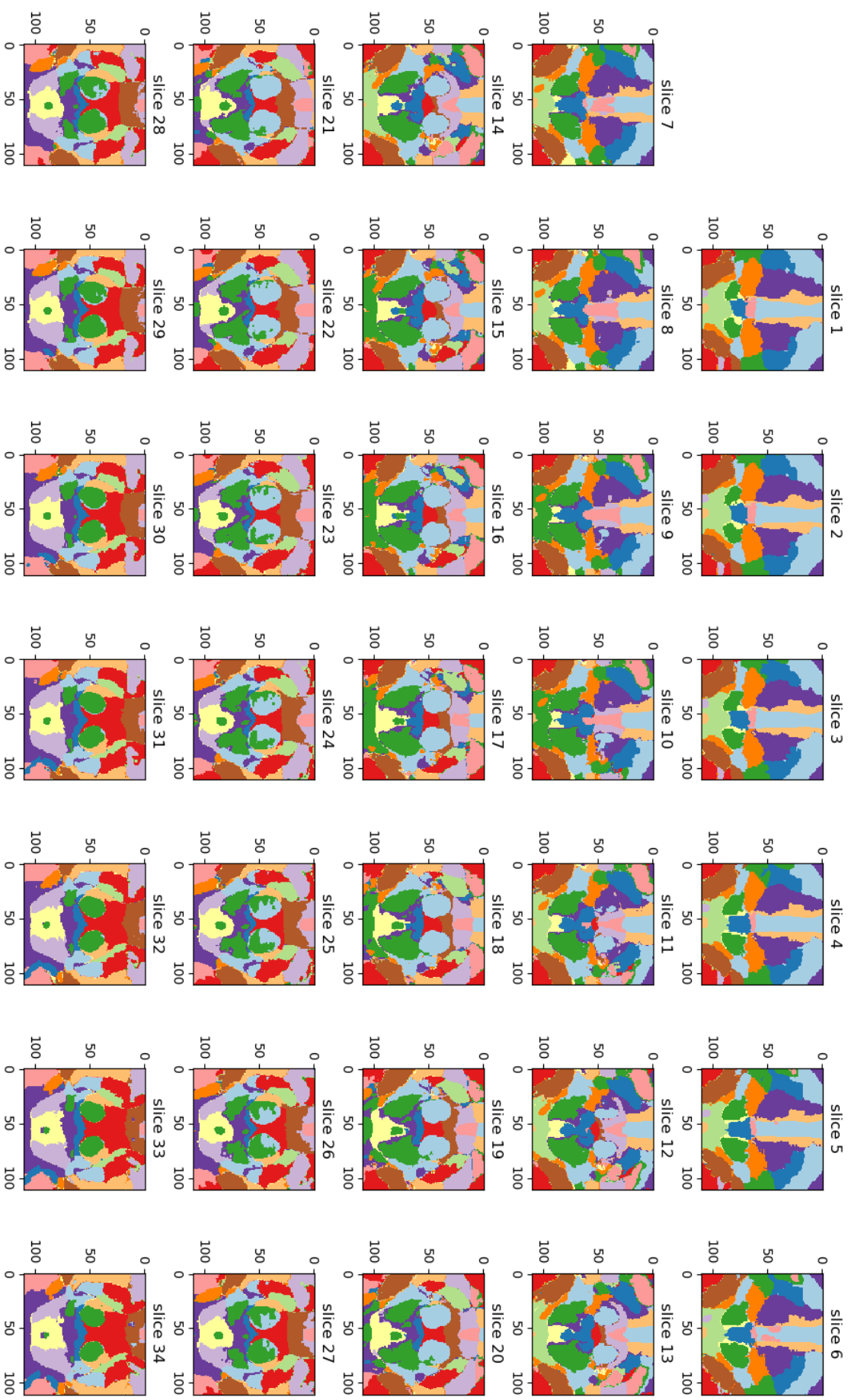DEC$_{(150)}$ relative to DEC$_{(15)}$, exhibited a greater amount of detail. The segmentation maintained its uniformity while it revealed the anatomy of more sub-structures. For instance, the RN was divided caudally and rostrally into two parts from DEC$_{(15)}$ to DEC$_{(150)}$. RN body is indeed known to comprise caudal magnocellular and rostral parvocellular components. The structure of SN identified in DEC$_{(15)}$ was also further divided into 3 areas in DEC$_{(150)}$, which pretty much followed the geometry of the three known components of SN. The pale green patch located ventrally relative to RN delineated the shape of the pars compacta. The red cluster, laterally adjacent to the former patch mapped out pars reticulata and the dorsal light blue tail of pars reticulate and pars compacta clusters delineated the pars lateralis component of SN. Crus cerebri was divided into three subregions in DEC$_{(150)}$. The most ventral part of crus in salmon pink depicted corticopontine (fronto-pontine) tracts, described in previous literature. The middle area in lavender violet depicted pyramidal (corticospinal) tracts and the dorsal tail in amber orange outlined the corticopontine (parieto, temporo, and occipital-pontine) tracts. The dorsal midbrain tegmentum and tectum had also been further divided into anatomically meaningful areas. Unlike DEC$_{(15)}$, there was a clear line between PAG and the quadrigeminal cistern. PAG in yellow encompassed a green cylinder that described the topology of the cerebral aqueduct. Another very interesting cluster was the green patch that covered the rostral part of the tectum. This patch got detached from the tectal plate at z = -7.2 and its caudal tail extended ventrally toward RN. The rostral part of the cluster adjacent to the tectal plate agrees very well with the geometrical definition of the superior colliculus (SC). The inferior tectum cluster in light violet, encompassing laterally the PAG, defined the boundaries of the inferior colliculus.

4.3.4 Reproducibility and validation

We analyzed the individual level reproducibility of the clustering for DEC$_{(150)}$, separately for each subject. The average NMI between $DEC_{(150)}^{(i)}$ and $DEC_{(150)}^{(\sim i)}$ (while ~i corresponds to the entire sample size excluding subject i) of all individuals was equal to 0.611. Keeping the cluster sizes in each $DEC_{(150)}^{(i)}$ case, we permuted the order of the dataset observations – which in 3D space can be interpreted as a permutation of voxel positions – 1000 times, and each time we calculated the NMI between the permuted set and the corresponding $DEC_{(150)}^{(\sim i)}$.
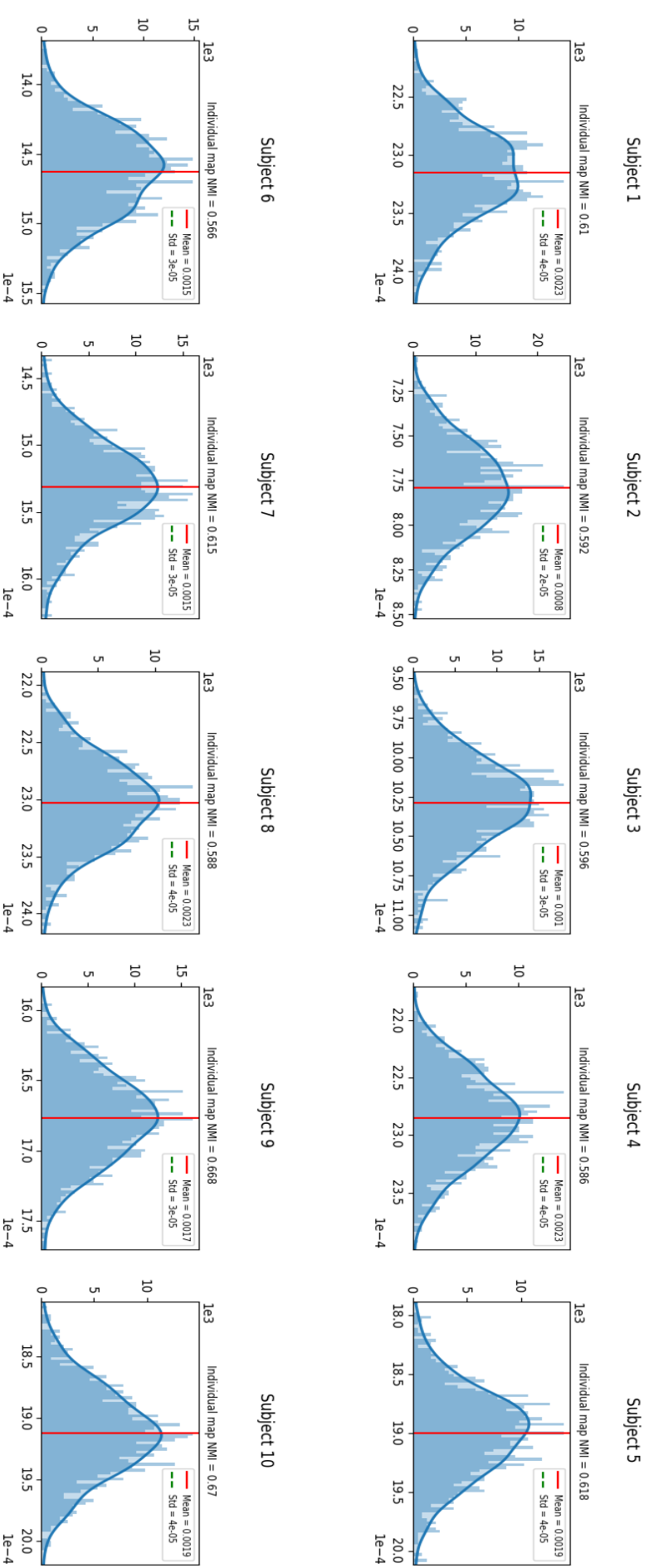
Figure 4.7 - NMI value for each subject in comparison with the distribution of NMI for 10,000 permutations of the individual's clustering labels while keeping the ratio of each label to the total sum.

However, the comparison between this distribution and the NMI value calculated from the actual clustering outcome suggested that it is possible to predict the single subject clustering by having the clustering result provided by a group of unassociated data. In other words, the distributions based on permutations show that it is unlikely to randomly arrive at the NMI values of the actual data.

4.4 Discussion

The current study pioneered the use of deep clustering for human brainstem segmentation. In our approach, without using any labeled MRI data and by relying on the information in the MR images, we successfully identified the human superior colliculus anatomy in-vivo. We partially identified the parvocellular and magnocellular components of the red nuclei, the substantia nigra triplex of pars compacta, pars reticulata and pars laterialis, the periaqueductal gray and the crus cerebri, divided into two bundles of corticopontine tracts and a single bundle of corticospinal tracts. However, due to the limited FOV, it was only possible to spot the more rostral parts of these structures located at the upper part of the midbrain. We built this study upon an earlier report by Loureiro et al. (2018), in which they showed that the values of the MRI quantitative maps in 3 different modalities (T1w, R2* and QSM) change systematically as we move from the surface of the superior colliculus toward its depth. Based on this observation and the same dataset we investigated whether there is any learnable intensity-associated pattern in the combination of all three MR modalities. However, we were compelled to discard the T1 dataset as it was originally acquired in a lower resolution and was upsampled later. We observed that using T1w images induced plenty of artifacts at the edges because of its low sharpness at those regions induced by data interpolation. Using only R2* and the QSM data for 10 subjects, we manually selected a set of primary features, based on which we could train a stacked autoencoder (SAE) to create features of more depth for clustering purpose. The feature set included the voxel value, gradient value, mean of 27 neighboring voxel values, and their standard deviation. The latter two were multiplied with the voxel distance from the mid-sagittal plane and with the voxel distance from the first (top) plane in the coronal view. We built a collection of these features for each voxel of both modalities. Then, we stacked the same feature set from each subject. A total number of over 400,000 voxels with an individual volume of only 0.027 mm^3 was available for the learning stage. We used deep unsupervised clustering, with SAE and k-means working in hybrid to update the clustering result and the trained features in each iteration. Therefore, instead of keep training the

clustering algorithm with the primary hand-crafted features, we optimized a learned feature set of SAE based on the high confidence predictions of the clustering results at the end of each iteration.

To evaluate the performance of DEC we compared its results with k-means clustering outcomes. We quantified the predictability of a single subject clustering from the clustering result of the group of nine other subjects and calculated 10 normalized mutual information (NMI) values for both DEC and conventional k-means clustering methods. The distribution of these values in each approach showed that DEC is a more powerful method to build more reproducible results, as the mean NMI of the DEC distribution was higher than the k-means distribution mean.

One important advantage of an unsupervised clustering approach is that it does not require the labeling of the data. Labeling depends on specialists' opinions based on their subjective judgment. Entirely relying on computer vision and statistics, the final output of an unsupervised clustering approach would be free of any possible fallacious subjective biases. However, neuroanatomist inspections are essential to confirm the final findings of the automatic data labeling.

One of the most recent attempts to map the human brainstem by Straub et al. (2019) used different structural MRI modalities in 3T and 7T. They manually labeled images of 5 subjects in different modalities, comparing each image to histological Loyez stains of a 36-year-old male. The criterion for structure depiction was that a structure could be delineated in the different contrasts with respect to the surrounding tissue based on the knowledge of its location from histology slices. They claimed that QSM in comparison with relaxation measurements R^*2, R1, diffusion tensor imaging (DTI) and T2-and proton density (PD)-weighted imaging is the contrast with which the highest number of structures could be identified. However, the reliance on structure identification by a neuroradiologist might result in subjective misinterpretations. In contrast, we used cutting-edge deep learning algorithms to eliminate human intervention in detecting the boundaries of brainstem nuclei and tracts.

Among all brainstem nuclei, RN and SN received much attention due to their salient structures in MR images. There have been many attempts to locate and delineate these structures (Grossman & Yousem, 1994; Naidich et al., 2009; Schuenke, Schulte, & Schumacher, 2010). However, in most cases, the authors were unable to differentiate

between different components of these structures with conventional MRI technics (Fitzgibbons & Salamon, 2016). One of the most recent efforts (Guo et al., 2018) used a seed point discontinuity-based method to delineate these two structures in 3D QSM data. However, their result was prone to misregistration of images across subjects. They also mentioned manual segmentation as a source of bias in the final evaluation of their results.

Several authors (Haegelen et al., 2013; Kim, Lenglet, Duchin, Sapiro, & Harel, 2013; Y. Xiao et al., 2012; Y. Xiao et al., 2014) described different methods for automatic segmentation of the substantia nigra, subthalamic nucleus, and red nucleus. Although all of these studies used T2- or T2*-weighted MRI data, imaging resolution and MR contrasts varied between studies. The dice score is the most commonly reported measure to compare the segmentation result to the histological map reference, but a comparison of such scores between studies is problematic due to differences in field strength and acquisition parameters, as well as in the manual segmentations that are used. Visser, Keuken, Forstmann, & Jenkinson (2016) used a multimodal image segmentation tool (MIST) for segmentation of the abovementioned structures using FLASH magnitude images and QSM data. Despite all efforts, all methods used were unable to further segment SN and SN into their components. Additionally, another issue might be the use of the right modality to capture the anatomy of the structures. Langley et al. (2015) demonstrated that the delineation of the SN depends on the modality used for the analysis, where susceptibility-weighted images were the better choices for the detection of some midbrain structures such as RN and STN.

We used multimodal data to identify brainstem substructures while treating all modalities equally. It was essentially the deep network that decided how to value each selected image feature from either modality to improve the segmentation function. This approach needs no information about the magnetic quality of the sub-structures or the expected intensity/value of the voxels within them. Nevertheless, such information could further improve the clustering outcome. We successfully identified the human SC for unprecedented detail as well as RN and SN with their sub-components. These together show the power of deep clustering combined with ultra-high-field MR images. Possibly adding more MR modalities as well as more subjects with a wider field of view, covering more volume of the brainstem would be a way to consistently map the entire human brainstem sub-structures that are visible through the acquired images.

CHAPTER 5   CONCLUSION AND FINAL REMARKS

For over a decade, MRI modalities have been the predominant neuroimaging data type in-use for in vivo studies of human brain function and structure. Together with powerful statistical toolsets, MR images substantially improved our knowledge of the human brain. However, that is not entirely including the functional units of the human brainstem. Neither MRI nor any other imaging instrument captured clean and clear signals from most of the tiny brainstem nuclei. Most of the available denoising approaches failed to extract the critical signal of interest from the raw noisy data. This lack of effective techniques caused a huge gap between the little published knowledge over human brainstem function comparing to a large number of studies on human cerebral, cerebellar, and subcortical areas.

Recent efforts to improve functional and structural MR image quality as well as the development of advanced preprocessing pipelines added to the popularity of brainstem and midbrain as a topic of research. Any successful research in the field proves the possibility of further investigation of the human brainstem in-vivo. Our study of the human superior colliculus function and anatomy as exemplar nuclei located on the dorsal surface of the midbrain is a showcase of this area of research potentials.

In the first phase of the project, we depicted the general view of the functional cortical and subcortical connectivity network of human SC. To achieve this goal we used a 3T fMRI dataset with a total of 143 human subjects, preprocessed with the HCP pipeline. Our findings widely agreed with our knowledge of animal studies. Also, we found significant correlations between SC and prefrontal, posterior temporal, premotor, and primary motor cortex, at locations with little prior evidence of connections to the SC from animal models. This observation is in line with recent claims that the functions of the SC reach far beyond vision, attention, and oculomotor control. The wide range of areas

contributing to the SC FCN comprising inferior/middle frontal area, posterior superior temporal visual area, and neck and shoulder representations of the primary motor cortex is a sign of possible multiplicity of cortical networks and functions that the SC plays a role in e.g. responses to moving objects, target selection, and postural control. The results of the first phase provided no clear evidence of SC FCN laterality. We were also unable to detect any sign of systematic depth-dependent alteration of the FCN. Even though we acquired solid evidence of the involvement of SC in a diversity of functional networks in our initial analyses, detection of the depth-dependent networks was not possible except with the help of higher quality data.

Based on the results of phase I, we used the HCP 7T fMRI dataset of 170 human subjects. This new dataset included the former subjects from phase I plus 26 more subjects. Our analysis showed that not only the early results from the first phase were replicable, but that also in-detail depth-dependent functional connectivity analysis of the SC was feasible. Information within the latter dataset of 7T fMRI proved to be adequate to separately recognize the functional networks that the human SC is part of. The Extrapolation of a higher resolution of the SC mask empowered the employed clustering algorithm for a fairly stable assignment of the global brain voxels to the clusters. This assignment was based on the voxel behavior pertinent to the plot of its signal correlation with the average signals from different layers of the SC. By employing this idea, we segmented the brain into 6 functional networks based on their correlation profiles with different SC layers. Except for one, all the estimated clusters could be related to the existing knowledge or predictions about the human SC function, e.g. our method identified the SC visual network as a unique cluster. Besides, it detected the oculomotor system as a separate cluster including areas that are typically involved in peripheral vision and attention. The clustering algorithm also suggested a wide combination of areas as a single cluster which plays a role in visual attention and planning goal-directed hand actions. It also provided a clear delineation of those brain areas which carry no significant functional connection to SC.

During the analyses of the first two phases of the project, one of the main concerns was our limited understanding of the SC anatomy from structural MR imaging. An accurate map of an ROI is essential for any functional connectivity analysis. Any excessive violation of the true ROI boundaries would result in inaccurate results and conclusions. To build the first in-vivo map of the human SC we piloted the 3rd phase of the project based on previously acquired and preprocessed UHF MRI quantitative maps by (Loureiro et al.,

2017). We used a 9.4T structural MRI dataset of 10 subjects with two modalities per subject for the automatic segmentation of the human SC. With 0.3mm isotropic voxels, we described the anatomy of the SC with 40 times more voxels compared to conventional structural images with 1mm isotropic voxels. The simultaneous use of QSM and R2* relaxometry maps resulted in a better-informed segmentation in comparison to the use of a single modality. By selecting the entire midbrain voxels as a seed, we utilized unsupervised deep learning methods for the automatic identification of prominent anatomical areas of the midbrain, including SC, based on their location and image-related characteristics which were hidden in the two quantitative maps. The use of 10 subjects, previously co-registered with an MNI brain template, also helped to generalize the outcome of the clustering to a supposed average human brain anatomy. Deep learning was the key tool to handle clustering over 400,000 voxels with 160 features for each voxel, which is impossible to perform manually or with conventional learning algorithms. Within the chosen anatomical frame, our method successfully delineated the boundaries of human SC. Besides, it estimated the extent of the boundaries for other know nuclei within the brainstem with unparalleled details, e.g. parvocellular and magnocellular areas of the red nuclei, pars reticulata, pars compacta, and pars lateralis sections of the substantia nigra, the 3 major tract bundles of the crus cerebri, periaqueductal grey and the inferior colliculus. Our findings suggest that UHF MRI could be a major contributor to a better understanding of the human brain anatomy, specifically for the less explored regions of the brainstem which is home to many significant nuclei and tracts.

In conclusion, the advances in MRI technology and mathematical tools are creating significant opportunities to investigate previously unexplored regions of the brain. Our in-vivo study of the human SC function and anatomy is a showcase for such possibilities, which in turn introduces many benefits in the field of healthcare with clinical applications based on a better understanding of neural disorders and personalized treatments.

REFERENCES

Acuña, C., Gonzalez, F., & Dominguez, R. (1983). Sensorimotor unit activity related to intention in the pulvinar of behaving Cebus apella monkeys. *Experimental brain research, 52*(3), 411-422.

Ajina, S., Kennard, C., Rees, G., & Bridge, H. (2014). Motion area V5/MT+ response to global motion in the absence of V1 resembles early visual cortex. *Brain, 138*(1), 164-178.

Akert, K., & Hartmann-von, K. M. (1980). Relationships of precentral premotor and prefrontal cortex to the mediodorsal and intralaminar nuclei of the monkey thalamus. *Acta neurobiologiae experimentalis, 40*(1), 7-25.

Asplund, C. L., Todd, J. J., Snyder, A. P., & Marois, R. (2010). A central role for the lateral prefrontal cortex in goal-directed and stimulus-driven attention. *Nature neuroscience, 13*(4), 507.

Baker, C. M., Burks, J. D., Briggs, R. G., Conner, A. K., Glenn, C. A., Sali, G., . . . Sughrue, M. E. (2018). A Connectomic Atlas of the Human Cerebrum—Chapter 1: Introduction, Methods, and Significance. *Operative Neurosurgery, 15*(suppl_1), S1-S9.

Baker, C. M., Burks, J. D., Briggs, R. G., Conner, A. K., Glenn, C. A., Taylor, K. N., . . . O'Donoghue, D. L. (2018). A Connectomic Atlas of the Human Cerebrum—Chapter 7: The Lateral Parietal Lobe. *Operative Neurosurgery, 15*(suppl_1), S295-S349.

Beckstead, R. M. (1979). An autoradiographic examination of corticocortical and subcortical projections of the mediodorsal-projection (prefrontal) cortex in the rat. *Journal of Comparative Neurology, 184*(1), 43-62.

Beckstead, R. M., & Frankfurter, A. (1982). The distribution and some morphological features of substantia nigra neurons that project to the thalamus, superior colliculus and pedunculopontine nucleus in the monkey. *Neuroscience, 7*(10), 2377-2388.

Beissner, F., & Baudrexel, S. (2014). Investigating the human brainstem with structural and functional MRI. *Frontiers in human neuroscience, 8*, 116.

Bell, A. H., Fecteau, J. H., & Munoz, D. P. (2004). Using auditory and visual stimuli to investigate the behavioral and neuronal consequences of reflexive covert orienting. *Journal of Neurophysiology, 91*(5), 2172-2184.

Benevento, L. A., & Standage, G. P. (1983). The organization of projections of the retinorecipient and nonretinorecipient nuclei of the pretectal complex and layers of the superior colliculus to the lateral pulvinar and medial pulvinar in the macaque monkey. *Journal of Comparative Neurology, 217*(3), 307-336.

Blair, R. C., & Karniski, W. (1993). An alternative method for significance testing of waveform difference potentials. *Psychophysiology, 30*(5), 518-524.

Boehnke, S. E., & Munoz, D. P. (2008). On the importance of the transient visual response in the superior colliculus. *Current opinion in neurobiology, 18*(6), 544-551.

Borra, E., Gerbella, M., Rozzi, S., & Luppino, G. (2017). The macaque lateral grasping network: a neural substrate for generating purposeful hand actions. *Neuroscience & Biobehavioral Reviews, 75*, 65-90.

Borra, E., Gerbella, M., Rozzi, S., Tonelli, S., & Luppino, G. (2012a). Projections to the Superior Colliculus From Inferior Parietal , Ventral Premotor , and Ventrolateral Prefrontal Areas Involved in Controlling Goal-Directed Hand Actions in the Macaque. doi:10.1093/cercor/bhs392

Borra, E., Gerbella, M., Rozzi, S., Tonelli, S., & Luppino, G. (2012b). Projections to the superior colliculus from inferior parietal, ventral premotor, and ventrolateral prefrontal areas involved in controlling goal-directed hand actions in the macaque. *Cerebral cortex, 24*(4), 1054-1065.

Brass, M., Derrfuss, J., Forstmann, B., & von Cramon, D. Y. (2005). The role of the inferior frontal junction area in cognitive control. *Trends in cognitive sciences, 9*(7), 314-316.

Buckner, R. L., Krienen, F. M., Castellanos, A., Diaz, J. C., & Yeo, B. T. (2011). The organization of the human cerebellum estimated by intrinsic functional connectivity. *American Journal of Physiology-Heart and Circulatory Physiology*.

Büttner, U., & Büttner-Ennever, J. (1988). Present concepts of oculomotor organization. *Reviews of oculomotor research, 2*, 3-32.

Caminiti, R., Genovesio, A., Marconi, B., Mayer, A. B., Onorati, P., Ferraina, S., . . . Maioli, M. G. (1999). Early coding of reaching: frontal and parietal association connections of parieto-occipital cortex. *European Journal of Neuroscience, 11*(9), 3339-3345.

Casagrande, V., Harting, J. K., Hall, W., Diamond, I., & Martin, G. (1972). Superior colliculus of the tree shrew: a structural and functional subdivision into superficial and deep layers. *Science, 177*(4047), 444-447.

Castiello, U., & Begliomini, C. (2008). The cortical control of visually guided grasping. *The Neuroscientist, 14*(2), 157-170.

Cechetto, D. F., & Shoemaker, J. K. (2009). Functional neuroanatomy of autonomic regulation. *Neuroimage, 47*(3), 795-803.

Chen, X., Duan, M., He, H., Yang, M., Klugah–Brown, B., Xu, H., . . . Yao, D. (2016). Functional abnormalities of the right posterior insula are related to the altered self-experience in schizophrenia. *Psychiatry Research: Neuroimaging, 256*, 26-32.

Cheng, A., Eysel, U. T., & Vidyasagar, T. R. (2004). The role of the magnocellular pathway in serial deployment of visual attention. *European Journal of Neuroscience, 20*(8), 2188-2192.

Chiba, T., Kayahara, T., & Nakano, K. (2001). Efferent projections of infralimbic and prelimbic areas of the medial prefrontal cortex in the Japanese monkey, Macaca fuscata. *Brain research, 888*(1), 83-101.

Chouinard, P. A., & Paus, T. (2006). The primary motor and premotor areas of the human cerebral cortex. *The Neuroscientist, 12*(2), 143-152.

Clower, D. M., West, R. A., Lynch, J. C., & Strick, P. L. (2001). The inferior parietal lobule is the target of output from the superior colliculus, hippocampus, and cerebellum. *Journal of Neuroscience, 21*(16), 6283-6291.

Collins, C. E., Lyon, D. C., & Kaas, J. H. (2005). Distribution across cortical areas of neurons projecting to the superior colliculus in new world monkeys. *The Anatomical Record Part A: Discoveries in Molecular, Cellular, and Evolutionary Biology: An Official Publication of the American Association of Anatomists, 285*(1), 619-627.

Corbetta, M., Patel, G., & Shulman, G. L. (2008). The reorienting system of the human brain: from environment to theory of mind. *Neuron, 58*(3), 306-324.

Courjon, J. H., Olivier, E., & Pélisson, D. (2004). Direct evidence for the contribution of the superior colliculus in the control of visually guided reaching movements in the cat. *The Journal of physiology, 556*(3), 675-681.

De Benedictis, A., Duffau, H., Paradiso, B., Grandi, E., Balbi, S., Granieri, E., . . . Sarubbo, S. (2014). Anatomo-functional study of the temporo-parieto-occipital region: dissection, tractographic and brain mapping evidence from a neurosurgical perspective. *Journal of anatomy, 225*(2), 132-151.

Dean, P., Redgrave, P., & Westby, G. (1989). Event or emergency? Two response systems in the mammalian superior colliculus. *Trends in neurosciences, 12*(4), 137-147.

Dermon, C., & Barbas, H. (1994). Contralateral thalamic projections predominantly reach transitional cortices in the rhesus monkey. *Journal of Comparative Neurology, 344*(4), 508-531.

Devinsky, O., Morrell, M. J., & Vogt, B. A. (1995). Contributions of anterior cingulate cortex to behaviour. *Brain, 118*(1), 279-306.

Fan, J., Han, F., & Liu, H. (2014). Challenges of big data analysis. *National science review, 1*(2), 293-314.

Faull, O. K., Jenkinson, M., Clare, S., & Pattinson, K. T. (2015). Functional subdivision of the human periaqueductal grey in respiratory control using 7 tesla fMRI. *Neuroimage, 113*, 356-364.

Fecteau, J. H., Bell, A. H., & Munoz, D. P. (2004). Neural correlates of the automatic and goal-driven biases in orienting spatial attention. *Journal of Neurophysiology, 92*(3), 1728-1737.

Ferraina, S., Johnson, P., Garasto, M., Battaglia-Mayer, A., Ercolani, L., Bianchi, L., . . . Caminiti, R. (1997). Combination of hand and gaze signals during reaching: activity in parietal area 7m of the monkey. *Journal of Neurophysiology, 77*(2), 1034-1038.

Fischl, B., Salat, D. H., Busa, E., Albert, M., Dieterich, M., Haselgrove, C., . . . Klaveness, S. (2002). Whole brain segmentation: automated labeling of neuroanatomical structures in the human brain. *Neuron, 33*(3), 341-355.

Fischl, B., Sereno, M. I., Tootell, R. B., & Dale, A. M. (1999). High-resolution intersubject averaging and a coordinate system for the cortical surface. *Human brain mapping, 8*(4), 272-284.

Fitzgibbons, M., & Salamon, N. (2016). Primer of Brainstem Anatomy: A Detailed Examination of Anatomy and Pathology Through MRI and DTI. *Neurographics, 6*(2), 76-87.

Fogassi, L., Gallese, V., Buccino, G., Craighero, L., Fadiga, L., & Rizzolatti, G. (2001). Cortical mechanism for the visual guidance of hand grasping movements in the monkey: A reversible inactivation study. *Brain, 124*(3), 571-586.

Fries, W. (1984a). Cortical Projections to the Superior Colliculus in the Macaque Monkey - a Retrograde Study Using Horseradish-Peroxidase. *Journal of Comparative Neurology, 230*(1), 55-76. doi:DOI 10.1002/cne.902300106

Fries, W. (1984b). Cortical projections to the superior colliculus in the macaque monkey: a retrograde study using horseradish peroxidase. *Journal of Comparative Neurology, 230*(1), 55-76.

Fries, W., & Distel, H. (1983). Large Layer Vi Neurons of Monkey Striate Cortex (Meynert Cells) Project to the Superior Colliculus. *Proceedings of the Royal Society Series B-Biological Sciences, 219*(1214), 53-+. doi:DOI 10.1098/rspb.1983.0058

Gaese, B., & Johnen, A. (2000). Coding for auditory space in the superior colliculus of the rat. *European Journal of Neuroscience, 12*(5), 1739-1752.

Galletti, C., & Fattori, P. (2018). The dorsal visual stream revisited: Stable circuits or dynamic pathways? *Cortex, 98*, 203-217.

Gitelman, D. R., Parrish, T. B., Friston, K. J., & Mesulam, M. M. (2002). Functional anatomy of visual search: regional segregations within the frontal eye fields and effective connectivity of the superior colliculus. *Neuroimage, 15*(4), 970-982. doi:10.1006/nimg.2001.1006

Glasser, M. F., Coalson, T. S., Robinson, E. C., Hacker, C. D., Harwell, J., Yacoub, E., . . . Van Essen, D. C. (2016). A multi-modal parcellation of human cerebral cortex. *Nature, 536*(7615), 171-178. doi:10.1038/nature18933

Glasser, M. F., Sotiropoulos, S. N., Wilson, J. A., Coalson, T. S., Fischl, B., Andersson, J. L., . . . Consortium, W. U.-M. H. (2013). The minimal preprocessing pipelines for the Human Connectome Project. *Neuroimage, 80*, 105-124. doi:10.1016/j.neuroimage.2013.04.127

Gnadt, J. W., & Beyer, J. (1998). Eye movements in depth: What does the monkey's parietal cortex tell the superior colliculus? *Neuroreport, 9*(2), 233-237.

Goldman, P. S., & Nauta, W. J. (1976). Autoradiographic demonstration of a projection from prefrontal association cortex to the superior colliculus in the rhesus monkey. *Brain research.*

Goossens, L., Schruers, K., Peeters, R., Griez, E., & Sunaert, S. (2007). Visual presentation of phobic stimuli: amygdala activation via an extrageniculostriate pathway? *Psychiatry Research: Neuroimaging, 155*(2), 113-120.

Grefkes, C., & Fink, G. R. (2005). The functional organization of the intraparietal sulcus in humans and monkeys. *Journal of anatomy, 207*(1), 3-17.

Grieve, K. L., Acuña, C., & Cudeiro, J. (2000). The primate pulvinar nuclei: vision and action. *Trends in neurosciences, 23*(1), 35-39.

Groh, J. M., & Sparks, D. L. (1996). Saccades to somatosensory targets. I. Behavioral characteristics. *Journal of Neurophysiology, 75*(1), 412-427.

Grossman, R. I., & Yousem, D. M. (1994). *Neuroradiology: the requisites*: Mosby.

Guo, T., Song, Y., Li, J., Fan, M., Yan, X., He, A., . . . Yang, G. (2018). Seed point discontinuity-based segmentation method for the substantia nigra and the red nucleus in quantitative susceptibility maps. *Journal of Magnetic Resonance Imaging, 48*(4), 1112-1119.

Haegelen, C., Coupé, P., Fonov, V., Guizard, N., Jannin, P., Morandi, X., & Collins, D. L. (2013). Automated segmentation of basal ganglia and deep brain structures in MRI of Parkinson's disease. *International journal of computer assisted radiology and surgery, 8*(1), 99-110.

Hardy, S. P., & Lynch, J. C. (1992). The spatial distribution of pulvinar neurons that project to two subregions of the inferior parietal lobule in the macaque. *Cerebral cortex, 2*(3), 217-230.

Hartigan, J. A., & Wong, M. A. (1979). Algorithm AS 136: A k-means clustering algorithm. *Journal of the royal statistical society. series c (applied statistics), 28*(1), 100-108.

Harting, J. K., Hall, W., Diamond, I., & Martin, G. (1973). Anterograde degeneration study of the superior colliculus in Tupaia glis: evidence for a subdivision between superficial and deep layers. *Journal of Comparative Neurology, 148*(3), 361-386.

Harting, J. K., Huerta, M. F., Frankfurter, A. J., Strominger, N. L., & Royce, G. J. (1980). Ascending pathways from the monkey superior colliculus: an autoradiographic analysis. *Journal of Comparative Neurology, 192*(4), 853-882.

Holmes, A. J., Hollinshead, M. O., O'Keefe, T. M., Petrov, V. I., Fariello, G. R., Wald, L. L., . . . Roffman, J. L. (2011). The organization of the human cerebral cortex estimated by intrinsic functional connectivity. *Scientific Data, Volume 2, Issue, pp. 150031 (2011). 2*, 150031.

Huerta, M. F. (1984). The mammalian superior colliculus: studies of its morphology and connections. *The comparative neurology of the optic tectum*, 687-772.

Huerta, M. F., & Harting, J. K. (1983). Sublamination within the superficial gray layer of the squirrel monkey: an analysis of the tectopulvinar projection using anterograde and retrograde transport methods. *Brain research, 261*(1), 119-126.

Huerta, M. F., & Kaas, J. H. (1990). Supplementary eye field as defined by intracortical microstimulation: connections in macaques. *Journal of Comparative Neurology, 293*(2), 299-330.

Huerta, M. F., Krubitzer, L. A., & Kaas, J. H. (1986). Frontal eye field as defined by intracortical microstimulation in squirrel monkeys, owl monkeys, and macaque monkeys: I. Subcortical connections. *Journal of Comparative Neurology, 253*(4), 415-439.

Huerta, M. F., Van Lieshout, D., & Harting, J. K. (1991). Nigrotectal projections in the primate Galago crassicaudatus. *Experimental brain research, 87*(2), 389-401.

Huk, A. C., Dougherty, R. F., & Heeger, D. J. (2002). Retinotopy and functional subdivision of human areas MT and MST. *Journal of Neuroscience, 22*(16), 7195-7205.

Iglesias, J. E., Van Leemput, K., Bhatt, P., Casillas, C., Dutt, S., Schuff, N., . . . Initiative, A. s. D. N. (2015). Bayesian segmentation of brainstem structures in MRI. *Neuroimage, 113*, 184-195.

Jay, M. F., & Sparks, D. L. (1987). Sensorimotor integration in the primate superior colliculus. II. Coordinates of auditory signals. *Journal of Neurophysiology, 57*(1), 35-55.

Jeffries, A. M., Killian, N. J., & Pezaris, J. S. (2014). Mapping the primate lateral geniculate nucleus: a review of experiments and methods. *Journal of Physiology-Paris, 108*(1), 3-10.

Kaas, J. H., & Lyon, D. C. (2007). Pulvinar contributions to the dorsal and ventral streams of visual processing in primates. *Brain research reviews, 55*(2), 285-296.

Katsuyama, N., Usui, N., & Taira, M. (2016). Activation of the Human MT Complex by Motion in Depth Induced by a Moving Cast Shadow. *PLoS One, 11*(9), e0162555.

Kim, J., Lenglet, C., Duchin, Y., Sapiro, G., & Harel, N. (2013). Semiautomatic segmentation of brain subcortical structures from high-field MRI. *IEEE journal of biomedical and health informatics, 18*(5), 1678-1695.

Klein, J. C., Rushworth, M. F., Behrens, T. E., Mackay, C. E., de Crespigny, A. J., D'arceuil, H., & Johansen-Berg, H. (2010). Topography of connections between human prefrontal cortex and mediodorsal thalamus studied with diffusion tractography. *Neuroimage, 51*(2), 555-564.

Komatsu, H., & Suzuki, H. (1985). Projections from the functional subdivisions of the frontal eye field to the superior colliculus in the monkey. *Brain research, 327*(1-2), 324-327.

Krauth, A., Blanc, R., Poveda, A., Jeanmonod, D., Morel, A., & Szekely, G. (2010). A mean three-dimensional atlas of the human thalamus: generation from multiple histological data. *Neuroimage, 49*(3), 2053-2062. doi:10.1016/j.neuroimage.2009.10.042

Künzle, H., & Akert, K. (1977). Efferent connections of cortical, area 8 (frontal eye field) in Macaca fascicularis. A reinvestigation using the autoradiographic technique. *Journal of Comparative Neurology, 173*(1), 147-163.

Künzle, H., Akert, K., & Wurtz, R. H. (1976). Projection of area 8 (frontal eye field) to superior colliculus in the monkey. An autoradiographic study. *Brain Res, 117*(3), 487-492.

Langley, J., Huddleston, D. E., Chen, X., Sedlacik, J., Zachariah, N., & Hu, X. (2015). A multicontrast approach for comprehensive imaging of substantia nigra. *Neuroimage, 112*, 7-13.

Lappe, M., Bremmer, F., Pekel, M., Thiele, A., & Hoffmann, K.-P. (1996). Optic flow processing in monkey STS: a theoretical and experimental approach. *Journal of Neuroscience, 16*(19), 6265-6285.

Leichnetz, G. R. (2001). Connections of the medial posterior parietal cortex (area 7m) in the monkey. *The Anatomical Record: An Official Publication of the American Association of Anatomists, 263*(2), 215-236.

Leichnetz, G. R., Spencer, R., Hardy, S., & Astruc, J. (1981). The prefrontal corticotectal projection in the monkey; an anterograde and retrograde horseradish peroxidase study. *Neuroscience, 6*(6), 1023-1041.

Lin, M., Lucas Jr, H. C., & Shmueli, G. (2013). Research commentary—too big to fail: large samples and the p-value problem. *Information Systems Research, 24*(4), 906-917.

Litjens, G., Kooi, T., Bejnordi, B. E., Setio, A. A. A., Ciompi, F., Ghafoorian, M., . . . Sánchez, C. I. (2017). A survey on deep learning in medical image analysis. *Medical image analysis, 42*, 60-88.

Lomber, S. G., Payne, B. R., & Cornwell, P. (2001). Role of the superior colliculus in analyses of space: superficial and intermediate layer contributions to visual orienting, auditory orienting, and visuospatial discriminations during unilateral and bilateral deactivations. *Journal of Comparative Neurology, 441*(1), 44-57.

Long, X.-Y., Zuo, X.-N., Kiviniemi, V., Yang, Y., Zou, Q.-H., Zhu, C.-Z., . . . Wang, L. (2008). Default mode network as revealed with multiple methods for resting-state functional MRI analysis. *Journal of neuroscience methods, 171*(2), 349-355.

Loureiro, J. R., Hagberg, G. E., Ethofer, T., Erb, M., Bause, J., Ehses, P., . . . Himmelbach, M. (2017). Depth-dependence of visual signals in the human superior colliculus at 9.4 T. *Hum Brain Mapp, 38*(1), 574-587. doi:10.1002/hbm.23404

Loureiro, J. R., Himmelbach, M., Ethofer, T., Pohmann, R., Martin, P., Bause, J., . . . Hagberg, G. E. (2018). In-vivo quantitative structural imaging of the human midbrain and the superior colliculus at 9.4 T. *Neuroimage, 177*, 117-128.

Lui, F., Gregory, K. M., Blanks, R. H., & Giolli, R. A. (1995). Projections from visual areas of the cerebral cortex to pretectal nuclear complex, terminal accessory optic nuclei, and superior colliculus in macaque monkey. *Journal of Comparative Neurology, 363*(3), 439-460.

Lund, R. D. (1969). Synaptic patterns of the superficial layers of the superior colliculus of the rat. *Journal of Comparative Neurology, 135*(2), 179-207.

Lund, R. D. (1972a). Anatomic studies on the superior colliculus. *Investigative ophthalmology & visual science, 11*(6), 434-441.

Lund, R. D. (1972b). Synaptic patterns in the superficial layers of the superior colliculus of the monkey, Macaca mulatta. *Exp Brain Res, 15*(2), 194-211.

Lund, R. D., Land, P., & Boles, J. (1980). Normal and abnormal uncrossed retinotectal pathways in rats: an HRP study in adults. *Journal of Comparative Neurology, 189*(4), 711-720.

Lünenburger, L., Kleiser, R., Stuphorn, V., Miller, L. E., & Hoffmann, K.-P. (2001). A possible role of the superior colliculus in eye-hand coordination. *Vision: From neurons to cognition, 134*, 109.

Luppino, G., Rozzi, S., Calzavara, R., & Matelli, M. (2003). Prefrontal and agranular cingulate projections to the dorsal premotor areas F2 and F7 in the macaque monkey. *European Journal of Neuroscience, 17*(3), 559-578.

Lynch, J., Graybiel, A., & Lobeck, L. (1985). The differential projection of two cytoarchitectonic subregions of the inferior parietal lobule of macaque upon the deep layers of the superior colliculus. *Journal of Comparative Neurology, 235*(2), 241-254.

Lynch, J., & Tian, J.-R. (2006). Cortico-cortical networks and cortico-subcortical loops for the higher control of eye movements. *Progress in brain research, 151*, 461-501.

Lyon, D. C., Nassi, J. J., & Callaway, E. M. (2010a). A disynaptic relay from superior colliculus to dorsal stream visual cortex in macaque monkey. *Neuron, 65*(2), 270-279.

Lyon, D. C., Nassi, J. J., & Callaway, E. M. (2010b). A disynaptic relay from superior colliculus to dorsal stream visual cortex in macaque monkey. *Neuron, 65*(2), 270-279. doi:10.1016/j.neuron.2010.01.003

Marrocco, R. T. (1978). Conduction velocities of afferent input to superior colliculus in normal and decorticate monkeys. *Brain research, 140*(1), 155-158.

Mars, R. B., Jbabdi, S., Sallet, J., O'Reilly, J. X., Croxson, P. L., Olivier, E., . . . Baxter, M. G. (2011). Diffusion-weighted imaging tractography-based parcellation of the human parietal cortex and comparison with human and macaque resting-state functional connectivity. *Journal of Neuroscience, 31*(11), 4087-4100.

Martin, J. A., Karnath, H.-O., & Himmelbach, M. (2015). Revisiting the cortical system for peripheral reaching at the parieto-occipital junction. *Cortex, 64*, 363-379.

May, P. J. (2006). The mammalian superior colliculus: laminar structure and connections. *Progress in brain research, 151*, 321-378.

Mikellidou, K., Kurzawski, J. W., Frijia, F., Montanaro, D., Greco, V., Burr, D. C., & Morrone, M. C. (2017). Area prostriata in the human brain. *Current Biology, 27*(19), 3056-3060. e3053.

Mikulić, A. (2010). *Primate superior colliculus neurons active in a goal-directed arm movement task involving hand-target contact and external task perturbation.* Ruhr University Bochum.

Min, E., Guo, X., Liu, Q., Zhang, G., Cui, J., & Long, J. (2018). A survey of clustering with deep learning: From the perspective of network architecture. *IEEE Access, 6*, 39501-39514.

Mohler, C. W., & Wurtz, R. H. (1976). Organization of monkey superior colliculus: intermediate layer cells discharging before eye movements. *Journal of Neurophysiology, 39*(4), 722-744.

Morris, J. S., Öhman, A., & Dolan, R. J. (1999). A subcortical pathway to the right amygdala mediating "unseen" fear. *Proceedings of the National Academy of Sciences, 96*(4), 1680-1685.

Moschovakis, A., Karabelas, A., & Highstein, S. (1988). Structure-function relationships in the primate superior colliculus. I. Morphological classification of efferent neurons. *Journal of Neurophysiology, 60*(1), 232-262.

Mruczek, R. E., von Loga, I. S., & Kastner, S. (2013). The representation of tool and non-tool object information in the human intraparietal sulcus. *Journal of Neurophysiology, 109*(12), 2883-2896.

Müri, R. M. (2006). MRI and fMRI analysis of oculomotor function. *Progress in brain research, 151*, 503-526.

Müri, R. M., Iba-Zizen, M., Derosier, C., Cabanis, E., & Pierrot-Deseilligny, C. (1996). Location of the human posterior eye field with functional magnetic resonance imaging. *Journal of Neurology, Neurosurgery & Psychiatry, 60*(4), 445-448.

Naidich, T. P., Duvernoy, H. M., Delman, B. N., Sorensen, A. G., Kollias, S. S., & Haacke, E. M. (2009). *Duvernoy's atlas of the human brain stem and cerebellum: high-field MRI, surface anatomy, internal structure, vascularization and 3 D sectional anatomy*: Springer Science & Business Media.

Nassi, J. J., & Callaway, E. M. (2009). Parallel processing strategies of the primate visual system. *Nature reviews neuroscience, 10*(5), 360.

Nicholls, J. G., & Paton, J. F. (2009). Brainstem: neural networks vital for life: The Royal Society.

Nichols, T. E., & Holmes, A. P. (2002). Nonparametric permutation tests for functional neuroimaging: A primer with examples. *Human brain mapping, 15*, 1-25. doi:10.1002/hbm.1058

Nitschke, K., Köstering, L., Finkel, L., Weiller, C., & Kaller, C. P. (2017). A meta-analysis on the neural basis of planning: Activation likelihood estimation of functional brain imaging results in the tower of London task. *Human brain mapping, 38*(1), 396-413.

Olive, I., Tempelmann, C., Berthoz, A., & Heinze, H. J. (2015). Increased functional connectivity between superior colliculus and brain regions implicated in bodily self-consciousness during the rubber hand illusion. *Hum Brain Mapp, 36*(2), 717-730. doi:10.1002/hbm.22659

Ouhaz, Z., Fleming, H., & Mitchell, A. S. (2018). Cognitive functions and neurodevelopmental disorders involving the prefrontal cortex and mediodorsal thalamus. *Frontiers in Neuroscience, 12*, 33.

Parthasarathy, H., Schall, J., & Graybiel, A. (1992). Distributed but convergent ordering of corticostriatal projections: analysis of the frontal eye field and the supplementary eye field in the macaque monkey. *Journal of Neuroscience, 12*(11), 4468-4488.

Passingham, R., Chung, A., Goparaju, B., Cowey, A., & Vaina, L. (2014). Using action understanding to understand the left inferior parietal cortex in the human brain. *Brain research, 1582*, 64-76.

Pattinson, K. T., Mitsis, G. D., Harvey, A. K., Jbabdi, S., Dirckx, S., Mayhew, S. D., . . . Wise, R. G. (2009). Determination of the human brainstem respiratory control network and its cortical connections in vivo using functional and structural imaging. *Neuroimage, 44*(2), 295-305.

Pergola, G., Danet, L., Pitel, A.-L., Carlesimo, G. A., Segobin, S., Pariente, J., . . . Barbeau, E. J. (2018). The Regulatory Role of the Human Mediodorsal Thalamus. *Trends in cognitive sciences*.

Perry, V. H., & Cowey, A. (1984). Retinal Ganglion-Cells That Project to the Superior Colliculus and Pretectum in the Macaque Monkey. *Neuroscience, 12*(4), 1125-1137. doi:Doi 10.1016/0306-4522(84)90007-1

Petrides, M. (2005). Lateral prefrontal cortex: architectonic and functional organization. *Philosophical Transactions of the Royal Society B: Biological Sciences, 360*(1456), 781-795.

Pierrot-Deseilligny, C., Milea, D., & Müri, R. M. (2004). Eye movement control by the cerebral cortex. *Current opinion in neurology, 17*(1), 17-25.

Pollack, J. G., & Hickey, T. L. (1979). The distribution of retino-collicular axon terminals in rhesus monkey. *Journal of Comparative Neurology, 185*(4), 587-602.

Prado, J., Clavagnier, S., Otzenberger, H., Scheiber, C., Kennedy, H., & Perenin, M.-T. (2005). Two cortical systems for reaching in central and peripheral vision. *Neuron, 48*(5), 849-858.

Prechelt, L. (1998). Automatic early stopping using cross validation: quantifying the criteria. *Neural Networks, 11*(4), 761-767.

Prevosto, V., Graf, W., & Ugolini, G. (2009). Posterior parietal cortex areas MIP and LIPv receive eye position and velocity inputs via ascending preposito-thalamo-cortical pathways. *European Journal of Neuroscience, 30*(6), 1151-1161.

Purpura, K. P., & Schiff, N. D. (1997). The thalamic intralaminar nuclei: a role in visual awareness. *The Neuroscientist, 3*(1), 8-15.

Rafal, R. D., Koller, K., Bultitude, J. H., Mullins, P., Ward, R., Mitchell, A. S., & Bell, A. H. (2015). Connectivity between the superior colliculus and the amygdala in humans and macaque monkeys: virtual dissection with probabilistic DTI tractography. *Journal of Neurophysiology, 114*, 1947-1962. doi:10.1152/jn.01016.2014

Rafal, R. D., Posner, M. I., Friedman, J. H., Inhoff, A. W., & Bernstein, E. (1988). Orienting of visual attention in progressive supranuclear palsy. *Brain, 111 (Pt 2)*(2), 267-280. doi:10.1093/brain/111.2.267

Rajkowska, G., & Goldman-Rakic, P. S. (1995). Cytoarchitectonic definition of prefrontal areas in the normal human cortex: I. Remapping of areas 9 and 46 using quantitative criteria. *Cerebral cortex, 5*(4), 307-322.

Reser, D. H., Burman, K. J., Yu, H.-H., Chaplin, T. A., Richardson, K. E., Worthy, K. H., & Rosa, M. G. (2012). Contrasting patterns of cortical input to architectural subdivisions of the area 8 complex: a retrograde tracing study in marmoset monkeys. *Cerebral cortex, 23*(8), 1901-1922.

Rockland, K. S. (1998). Convergence and branching patterns of round, type 2 corticopulvinar axons. *Journal of Comparative Neurology, 390*(4), 515-536.

Rockland, K. S. (2012). Visual system: prostriata—a visual area off the beaten path. *Current Biology, 22*(14), R571-R573.

Rodieck, R. W., & Watanabe, M. (1993). Survey of the Morphology of Macaque Retinal Ganglion-Cells That Project to the Pretectum, Superior Colliculus, and Parvicellular Laminae of the Lateral Geniculate-Nucleus. *Journal of Comparative Neurology, 338*(2), 289-303. doi:DOI 10.1002/cne.903380211

Rosano, C., Krisky, C. M., Welling, J. S., Eddy, W. F., Luna, B., Thulborn, K. R., & Sweeney, J. A. (2002). Pursuit and saccadic eye movement subregions in human frontal eye field: a high-resolution fMRI investigation. *Cerebral cortex, 12*(2), 107-115.

Rushworth, M. F., Behrens, T. E., & Johansen-Berg, H. (2006). Connection patterns distinguish 3 regions of human parietal cortex. *Cereb Cortex, 16*(10), 1418-1430. doi:10.1093/cercor/bhj079

Sadikot, A., Parent, A., & Francois, C. (1992). Efferent connections of the centromedian and parafascicular thalamic nuclei in the squirrel monkey: a PHA-L study of subcortical projections. *Journal of Comparative Neurology, 315*(2), 137-159.

Sapir, A., Soroker, N., Berger, A., & Henik, A. (1999). Inhibition of return in spatial attention: Direct evidence for collicular generation. *Nature neuroscience, 2*(12), 1053.

Scheperjans, F., Eickhoff, S. B., Hömke, L., Mohlberg, H., Hermann, K., Amunts, K., & Zilles, K. (2008). Probabilistic maps, morphometry, and variability of cytoarchitectonic areas in the human superior parietal cortex. *Cerebral cortex, 18*(9), 2141-2157.

Scheperjans, F., Palomero-Gallagher, N., Grefkes, C., Schleicher, A., & Zilles, K. (2005). Transmitter receptors reveal segregation of cortical areas in the human superior parietal cortex: relations to visual and somatosensory regions. *Neuroimage, 28*(2), 362-379.

Schneider, K. A., & Kastner, S. (2005). Visual responses of the human superior colliculus: a high-resolution functional magnetic resonance imaging study. *J Neurophysiol, 94*(4), 2491-2503. doi:10.1152/jn.00288.2005

Schuenke, M., Schulte, E., & Schumacher, U. (2010). *Head and neuroanatomy*: Thieme.

Sclocco, R., Beissner, F., Bianciardi, M., Polimeni, J. R., & Napadow, V. (2018). Challenges and opportunities for brainstem neuroimaging with ultrahigh field MRI. *Neuroimage, 168*, 412-426.

Segraves, M. A., & Goldberg, M. E. (1987). Functional properties of corticotectal neurons in the monkey's frontal eye field. *Journal of Neurophysiology, 58*(6), 1387-1419.

Shook, B., Schlag-Rey, M., & Schlag, J. (1990). Primate supplementary eye field: I. Comparative aspects of mesencephalic and pontine connections. *Journal of Comparative Neurology, 301*(4), 618-642.

Siegel, R. M., & Read, H. (1997). Analysis of optic flow in the monkey parietal area 7a. *Cerebral cortex (New York, NY: 1991), 7*(4), 327-346.

Small, D., Gitelman, D., Gregory, M., Nobre, A., Parrish, T., & Mesulam, M.-M. (2003). The posterior cingulate and medial prefrontal cortex mediate the anticipatory allocation of spatial attention. *Neuroimage, 18*(3), 633-641.

Sommer, M. A., & Wurtz, R. H. (2000). Composition and topographic organization of signals sent from the frontal eye field to the superior colliculus. *Journal of Neurophysiology, 83*(4), 1979-2001.

Song, J.-H., Rafal, R. D., & McPeek, R. M. (2011). Deficits in reach target selection during inactivation of the midbrain superior colliculus. *Proceedings of the National Academy of Sciences, 108*(51), E1433-E1440.

Soria, G., De Notaris, M., Tudela, R., Blasco, G., Puig, J., Planas, A. M., . . . Prats-Galino, A. (2011). Improved Assessment of Ex Vivo Brainstem Neuroanatomy With High-Resolution MRI and DTI at 7 Tesla. *The Anatomical Record: Advances in Integrative Anatomy and Evolutionary Biology, 294*(6), 1035-1044.

Sparks, D. L. (1981). The role of the monkey superior colliculus in the control of saccadic eye movements: a current perspective. *Developments in Neuroscience. Progress in oculomotor research*, 137-144.

Sparks, D. L. (1986). Translation of Sensory Signals into Commands for Control of Saccadic Eye-Movements - Role of Primate Superior Colliculus. *Physiological Reviews, 66*(1), 118-171.

Sprague, J. M. (1966). Interaction of cortex and superior colliculus in mediation of visually guided behavior in the cat. *Science, 153*(3743), 1544-1547.

Stanton, G., Goldberg, M., & Bruce, C. (1988). Frontal eye field efferents in the macaque monkey: II. Topography of terminal fields in midbrain and pons. *Journal of Comparative Neurology, 271*(4), 493-506.

Stepniewska, I., QI, H.-X., & Kaas, J. H. (2000). Projections of the superior colliculus to subdivisions of the inferior pulvinar in New World and Old World monkeys. *Visual neuroscience, 17*(4), 529-549.

Straub, S., Knowles, B. R., Flassbeck, S., Steiger, R., Ladd, M. E., & Gizewski, E. R. (2019). Mapping the human brainstem: Brain nuclei and fiber tracts at 3 T and 7 T. *NMR in Biomedicine, 32*(9), e4118.

Strong, S. L., Silson, E. H., Gouws, A. D., Morland, A. B., & McKeefry, D. J. (2016). A direct demonstration of functional differences between subdivisions of human V5/MT+. *Cerebral cortex, 27*(1), 1-10.

Sundermann, B., & Pfleiderer, B. (2012). Functional connectivity profile of the human inferior frontal junction: involvement in a cognitive control network. *BMC neuroscience, 13*(1), 119.

Tardif, E., Delacuisine, B., Probst, A., & Clarke, S. (2005). Intrinsic connectivity of human superior colliculus. *Exp Brain Res, 166*(3-4), 316-324. doi:10.1007/s00221-005-2373-z

Tigges, J., & Tigges, M. (1981). Distribution of retinofugal and corticofugal axon terminals in the superior colliculus of squirrel monkey. *Investigative ophthalmology & visual science, 20*(2), 149-158.

Topolovec, J. C., Gati, J. S., Menon, R. S., Shoemaker, J. K., & Cechetto, D. F. (2004). Human cardiovascular and gustatory brainstem sites observed by functional magnetic resonance imaging. *Journal of Comparative Neurology, 471*(4), 446-461.

Van Essen, D. C., Glasser, M. F., Dierker, D. L., Harwell, J., & Coalson, T. (2011). Parcellations and hemispheric asymmetries of human cerebral cortex analyzed on surface-based atlases. *Cerebral cortex, 22*(10), 2241-2262.

Van Essen, D. C., Lewis, J. W., Drury, H. A., Hadjikhani, N., Tootell, R. B., Bakircioglu, M., & Miller, M. I. (2001). Mapping visual cortex in monkeys and humans using surface-based atlases. *Vision research, 41*(10-11), 1359-1378.

Van Essen, D. C., Ugurbil, K., Auerbach, E., Barch, D., Behrens, T. E., Bucholz, R., . . . Consortium, W. U.-M. H. (2012). The Human Connectome Project: a data acquisition perspective. *Neuroimage, 62*(4), 2222-2231. doi:10.1016/j.neuroimage.2012.02.018

Visser, E., Keuken, M. C., Forstmann, B. U., & Jenkinson, M. (2016). Automated segmentation of the substantia nigra, subthalamic nucleus and red nucleus in 7 T data at young and old age. *Neuroimage, 139*, 324-336.

Vogt, B. A., & Vogt, L. (2003). Cytology of human dorsal midcingulate and supplementary motor cortices. *Journal of chemical neuroanatomy, 26*(4), 301-309.

Vogt, B. A., Vogt, L., & Laureys, S. (2006). Cytology and functionally correlated circuits of human posterior cingulate areas. *Neuroimage, 29*(2), 452-466.

Vu, A. T., Jamison, K., Glasser, M. F., Smith, S. M., Coalson, T., Moeller, S., . . . Yacoub, E. (2017). Tradeoffs in pushing the spatial resolution of fMRI for the 7T Human Connectome Project. *Neuroimage, 154*, 23-32.

Wang, J., Yang, Y., Fan, L., Xu, J., Li, C., Liu, Y., . . . Jiang, T. (2015). Convergent functional architecture of the superior parietal lobule unraveled with multimodal neuroimaging approaches. *Human brain mapping, 36*(1), 238-257.

Wang, Q., & Burkhalter, A. (2013). Stream-related preferences of inputs to the superior colliculus from areas of dorsal and ventral streams of mouse visual cortex. *Journal of Neuroscience, 33*(4), 1696-1705.

Wei, P., Liu, N., Zhang, Z., Liu, X., Tang, Y., He, X., . . . Li, J. (2015). Processing of visually evoked innate fear by a non-canonical thalamic pathway. *Nature communications, 6*, 6756.

Weiskopf, N., Mohammadi, S., Lutti, A., & Callaghan, M. F. (2015). Advances in MRI-based computational neuroanatomy: from morphometry to in-vivo histology. *Current opinion in neurology, 28*(4), 313-322.

Werner, W. (1993). Neurons in the primate superior colliculus are active before and during arm movements to visual targets. *European Journal of Neuroscience, 5*(4), 335-340.

Wilson, J. R., Hendrickson, A. E., Sherk, H., & Tigges, J. (1995). Sources of subcortical afferents to the macaque's dorsal lateral geniculate nucleus. *The Anatomical Record, 242*(4), 566-574.

Wilson, M. E., & Toyne, M. J. (1970). Retino-tectal and cortico-tectal projections inMacaca mulatta. *Brain research, 24*(3), 395-406.

Wurtz, R. H., & Albano, J. E. (1980). Visual-motor function of the primate superior colliculus. *Annual review of neuroscience, 3*(1), 189-226.

Wurtz, R. H., McAlonan, K., Cavanaugh, J., & Berman, R. A. (2011). Thalamic pathways for active vision. *Trends in cognitive sciences, 15*(4), 177-184.

Wurtz, R. H., & Mohler, C. W. (1976). Organization of monkey superior colliculus: enhanced visual response of superficial layer cells. *Journal of Neurophysiology, 39*(4), 745-765.

Wyder, M. T., Massoglia, D. P., & Stanford, T. R. (2003). Quantitative assessment of the timing and tuning of visual-related, saccade-related, and delay period activity in primate central thalamus. *Journal of Neurophysiology, 90*(3), 2029-2052.

Xiao, D., Zikopoulos, B., & Barbas, H. (2009). Laminar and modular organization of prefrontal projections to multiple thalamic nuclei. *Neuroscience, 161*(4), 1067-1081.

Xiao, Y., Bailey, L., Chakravarty, M. M., Beriault, S., Sadikot, A. F., Pike, G. B., & Collins, D. L. (2012). *Atlas-based segmentation of the subthalamic nucleus, red nucleus, and substantia nigra for deep brain stimulation by incorporating multiple MRI contrasts.* Paper presented at the International Conference on Information Processing in Computer-Assisted Interventions.

Xiao, Y., Jannin, P., d'Albis, T., Guizard, N., Haegelen, C., Lalys, F., . . . Collins, D. L. (2014). Investigation of morphometric variability of subthalamic nucleus, red nucleus, and substantia nigra in advanced Parkinson's disease patients using automatic segmentation and PCA-based analysis. *Human brain mapping, 35*(9), 4330-4344.

Xie, J., Girshick, R., & Farhadi, A. (2016). *Unsupervised deep embedding for clustering analysis.* Paper presented at the International conference on machine learning.

Yamasaki, D. S., Krauthamer, G. M., & Rhoades, R. W. (1986). Superior collicular projection to intralaminar thalamus in rat. *Brain research, 378*(2), 223-233.

Yeterian, E. H., & Pandya, D. N. (1993). Striatal connections of the parietal association cortices in rhesus monkeys. *Journal of Comparative Neurology, 332*(2), 175-197.

Yu, H.-H., Chaplin, T. A., Davies, A. J., Verma, R., & Rosa, M. G. (2012). A specialized area in limbic cortex for fast analysis of peripheral vision. *Current Biology, 22*(14), 1351-1357.

Zhang, X., Mlynaryk, N., Ahmed, S., Japee, S., & Ungerleider, L. G. (2018). The role of inferior frontal junction in controlling the spatially global effect of feature-based attention in human visual areas. *PLoS biology, 16*(6), e2005399.

STATEMENT OF CONTRIBUTIONS

CHAPTER 2 GLOBAL BRAIN FUNCTIONAL CONNECTIVITY OF THE HUMAN SC AT 3T

Chapter 2 largely follows the text of a manuscript to be submitted for publication. I contributed to the study design and conducted the data analysis together with Marc Himmelbach (MH). The text of chapter 2 was written by me with revisions from MH and Francesko Molla.

CHAPTER 3 DEPTH DEPENDENT FUNCTIONAL NETWORKS OF THE HUMAN SC

Chapter 3 largely follows the text of a manuscript to be submitted for publication. I designed the study and conducted the data analysis together with Marc Himmelbach (MH). The text of chapter 3 was written by me with revisions from MH and Francesko Molla.

CHAPTER 4 STRUCTURAL MAPPING OF THE HUMAN MIDBRAIN (SC)

Chapter 4 largely follows the text of a manuscript to be submitted for publication. . I designed the study and conducted the data analysis together with Marc Himmelbach (MH). The text of chapter 4 was written by me with revisions from MH. Gisela Hagberg (GH) and Joana Loureiro (JL) acquired the data used in chapter 4 and conducted the data preprocessing. GH and JL revised the text.

ACKNOWLEDGMENTS

First, I would like to thank my supervisor Dr. Marc Himmelbach for all the support, suggestions, presence, and guidance during the Ph.D. He has been an invaluable mentor, from who I learned not only about science and research but also made me improve on a personal level; always giving me priceless advice and cast light onto my professional career. He is with no doubt a huge source of inspiration and a role model to me.

I thank Prof. Dr. Markus Siegel for his thoughtful and accurate suggestions to improve the quality of the present work.

I thank Prof. Dr. Ludger Schoels for all the suggestions and insightful discussions during multiple stages of the project.

I thank Dr. Gisela Hagberg for her availability, openness, and generosity in helping out and sharing her resources.

I thank Dr. Joana Loureiro for sharing her thoughts and concerns and allowing me to build upon her valuable work.

I thank Bernd Kardatzki for the IT support and his patience and availability. Accomplishing such demanding projects would have been simply impossible without his remarkable selflessness.

I am deeply thankful to the Neuropsychology of Action group: Nikhil Prabhu, Eric McDermott, Francesko Molla, Sarah-Louisa Merkel, Nicole Knodel, and Dominik Wabersich for the great environment that was created daily and for not only being always ready to share critics, ideas, and suggestions at the work level but also to share tears, drinks laughs, insightful talks and lots of fun which helped me immensely the due course of the Ph.D. and motivated me to go through all the difficulties inherent to it.

I would like to sincerely express my gratitude to Prof. Dr. Dr. Hans-Otto Karnath and Ina Baumeister for their continuous support during my Ph.D.

This thesis would have never been possible without the love and encouragement of my family and friends. Their confidence and support made me go through all the difficulties

the entire time and kept me motivated to do always the best I could. I am especially grateful to my wife Shima for her love, support, and patience.